Extrasolar planet detection through spatially resolved observations

Meshkat, T.R.

Cover Page

Universiteit Leiden

Leiden University Repository

Author: Meshkat, Tiffany
Title: Extrasolar planet detection through spatially resolved observations
Issue Date: 2015-06-11

Extrasolar Planet Detection
Through Spatially Resolved Observations

Proefschrift

ter verkrijging van
de graad van Doctor aan de Universiteit Leiden,
op gezag van de Rector Magnificus Prof. mr. C. J. J. M. Stolker,
volgens besluit van het College voor Promoties
te verdedigen op donderdag 11 juni 2015
klokke 15:00 uur

door
Tiffany Meshkat
geboren te Mountain View, California, USA
in 1987

For my parents, whose unwavering support and sacrifices
have allowed me to follow my dream.

"If we long for our planet to be important, there is something we can do about it. We make our world significant by the courage of our questions and by the depth of our answers."
-Carl Sagan, *Cosmos*

TABLE OF CONTENTS

Chapter 1

INTRODUCTION

The interest in extrasolar planets (exoplanets) has been a feature of human inquiry for thousands of years, as evidenced by Epicurus' letter to Herodotus in the 4th century B.C. where he postulated that many other worlds – similar and different to our own – must exist. This curiosity is very relatable: we want to better understand ourselves, our planet, and our place in the universe. Until fairly recently, the only known planets were in our own solar system. Much of star and planet formation theories were derived from this limited knowledge. The existence of exoplanets was only confirmed when indirect planet detection techniques became suitably sensitive to find planets (Wolszczan & Frail 1992; Mayor & Queloz 1995).

The earliest exoplanet detection technique, radial velocity, takes advantage of the subtle Doppler shift in a star's spectrum due to a massive body orbiting nearby. This gravitational "wobble" technique revealed hundreds of close-in planets with systems very different to our own. The existence of "Hot Jupiters", planets as massive as Jupiter but within Mercury's orbit, led to a whole new field of planet migration studies. Later on, the transit technique led to the discovery of hundreds more planets which, by chance alignment with Earth, block out a small amount of the light from a star, causing a dip in its light curve over time. Since then, technological developments both from the ground and space, have resulted in the discovery of >1500 confirmed planets[1], in a diverse range of architectures and masses. The size and distribution of exoplanets around nearby stars in our galaxy provides insight into the different types of planet formation. This ultimately can help to reveal if our Solar System is typical or an exception.

---

[1]exoplanets.org
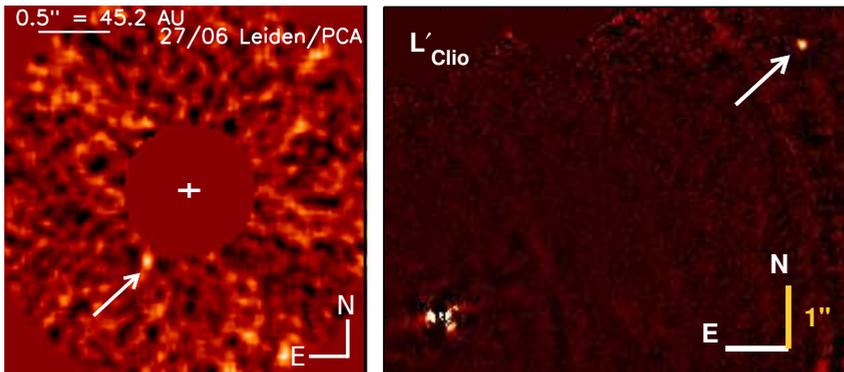
Figure 1.1 Left: Directly imaged 5 Jupiter mass planet HD 95086 b from Rameau et al. (2013c), indicated with a white arrow. Right: Planet HD 106906 b (white arrow) L'-band detection from Bailey et al. (2014).

1.1 Directly Imaging Exoplanets

Direct imaging is a recently successful technique to detect and characterize exoplanets. It involves directly detecting the photons from a planet itself. This techniques provides a unique opportunity to study young planets in the context of their formation and evolution. It examines the underlying semi-major axis exoplanet distribution (5 to 100 AU) and enables the characterization of the planet itself with spectroscopic examination of its emergent flux (Konopacky et al. 2013).

This method of planet detection is challenging for several reasons, some of which are readily apparent (planets are small, faint, and close to their host star) and others which are less clear from the outset (such as wavefront control, quasi-static speckles, etc. see Section 1.4). The limits of current technology only allow the direct detection of young, self-luminous planets. These young planets are still warm from their contraction, making them easier to directly detect in the infrared (Burrows et al. 2004) with typical planet-to-star contrasts of $10^{-5} - 10^{-6}$, compared to the values of $10^{-9} - 10^{-10}$ for more mature planets. Since these planets are young, they are ideal candidates to study the late stages of planet formation.

Despite the technical challenges associated with these detections, a handful of planetary-mass companions have been detected and confirmed (Figure 7.3): HR8799 bcde (Marois et al. 2008, 2010), Fomalhaut b (Kalas et al. 2008), β Pic b (Lagrange et al. 2009, 2010), 2MASS1207 b (Chauvin et al. 2004), 1RXS J1609–2105 b (Lafrenière et al. 2008), HD 95086 b (Rameau et al. 2013a), HD 106906 b (Bailey et al. 2014), GJ 504 b (Kuzuhara et al. 2013), and GU Psc b (Naud et al. 2014). A few of the detections may even be planets caught in formation (LkCa 15 b: (Kraus & Ireland 2012), HD 100546 b: (Quanz et al. 2013)). The detections of these young planets are beginning to bridge the gap between planets at large orbits (such as giant and icy giant planets in our Solar System) and their cooler and later stage cousins which are well mapped by the radial velocity and transit techniques.
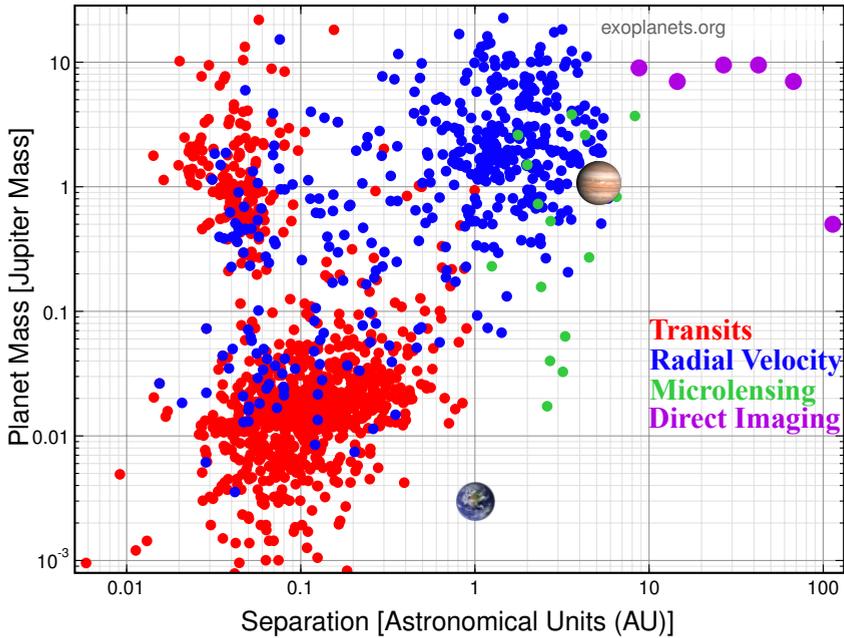
Figure 1.2 All detected and confirmed planets shown as a function of planet-star separation in AU and Jupiter masses (from exoplanets.org). The different colored points denote the method the planet was originally detected in. The vast majority of planets have been detected through the transit (red) and radial velocity (blue) method. Directly imaged planets (purple) are at a wider separation and higher mass than those detected through other techniques. Earth and Jupiter are also included as reference points.

Figure 1.2 shows the known and confirmed exoplanets, color coded based on the detection technique (from exoplanets.org). The planet-star separation in AU is plotted against the planet mass in Jupiter masses. Most of the planet detections have been made with the radial velocity (blue) and transit (red) method. Those two methods also overlap in planet-star separation and planet masses, allowing some targets to be observed via both methods. The direct imaging (purple) technique has only a handful of confirmed detections, at relatively high planet masses and large planet-star separations. Though there are fewer directly imaged planets, they occupy a previously unexplored region of this diagram. These planets are also very young, and thus probe earlier stages of planet formation, complementing the planets detected through other techniques. Advances in optics, wavefront control, and image processing techniques allow us to probe for lower mass, closer-in planets.

1.2 Planet Formation

Stars are formed from large cold clouds of molecular gas. Gravitational instability perturbs the cloud and starts its collapse. As a star forms out of a molecular cloud (Bergin & Tafalla 2007), conservation of angular momentum flattens its surrounding dust and gas into a circumstellar disk. It is in this early, gas rich stage that planets are thought to form. Eventually the gas is depleted, either blown out into the interstellar medium through stellar winds or through accretion onto the star or a planet (Alexander et al. 2014). The final stage in the disk life around a star is the debris disk phase, where planetesimals are collisionally ground up to form dust that is seen in reflected light (reviews by Wyatt 2008; Matthews et al. 2014). The planets in debris disks are thus recently formed, but the formation mechanism of giant planets is still a matter of contention. Even Jupiter's interior (and thus formation mechanism) is not well understood (Guillot 2005; Fortney & Nettelmann 2010). Two of the most popular giant planet formation mechanisms are core accretion (Safronov & Zvjagina 1969; Hayashi 1981; Pollack et al. 1996) and gravitational instability (Boss 1998; Mayer et al. 2002).

Core accretion begins with small micron and centimeter sized particles in a disk colliding and sticking together to form larger particles. These particles eventually coagulate to form planetesimals, which accrete to form a rocky planetary core ($\sim 5 - 10 M_\oplus$). As this planetary core orbits the star, its gravity accretes gas onto the surface of the core in a runaway process. This sweeping-up process also may explain how planets migrate through a disk. Planetary migration is a process which must have occurred given the observations of "Hot Jupiters" , which are too massive to have formed and swept-up enough gas at their current, small orbital separations (Lin et al. 1996; Rasio et al. 1996). However, this formation method is not without its challenges. Meter sized particles are expected to collide at velocities that are too high to result in sticking (Brauer et al. 2008). These bodies also decouple from the gas, causing them to drift rapidly into the star (Weidenschilling 1977). These two processes make it difficult for particles to grow larger than a meter in size. Icy dust grains have been proposed as a method to overcome this barrier, as ice grains collide and stick more easily (Okuzumi et al. 2012; Krijt et al. 2015). Also, accretion of gas onto the core must occur before the disk dissipates. Core accretion is thought to occur on a timescale of 0.5 to 10 Myr, while the observed disk lifetimes are 1 to 10 Myr.

Gravitational instability is a "top-down" method of giant planet formation. A higher mass planet is thought to form out of an instability in the gas and dust rich disk, which fragments into clumps and starts a gravitational collapse (Boss 1998; Mayer et al. 2002). In this scenario, the dust grains sink to form the core of the planet via self-gravity. Unlike core accretion, gravitational instability can form planets relatively quickly, with a timescale of a few disk orbits (100-1000 years at 10 to 100 AU). However, the cause of the fragmentation is uncertain. Fragmentation can only occur if the disk cools quickly enough, based on the Toomre instability parameter, or it can be caused by an external gravitational trigger, such as a binary star (Mayer et al. 2005).

Boley (2009) proposed that both planet formation mechanisms may create
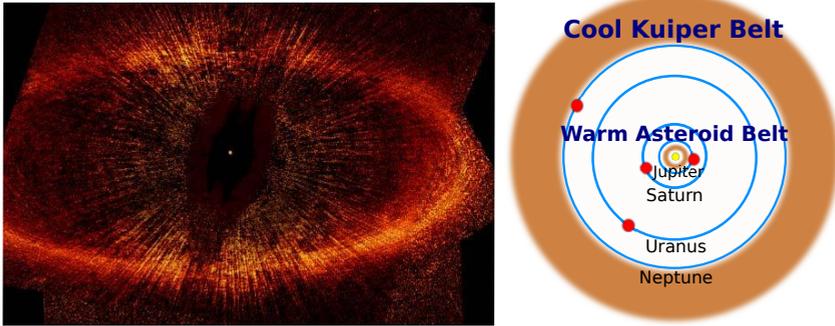
Figure 1.3 Left: The debris disk around the star Fomalhaut ([Kalas et al. 2005](#)), seen with the Hubble Space Telescope in scattered light. The debris has been sculpted into a ring, likely by an unseen planet. Right: Visualization of the two-belt dust debris structure in the Solar System.

planets in different parts of the disk: gravitational instability beyond a disk radii $r > 100$ AU and core accretion inside $r < 100$ AU. Transit studies with the Kepler space telescope have revealed that small planets ($\leq 2.5 R_\oplus$) are extremely common at small angular separations ([Batalha et al. 2013](#); [Fressin et al. 2013](#); [Lissauer et al. 2014](#)). Given their current separation and relatively low mass, most of these planets are thought to have formed via core accretion. Direct imaging surveys suggest that planets are very infrequent at large separations (see Section [1.5](#)). These large separation, high mass planets have been proposed to form by gravitational instability ([Marois et al. 2010](#)). However, recent studies cast doubt on the HR 8799 planets having formed via gravitational instability, as their masses and separations do not fulfill the model Toomre and cooling time criteria ([Rameau et al. 2013a](#)). Additionally, the lack of giant planets at large orbital radii suggests that giant planets formed via gravitational instability are uncommon ([Bowler et al. 2015](#)).

Theoretical planet cooling curves are employed to predict the temperature of giant planets over time. The "hot-start" models ([Burrows et al. 1997](#)) are most closely related to the gravitational instability planet formation mechanism: an object radiates its initial gravitational potential energy slowly. The "cold-start" and "warm-start" models ([Marley et al. 2007](#); [Spiegel & Burrows 2012](#)) involve the rapid loss of initial entropy caused by accretion, and thus is more related to core accretion. The masses of directly imaged planets are estimated from these evolutionary models.

1.3   Planet-Disk Interactions

In addition to detecting and characterizing planets, the results of direct imaging studies contribute to our understanding of debris disks. Nearly all of the directly imaged planets have been found around stars with debris disks; bright circumstellar dust clouds (see Figure [1.3](#), left). The dust is generated in collisional cascades of
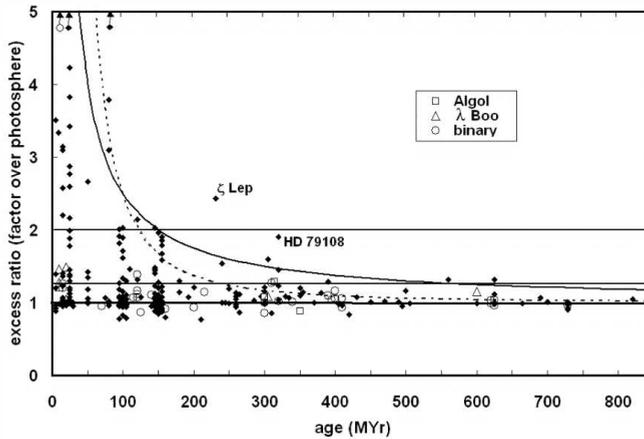
Figure 1.4 24 μm excess emission versus age for A-type stars, from (Rieke et al. 2005). The excess emission is the ratio of the flux density in the SED over the stellar photosphere alone. A ratio of 1 has no excess emission. Targets with an excess ratio >1.25 are considered the threshold for detection of an excess. An excess ratio >2 is considered a large excess. The decaying frequency of debris disks with age demonstrates the likelihood that an A-type star with a debris disk is young.

asteroids and comets, which can form grains down to a few microns (Acke et al. 2012). These small bodies are the remnants of planetesimals, which are thought to be the building blocks of planet cores. Thus, debris disks may be indicators of recent planet formation.

Debris disks can be directly detected (Figure 1.3, left) or inferred from excess infrared emission in a stellar energy distribution (SED). Resolved debris disks are extremely useful for direct imaging studies, as the inclination of the system can be assessed and, in some cases, substructure (such as gaps or holes) can be seen (Kalas et al. 2005). If a companion is detected in such systems, the inclination allows determination of the orbital separation from the star, rather than the projected separation. For unresolved debris disks, the approximate mass, temperature, inner and outer radii can be inferred by fitting the SED with an appropriate model. Figure 1.4 demonstrates that the frequency of debris disks decays over time (Rieke et al. 2005). These debris disks are inferred from excess 24 μm emission in their SEDs. Whether the disk is resolved or not, debris disks provide a wealth of information about the structure of the dust around a star and imply youth for the system.

A subset of debris disks show the signature of two temperature components in the SED: a warm inner belt and a cool outer belt. The relatively dust-free gap between these belts may be caused by one or more planets accreting the debris material as they form (Chiang et al. 2009). Our own Solar System has a two-component structure, with a warm inner asteroid belt, cool outer Kuiper belt, and
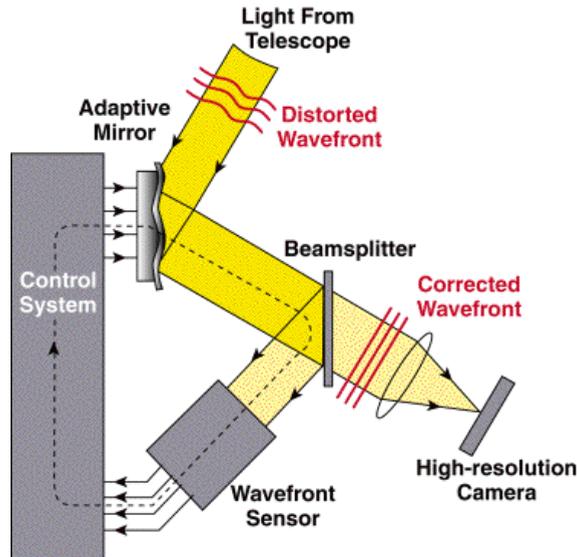
Figure 1.5 Demonstration of how an AO system corrects an incoming wavefront using a wavefront sensor which then adjusts the deformable mirror in real-time to produce a final corrected image (lyot.org).

four planets present across the gap (Figure 1.3, right). In the case of Fomalhaut, the cool outer belt is resolved, while the warm inner belt is inferred from the SED.

1.4   Observing Strategies and Image Processing

1.4.1   Optical Aberrations

As the light from a point source passes through an optical system, the shape of the image is called the point spread function (PSF). In the case of a circular aperture in a telescope, the PSF shape is described as an Airy disk. The central core of the PSF contains most of the stellar flux, with several, successively fainter Airy rings around the star. The theoretical, diffraction-limited resolution of a telescope is defined on this basis:

$$\theta \approx 1.22\lambda/D \qquad (1.1)$$

where λ is the wavelength and D is the diameter of the telescope. This also defines the minimum angular separation at which two objects of equal brightness can be resolved. Reaching this limit at a telescope, the so-called "Diffraction limit", is the goal if one wants to detect objects very near each other (i.e. planets). In order to reach a smaller diffraction limit, one must either observe in a shorter wavelength or with a larger telescope.

Achieving the diffraction limit of a telescope, however, is a challenging task. Instrumental aberrations are present in nearly every optical system. Even the Hubble Space Telescope has spherical aberrations in the primary mirror. In addition to static instrumental aberrations, ground-based telescopes have the challenge of observing through the turbulent, refractive atmosphere of the Earth.

1.4.2   Adaptive optics

The Earth's atmosphere introduces temporal and spatial variations in the light path from a point source, causing an image to appear smeared out. Adaptive Optics (AO) was invented in order to counter this blurring. An AO system measures the deviations in the incoming stellar wavefront using a wavefront sensor. The wavefront sensor determines the correction necessary to create a flat wavefront, and sends the correction information to a deformable mirror (DM). Ideally the DM cancels the aberration in the wavefront by physically reshaping the mirror, using actuators, to be the inverse aberration shape with half the amplitude. In a theoretical system where the DM is able to correct the atmospheric aberrations in real-time, the resulting wavefront would be flat. In practice, there is a brief time delay between the wavefront sensor and the DM correction. This process is repeated hundreds of times a second in order to compensate for the varying turbulence, which produces a point source (see Figure 1.5).

In order for this process to measure the wavefront accurately, a bright light source is needed. If the target object is too faint to be a natural guide star, a laser guide star is used to generate a fake point source. For the purposes of directly imaging exoplanets, the target stars are most often bright enough to act as their own natural guide star. AO correction is necessary to directly image exoplanets, since we require the stellar flux to be centralized in a point source as much as possible, in order to detect faint point sources at very small angular separations.

1.4.3   Coronagraphs

Coronagraphs are optics inserted in the light path of a telescope which minimize the diffracted light from a source, to allow access to small angular separations around a star. One of the first coronagraphs, the classical Lyot (Lyot 1939), achieved this with two optical elements, visualized in the top light path diagram in Figure 1.6. The light from the star (blue line) is blocked by a mask in the focal plane of the telescope. Since the planet (red line) is physically separated from the star, the angle of its incoming light is not blocked by the mask. Then a Lyot stop is inserted in the pupil plane in order to block the outer edge of the telescope pupil in the pupil plane image. Finally the image is formed on the detector. This coronagraph design is extremely sensitive to the telescope alignment, as the star must be placed precisely behind the focal plane mask (called tip-tilt alignment) and is thus sensitive to telescope vibrations. This physical mask also has the potential to block a planet signal, which may be very close to its parent star. Developments in coronagraphs have led to significant improvements on the classical Lyot (4QPM; Rouan et al. 2000), however the tip-tilt alignment is still a limitation as most
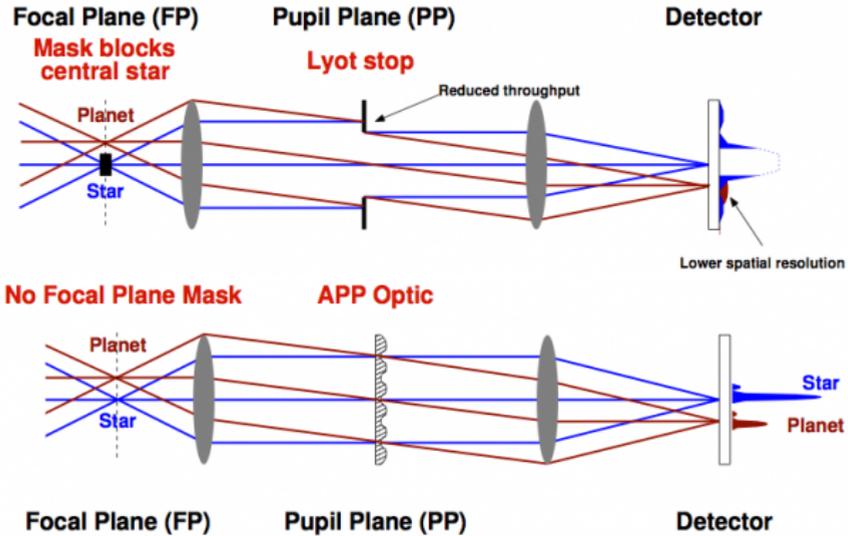
Figure 1.6 Light path diagrams demonstrating the Lyot coronagraph and the APP coronagraph designs, from Kenworthy et al. (2010). Both coronagraphs aim to allow the detection of faint sources close to a bright star. The classical Lyot uses a focal plane mask and a Lyot stop in the pupil plane. The APP only has one optic, which is in the pupil plane. The resulting image on the detector is seen on the right.

designs require an optic in the focal plane.

The Apodizing Phase Plate (APP) coronagraph (Kenworthy et al. 2010) uses only a single optic, placed in the pupil plane of the telescope, seen in the bottom light path diagram in Figure 1.6. The APP optic uses the light diffracted from the Airy core of the star to cancel out the coherent light in the diffraction rings. In effect, this minimizes the diffraction pattern on one side of the star, while reinforcing it on the other side. The result is seen on the right of Figure 1.6, the central Airy core of the star still reaches the detector, but the adjusted diffraction ring pattern allows the planet signal to shine through. This figure also demonstrates that everything in the field of view will have the characteristic APP diffraction suppression structure, including planets. As the central Airy core flux itself is used to cancel out the diffraction pattern on one side of the star, there is a cost of 40% to throughput. The APP was designed to have a "dark hole" where the sky background limit can be reached in the final APP images from $0\farcs18$ to $0\farcs75$ in which to search for faint companions. The most significant difference with previous coronagraph design is the lack of a focal plane mask. Thus, the APP is insensitive to tip-tilt errors and can even be used to observe binary star systems. Figure 1.7 shows the increased sensitivity at small angular separations with the APP (solid line), compared with direct imaging (dashed line). This figure was generated using real archival data of the same target obtained in L'-band with the
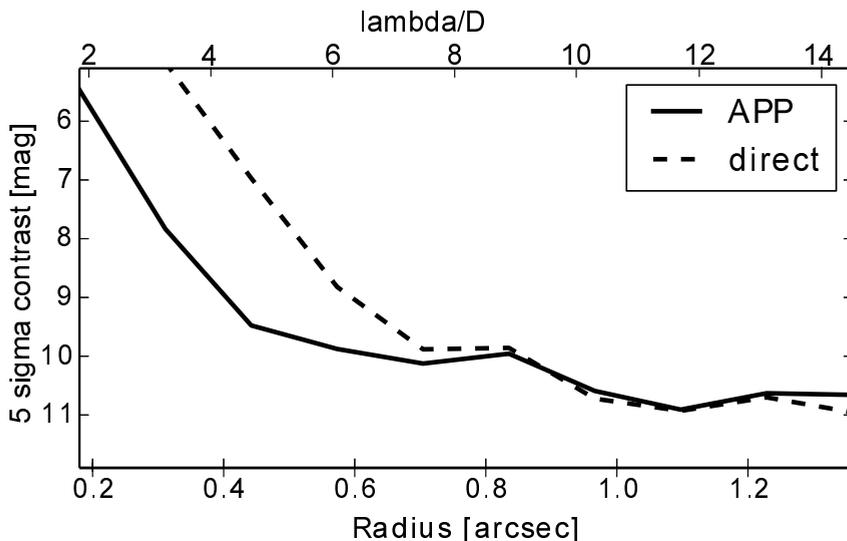
Figure 1.7 Comparison of sensitivity achieved with the APP coronagraph versus direct imaging for the same target observed with the NACO instrument on the VLT (from Meshkat et al. *submitted*).

NACO instrument on the VLT and processed with these same pipeline.

1.4.4 Angular Differential imaging

Sophisticated image processing algorithms are necessary to remove the "quasi-static super speckles" in our data, in order to let the light from a planet shine through. Though direct imaging data are obtained with AO correction, speckles remain in the images. These speckles, caused by instrumental features and residual atmospheric turbulence, can appear brighter than a planetary-mass companion (Hinkley et al. 2009). Several image processing algorithms have been developed to model and subtract these aberrations. One such algorithm is Angular Differential Imaging (ADI: Marois et al. 2006). In ADI mode, the sky de-rotator on an ALT-AZ mounted telescope is turned off, allowing the sky to rotate around a star. A planet will appear to orbit over time, while the aberrations stay relatively fixed. Assuming the planet is not in the same position in any consecutive images, a median over all images in time will capture the static speckle aberrations, but not the planet. While this median image succeeds in modelling the general stellar PSF structure, the speckles vary in brightness on time scales of the observing sequence.

1.4.5 SDI

Based on evolutionary cooling tracks (Baraffe et al. 2003), planets were predicted to have a strong methane signal, similar to field brown dwarfs. Simultaneous

Differential Imaging (SDI) is a method which takes advantage of this prediction, by simultaneously imaging in and out of the methane absorption feature at 1.62 μm. By subtracting the different narrow-band images, the stellar flux and speckles will be subtracted and the light from planet with methane absorption will be preserved (Biller et al. 2007). However, many recent studies do not find strong methane absorption from the known directly imaged planets (e.g. HR 8799 bcd and 2M1207 b; Skemer et al. 2014), suggesting that planets are not the same as field brown dwarfs of equivalent effective temperatures.

1.4.6   Locally optimized combination of images

Locally Optimized Combination of Images (LOCI) (Lafrenière et al. 2007) is a planet detection algorithm which models the stellar PSF in a subregion of the images to remove speckles. Data are obtained in ADI mode, to allow any companion source (and the sky) to rotate between successive images in time. For the ADI algorithm a simple median is taken over all the images in order to subtract the stellar PSF. This assumes that there is enough sky rotation such that a companion will never overlap with itself in successive images. In practice, a companion will always have some small amount of overlap between images. Thus, subtracting the median of the images will result in some self-subtraction of a companion. The LOCI algorithm mitigates this problem by introducing the parameter N_δ, which is the minimum amount of overlap allowed in units of the PSF full-width half maximum (FWHM). This determines how many images are rejected from the stellar PSF fit, in order to prevent self-subtraction. For example, an N_δ of 1 ensures there is no overlap of a companion, however it may result in the rejection of many frames depending on the sky rotation and angular separation of a companion. At smaller angular separations, the same amount of sky rotation results in a smaller actual movement:

$$\text{linear motion} = 2\pi r \frac{\theta}{360°} \qquad (1.2)$$

At very small angular separations (r), a companion may have very little linear motion, resulting in many rejected images. Lafrenière et al. (2007) consider a range of N_δ values from 0.25 (much self-subtraction allowed) up to 2.0 (none allowed). They find the value of N_δ=0.5 is optimal trade-off at including enough images to generate an accurate stellar PSF model while preventing too much self-subtraction.

The LOCI algorithm differs further from ADI by not taking a simple median over the images. The images are divided into annuli, which are subdivided into wedges. A linear least squares combination of images subtracts the speckles within one wedge region at a time. The size of each wedge is based on two parameters set by the user. This wedge is called the signal region S_T, where a potential planet signal is considered. As the sky rotation causes the planet to rotate around its parent star, it will pass in and out of the S_T region over the whole observing sequence. A larger optimization region wedge O_T, usually surrounding S_T, is used as a reference for speckles at that location. A least squares fit is performed on O_T at a fixed pixel location over the whole set of observed frames. Since the sky

is rotating around the parent star, a planet would only appear temporarily in the wedge in a few frames and therefore will not be a significant contribution to the least squares fit. To minimize the self subtraction of a potential planet, the frames nearest in time to a given single science frame are not included in the least squares fit. The fit of the O_T region is subtracted from the S_T region, and the process is repeated for all other wedges. Once all the wedges are processed, the frames are rotated by the parallactic angle so all the frames have the North axis up and East to the left. This least squares fitting algorithm is successful at minimizing speckles, however at small angular separations the self-subtraction is still an issue.

1.4.7   Principal Component Analysis

Principal Component Analysis (PCA) is another algorithm whose recent application to high contrast exoplanet imaging has been shown to be very effective (Amara & Quanz (2012), Soummer et al. (2012)). For exoplanet imaging, PCA involves converting a stack of science images into principal, orthogonal, linearly uncorrelated components. Some linear combination of these basis vectors, called principal components (PCs), can be used to represent every science image in the original stack.

PCA also takes advantage of data obtained in ADI mode, though sky rotation is not strictly necessary [2]. Unlike LOCI, the whole image is processed at once, rather than subdivided into wedges, making PCA less expensive. All the images in a stack are flattened into a single dimensional array. The mean of the stack of flattened images is subtracted from each flattened image. This step ensures the computed PC vectors always go through the origin. The flattened images are passed to a singular value decomposition (SVD) algorithm in order to determine the most dominate features in the images. SVD returns the following three matrices:

$$S = UWV^T \tag{1.3}$$

where S is the stack of one-dimensional images, U is a column-orthogonal matrix, W is a diagonal matrix with the positive, singular values corresponding to each PC, and V contains the PC singular vectors. The nth PC singular value is the variance of the image stack in the direction of the nth PC vector. The PCs are in order of decreasing contribution. The first PC has the highest singular value and defines the direction of the line through the origin that best fits the derived stack of images, in a least squares sense. A subset of these PCs are used in the linear least squares fit. The mean of the stack of flattened images, which was subtracted earlier, is appended to this subset of PCs. A linear least squares fit of this subset of PCs is performed on the first flattened image. The resulting coefficients are crossed with the PCs to construct the stellar PSF for the first image. The stellar PSF model is subtracted from the first image. This process is repeated for all subsequent images. The optimal number of PCs used in the linear fit is a trade-off between subtracting speckles and increasing the background noise.

---

[2]demonstrated with the equatorial mounted Palomar telescope, see (Fergus et al. 2014).

1.5   Overview of Direct Imaging Surveys

Many surveys have been performed, taking advantage of technological and image processing advantages (section 1.4), in order to directly image planets. There are several, large completed imaging surveys, each of which imaged ~40 to 250 stars: the Gemini Deep Planet Survey (GDPS, Lafrenière et al. 2007, the L' and M-band survey of sun-like stars (Heinze et al. 2010), the International Deep Planet Survey (IDPS, Vigan et al. 2012), the NICI instrument science campaign (Biller et al. 2013; Wahhaj et al. 2013; Nielsen et al. 2013), the NACO L'-band survey (Rameau et al. 2013a), the Strategic Exploration of Exoplanets and Disks with Subaru (SEEDS, Janson et al. 2013; Brandt et al. 2014), the NACO instrument large program (Desidera et al. 2015; Chauvin et al. 2015) the Planets around Low-mass Stars (PALMS) survey (Bowler et al. 2015). Despite the huge amount of stars surveyed, only three planetary systems were discovered through these surveys: HR 8799 bcde (Marois et al. 2008, 2010) from the GDPS survey, HD 95086 b (Rameau et al. 2013b) from the NACO L'-band survey, and GJ 504 b (Kuzuhara et al. 2013) from the SEEDS survey. Despite the few planet detections, many of these surveys have performed robust statistical analyses in order to place constraints on the planet occurrence rate as a function of stellar properties. The key findings and statistics from each survey are reported below.

GDPS was one of the first large direct imaging surveys searching for planets. 85 FGKM-type stars were observed at the Gemini North with the NIRI instrument in the narrowband filter CH4-short (1.54-1.65 μm) with ADI and AO (see Section 1.4). The data on average were sensitive to planets down to 2 M_{Jup} with a projected separation of 40 to 200 AU. Many companion candidates were detected in the initial analysis, but nearly all of the second-epoch observations confirmed that these were background sources (48 out of 54 targets). This high false-positive rate is a common occurrence for data in the 1.6 μm range, as stars are brighter in these shorter wavelengths. The remaining targets were discovered to be binary companions. The HR 8799 four planets were reported separately from the survey paper (Marois et al. 2008, 2010). They found the upper limit of the fraction of stars with at least one planetary mass object is 0.28 for 10-25 AU, 0.13 for 25-50 AU, and 0.093 for 50-250 AU.

The L'- and M-band survey obtained data no 54 nearby, sun-like stars with the Clio instrument on the MMT. The targets were preferentially selected based on proximitymed to be background stars. targets. Thirteen potential companions were detected, eleven of which were confirmed to be background stars. A low-mass star and brown dwarf companion were discovered, but no planetary mass objects were detected. They performed Monte Carlo simulations to test the planet distribution power law coefficients (Heinze et al. 2010a), assuming radial velocity statistics. They conclude that less than 8.1% of stars have three, wide orbit, massive planets, like the HR 8799 system. Thus, giant planets in large orbital separations are rare around sun-like stars.

The IDPS survey combined data from the VLT/NACO instrument and Gemini/NIRI instrument on 42 A-type stars with the CH4s and Ks-band (1.95-2.30μm) filters. A-stars are often the targets in direct imaging surveys, as radial velocity

searches for planets (Johnson et al. 2007) and planet formation theories (Alibert et al. 2011) suggest that more massive stars form massive planets more frequently. No planetary mass companions were detected in this survey. Their statistical analysis of the null result concludes that the fraction of A-stars with one massive planet (3-14 $M_{\rm Jup}$) is 5.9-18.8% from 5-320 AU at 68% confidence. They suggest that the peak of the massive planet population around A-stars may fall between the separations probed with radial velocity and direct imaging.

The NICI science campaign used the Gemini/NICI instrument in H-band to determine the frequency of giant planets around three surveys of stars: 57 debris disk stars, 80 young moving group stars, and 70 young B and A stars. Many companion candidates were detected in these surveys, but follow-up confirmed that all were either background sources, brown dwarfs or stellar mass companions. Bayesian analysis of the null result in the young moving group survey of 80 stars resulted in the strongest constraint on the planet fraction at that time: ≤6% of stars have 1-20 $M_{\rm Jup}$ planetary mass objects at semi-major axes of 10-150 AU at the 95% confidence level, using COND models (Baraffe et al. 2003). The debris disk survey concluded that the β Pic and HR 8799 planetary systems are rare. The B and A star survey agreed with this analysis: <10% of B and A stars have a planetary mass companion similar to the outer-most HR 8799 planet b (7 $M_{\rm Jup}$ at 68 AU) at 68% confidence.

The NACO L'-band survey (Rameau et al. 2013a) targeted 59 young, nearby stars with inferred debris disks with the VLT/NACO instrument in L'-band (3.8μm). The HD 95086 b planet was reported separately from the survey paper (Rameau et al. 2013b). Based on their survey results, their statistical analysis of the fraction of giant planets at large separations finds that 1-13 $M_{\rm Jup}$ planets have an occurrence of 10.8% to 24.8% from 1-1000 AU, at 68% confidence level.

The SEEDS survey is not yet complete. The results published thus far combine observations of ~250 stars with the Subaru/HiCIAO, Gemini/NIRI, and Gemini/NICI instruments. All data were obtained in H-band (1.65μm). The detection of the planet GJ 504 b was published separately (Kuzuhara et al. 2013). Through statistical analysis of their sample, they find that the commonly used radial velocity planet distribution function cannot extend beyond the (model-dependent) maximum semimajor axis of 30-100 AU.

The NACO large program observed 86 FGK-type stars with the VLT/NACO instrument in H-band, aiming to provide constraints on the frequency of planets and brown dwarfs in preparation for the new VLT/SPHERE instrument. No new planets were detected as part of this survey. They determine an upper limit on the occurrence of giant planets to be <15% for a >5 $M_{\rm Jup}$ planet between 100-500 AU, and <10% for a >10 $M_{\rm Jup}$ planet between 50-500 AU at 95% confidence.

The PALMS survey targeted 122 young M dwarf stars with H and K-band coronagraphic observations with the Keck/NIRC2 and Subaru/HiCIAO instruments. Four new brown dwarf companions were discovered, but no planetary mass objects were detected. The null results were used to provide the first statistical constraints on the occurrence of giant planets around M dwarfs, with an upper limit of 10.3% and 16.0% for 1-13 $M_{\rm Jup}$ planets between 10 and 100 AU for the hot-start (Burrows et al. 1997) and cold-start (Marley et al. 2007) evolutionary models, at the 95%

Survey	Bands	N_{star}	Spectral Types	Statistical results
GDPS (Lafrenière et al. 2007)	CH4s	85	FGKM	fraction of stars with at least one planetary-mass object is 0.28 for 10-25 AU, 0.13 for 25-50 AU, and 0.093 for 50-250 AU
L' and M-band survey of sun-like stars (Heinze et al. 2010)	L' and M	54	FGK	<8.1% of stars have three, wide orbit, massive planets
IDPS (Vigan et al. 2012)	CH4s and Ks	42	A	fraction of A-stars with one massive planet (3-14 M_{Jup}) is 5.9-18.8% from 5-320 AU, 68% confidence
NICI (Biller et al. 2013; Wahhaj et al. 2013; Nielsen et al. 2013)	H	~80	BAFGKM	≤6% of stars have 1-20 M_{Jup} planetary-mass objects at semi-major axes of 10-150 AU, 95% confidence
NACO L'-band survey (Rameau et al. 2013a)	L'	59	BAFGKM	1-13 M_{Jup} planets have an occurrence of 10.8% to 24.8% from 1-1000 AU, 68% confidence
SEEDS (Janson et al. 2013; Brandt et al. 2014)	H	~250	BAFGKM	RV planet distribution function cannot extend beyond the maximum semimajor axis of 30-100 AU, 95% confidence
NACO large program (Desidera et al. 2015; Chauvin et al. 2015)	H and Ks	86	FGK	<15% for a >5 M_{Jup} planet between 100-500 AU, and <10% for a >10 M_{Jup} planet between 50-500 AU, 95% confidence
PALMS (Bowler et al. 2015)	H and K	122	M	<10.3% and 16.0% for 1-13 M_{Jup} planets between 10 and 100 AU for hot-start and cold-start models, 95% confidence

Table 1.1 Summary of all major direct imaging surveys, including the planet frequency models ruled out due to statistical analysis.

confidence level.

Table 1.1 compares the targets, observations, and summarizes the results of these surveys. Except for the NACO L'-band survey, these surveys all obtained data in the near infrared (H and Ks-band). Theoretical evolutionary models predicted that planets would have strong methane absorption and little cloud opacity, similar to field brown dwarfs (COND; Baraffe et al. 2003). Thus, detecting a planet in methane absorption was one of the driving motivations for observing in H and Ks-band, rather than longer wavelengths. However, most directly imaged planets do not show evidence of methane absorption (HR8799bcd, 2M1207b; Skemer et al. 2014) and are redder than expected (Galicher et al. 2014), unlike field brown dwarfs of similar effective temperatures. This is likely a contributing factor to the low planet detection rate in these surveys. Additionally, nearly all these surveys agree that the massive, large orbital separation planets around HR 8799 and β Pic are rare.

1.6 This Thesis

The work presented in this thesis aims to build upon the results from previous direct imaging surveys, learning both from the target selection and planet frequency models, while also taking advantage of technological advances. This thesis presents an optimized image processing algorithm, the results of two surveys searching for planets, a significant non-detection of a known planet, and a new detection of an M-dwarf.

Chapter 2
Directly detecting the signal from a very faint planet next to a bright star requires a planet-to-star contrast of $10^{-5} - 10^{-6}$ for young planets in the infrared. Developments in observing modes and post-processing have made us more sensitive to detecting these faint sources. One such image processing development is principal component analysis (PCA: Amara & Quanz 2012; Soummer et al. 2012). This algorithm involves modeling and removing the stellar PSF, allowing a planet signal to shine through. This is achieved by removing linear combinations of principal components, generated from the data itself. We developed and applied our own python PCA pipeline to Fomalhaut narrow band 4.05 μm images from NACO/VLT obtained with the APP coronagraph. We performed a series of tests and determined that optimizing the number of principal components maximizes the signal-to-noise from a planet very close to its parent star. We demonstrate that our PCA pipeline is up to one magnitude more sensitive than the previous analysis method. This work appeared in Meshkat et al. (2014).

Chapter 3
The young nature of directly imaged planets makes them ideal candidates to study the late stages of planet formation. However, relatively few planets have been directly imaged. The reason for the few detections is a combination of factors, including instrument modes, target selection, and poor understanding of the frequency of giant planets.

The "Holey Debris Disk" project was created to determine if debris disks with gaps are signposts for planet formation. These gaps are predicted to be dynamically caused by planets (Chiang et al. 2009) accreting debris material as they form. We obtained data with NACO/VLT, LMIRCAM, CLIO, and NICI. In this chapter we present the analysis of six targets observed with NACO/VLT using the APP coronagraph and processed with our optimized PCA pipeline. We targeted bright debris disks with well covered infrared data, allowing us to model their SEDs. By comparing the inferred radius of the gaps with the sensitivity curves, we determined the upper limit on companions that could be carving out these disks. Though only 15 targets were observed with all the facilities combined, two planets were discovered: HD 95086 b (Rameau et al. 2013b) and HD 106906 b (Bailey et al. 2014). This work appeared in Meshkat et al. (2015)

Chapter 4
(Rameau et al. 2013b) reported the discovery of a 5 Jupiter mass planet around

the star HD 95086. Though confirmed to not be a background source, this point source was only detected in L'-band, leaving us unable to rule out foreground L or T dwarfs. In this chapter we analyze our complimentary H-band data from the NICI instrument on Gemini, which resulted in a significant non-detection. This non-detection in the deep dataset allowed us to place a strict color lower limit of $H - L' > 3.1 \pm 0.5$ mag, ruling out foreground L/T dwarfs and demonstrating just how red, dusty, and cloudy these young planets may be. This work appeared in Meshkat et al. (2013)

Chapter 5
We discovered a companion orbiting the F7V star HD 984 at ~9 AU in L'-band, as part of our A and F star survey. The companion was recovered in L'-band non-coronagraphic imaging data taken a few days later. The mass of direct imaged companions is usually inferred from the luminosity and theoretical evolutionary tracks (Baraffe et al. 2003; Allard et al. 2013; Chabrier et al. 2000), which are extremely sensitive to the age of the system. HD 984 is an F-star in the middle of its main sequence, making it particularly challenging to determine its age. It has been argued to be a kinematic member of the 30 Myr-old Columba group (Malo et al. 2013), however it is possible that HD 984 is a kinematic interloper. We independently estimated a main sequence isochronal age of $2.0^{+2.1}_{-1.8}$ Gyr which does not rely on this kinematic association. Based on the L'-band photometry alone, the two age extrema and the COND evolutionary models (Baraffe et al. 2003), we estimate the companion mass to be between 33 and 120 M_{Jup} (0.03-0.11$M_{\odot}$). To break this degeneracy, we obtained SINFONI $H + K$ integral field spectroscopy data to re-detect and characterize the companion. We compared its spectrum with field dwarfs and concluded that the companion is best fit by an M6.0±0.5 dwarf. This discovery suggests that caution should be used when estimating the masses of companions. This work is submitted.

Chapter 6
We observed thirteen A- and F-stars searching for sub-stellar companions with the APP on NACO/VLT. In addition to new companion detections, we aim to set direct imaging constraints on the frequency of sub-stellar companions as a function of stellar mass. The occurrence of giant planets is often extrapolated from radial velocity results to direct imaging surveys, however these two detection methods may probe very different planet populations (Vigan et al. 2012). We detected three low-mass companions, including one new M-dwarf (see Chapter 5). We ran Monte Carlo simulations to place constraints on the planet occurrence models for solar and A-type stars. Based on our non-detection of substellar companions in this survey, we reject the A-type star planet frequency for $r_{cutoff} > 80$AU, with 95% confidence. We also compare APP coronagraphic data with non-coronagraphic data, in order to assess when the APP outperformed direct imaging. This work is submitted.

Chapter 7
We discuss the future of direct imaging, including new instruments, coronagraphs,

image processing techniques, and targets.

References

Acke, B., Min, M., Dominik, C., et al. 2012, A&A, 540, A125

Alexander, R., Pascucci, I., Andrews, S., Armitage, P., & Cieza, L. 2014, Protostars and Planets VI, 475

Alibert, Y., Mordasini, C., & Benz, W. 2011, A&A, 526, A63

Allard, F., Homeier, D., Freytag, B., et al. 2013, Memorie della Societa Astronomica Italiana Supplementi, 24, 128

Amara, A., & Quanz, S. P. 2012, MNRAS, 427, 948

Bailey, V., Meshkat, T., Reiter, M., et al. 2014, ApJL, 780, L4

Baraffe, I., Chabrier, G., Barman, T. S., Allard, F., & Hauschildt, P. H. 2003, A&A, 402, 701

Batalha, N. M., Rowe, J. F., Bryson, S. T., et al. 2013, ApJS, 204, 24

Bergin, E. A., & Tafalla, M. 2007, ARA&A, 45, 339

Biller, B. A., Close, L. M., Masciadri, E., et al. 2007, ApJS, 173, 143

Biller, B. A., Liu, M. C., Wahhaj, Z., et al. 2013, ApJ, 777, 160

Boley, A. C. 2009, ApJL, 695, L53

Boss, A. P. 1998, ApJ, 503, 923

Bowler, B. P., Liu, M. C., Shkolnik, E. L., & Tamura, M. 2015, ApJS, 216, 7

Brandt, T. D., McElwain, M. W., Turner, E. L., et al. 2014, ApJ, 794, 159

Brauer, F., Dullemond, C. P., & Henning, T. 2008, A&A, 480, 859

Burrows, A., Sudarsky, D., & Hubeny, I. 2004, ApJ, 609, 407

Burrows, A., Marley, M., Hubbard, W. B., et al. 1997, ApJ, 491, 856

Chabrier, G., Baraffe, I., Allard, F., & Hauschildt, P. 2000, ApJ, 542, 464

Chauvin, G., Lagrange, A.-M., Dumas, C., et al. 2004, A&A, 425, L29

Chauvin, G., Vigan, A., Bonnefoy, M., et al. 2015, A&A, 573, A127

Chiang, E., Kite, E., Kalas, P., Graham, J. R., & Clampin, M. 2009, ApJ, 693, 734

Desidera, S., Covino, E., Messina, S., et al. 2015, A&A, 573, A126

Fergus, R., Hogg, D. W., Oppenheimer, R., Brenner, D., & Pueyo, L. 2014, ApJ, 794, 161

Fortney, J. J., & Nettelmann, N. 2010, Space Science Reviews, 152, 423

Fressin, F., Torres, G., Charbonneau, D., et al. 2013, ApJ, 766, 81

Galicher, R., Rameau, J., Bonnefoy, M., et al. 2014, A&A, 565, L4

Guillot, T. 2005, Annual Review of Earth and Planetary Sciences, 33, 493

Hayashi, C. 1981, in IAU Symposium, Vol. 93, Fundamental Problems in the Theory of Stellar Evolution, ed. D. Sugimoto, D. Q. Lamb, & D. N. Schramm, 113–126

Heinze, A. N., Hinz, P. M., Kenworthy, M., et al. 2010a, ApJ, 714, 1570

Heinze, A. N., Hinz, P. M., Sivanandam, S., et al. 2010b, ApJ, 714, 1551

Hinkley, S., Oppenheimer, B. R., Soummer, R., et al. 2009, ApJ, 701, 804

Janson, M., Brandt, T. D., Moro-Martín, A., et al. 2013, ApJ, 773, 73

Johnson, J. A., Butler, R. P., Marcy, G. W., et al. 2007, ApJ, 670, 833

Kalas, P., Graham, J. R., & Clampin, M. 2005, Nature, 435, 1067

Kalas, P., Graham, J. R., Chiang, E., et al. 2008, Science, 322, 1345

Kenworthy, M., Quanz, S., Meyer, M., et al. 2010, The Messenger, 141, 2

Konopacky, Q. M., Barman, T. S., Macintosh, B. A., & Marois, C. 2013, Science, 339, 1398

Kraus, A. L., & Ireland, M. J. 2012, ApJ, 745, 5

Krijt, S., Ormel, C. W., Dominik, C., & Tielens, A. G. G. M. 2015, A&A, 574, A83

Kuzuhara, M., Tamura, M., Kudo, T., et al. 2013, ApJ, 774, 11

Lafrenière, D., Jayawardhana, R., & van Kerkwijk, M. H. 2008, ApJL, 689, L153

Lafrenière, D., Marois, C., Doyon, R., Nadeau, D., & Artigau, É. 2007a, ApJ, 660, 770

Lafrenière, D., Doyon, R., Marois, C., et al. 2007b, ApJ, 670, 1367

Lagrange, A.-M., Gratadour, D., Chauvin, G., et al. 2009, A&A, 493, L21

Lagrange, A.-M., Bonnefoy, M., Chauvin, G., et al. 2010, Science, 329, 57

Lin, D. N. C., Bodenheimer, P., & Richardson, D. C. 1996, Nature, 380, 606

Lissauer, J. J., Dawson, R. I., & Tremaine, S. 2014, Nature, 513, 336

Lyot, B. 1939, MNRAS, 99, 580

Malo, L., Doyon, R., Lafrenière, D., et al. 2013, ApJ, 762, 88

Marley, M. S., Fortney, J. J., Hubickyj, O., Bodenheimer, P., & Lissauer, J. J. 2007, ApJ, 655, 541

Marois, C., Lafrenière, D., Doyon, R., Macintosh, B., & Nadeau, D. 2006, ApJ, 641, 556

Marois, C., Macintosh, B., Barman, T., et al. 2008, Science, 322, 1348

Marois, C., Macintosh, B., & Véran, J.-P. 2010, in Society of Photo-Optical Instrumentation Engineers (SPIE) Conference Series, Vol. 7736, Society of Photo-Optical Instrumentation Engineers (SPIE) Conference Series

Matthews, B., Kennedy, G., Sibthorpe, B., et al. 2014, ApJ, 780, 97

Mayer, L., Quinn, T., Wadsley, J., & Stadel, J. 2002, Science, 298, 1756

Mayer, L., Wadsley, J., Quinn, T., & Stadel, J. 2005, MNRAS, 363, 641

Mayor, M., & Queloz, D. 1995, Nature, 378, 355

Meshkat, T., Bailey, V. P., Su, K. Y. L., et al. 2015, ApJ, 800, 5

Meshkat, T., Kenworthy, M. A., Quanz, S. P., & Amara, A. 2014, ApJ, 780, 17

Meshkat, T., Bailey, V., Rameau, J., et al. 2013, ApJL, 775, L40

Naud, M.-E., Artigau, É., Malo, L., et al. 2014, ApJ, 787, 5

Nielsen, E. L., Liu, M. C., Wahhaj, Z., et al. 2013, ApJ, 776, 4

Okuzumi, S., Tanaka, H., Kobayashi, H., & Wada, K. 2012, ApJ, 752, 106

Pollack, J. B., Hubickyj, O., Bodenheimer, P., et al. 1996, Icarus, 124, 62

Quanz, S. P., Amara, A., Meyer, M. R., et al. 2013, ApJL, 766, L1

Rameau, J., Chauvin, G., Lagrange, A.-M., et al. 2013a, A&A, 553, A60

—. 2013b, ApJL, 779, L26

—. 2013c, ApJL, 772, L15

Rasio, F. A., Tout, C. A., Lubow, S. H., & Livio, M. 1996, ApJ, 470, 1187

Rieke, G. H., Su, K. Y. L., Stansberry, J. A., et al. 2005, ApJ, 620, 1010

Rouan, D., Riaud, P., Boccaletti, A., Clénet, Y., & Labeyrie, A. 2000, PASP, 112, 1479

Safronov, V. S., & Zvjagina, E. V. 1969, Icarus, 10, 109

Skemer, A. J., Marley, M. S., Hinz, P. M., et al. 2014, ApJ, 792, 17

Soummer, R., Pueyo, L., & Larkin, J. 2012, ApJL, 755, L28

Spiegel, D. S., & Burrows, A. 2012, ApJ, 745, 174

Vigan, A., Patience, J., Marois, C., et al. 2012, A&A, 544, A9

Wahhaj, Z., Liu, M. C., Nielsen, E. L., et al. 2013, ApJ, 773, 179

Weidenschilling, S. J. 1977, MNRAS, 180, 57

Wyatt, M. C. 2008, ARA&A, 46, 339

Chapter 2

Optimized Principal Component Analysis on Coronagraphic Images of the Fomalhaut System

We present the results of a study to optimize the Principal Component Analysis (PCA) algorithm for planet detection, a new algorithm complementing angular differential imaging and locally optimized combination of images (LOCI) for increasing the contrast achievable next to a bright star. The stellar PSF is constructed by removing linear combinations of principal components, allowing the flux from an extrasolar planet to shine through. The number of principal components used determines how well the stellar PSF is globally modeled. Using more principal components may decrease the number of speckles in the final image, but also increases the background noise. We apply PCA to Fomalhaut Very Large Telescope NaCo images acquired at 4.05 μm with an apodizing phase plate. We do not detect any companions, with a model dependent upper mass limit of 13–18 M_{Jup} from 4–10 AU. PCA achieves greater sensitivity than the LOCI algorithm for the Fomalhaut coronagraphic data by up to 1 mag. We make several adaptations to the PCA code and determine which of these prove the most effective at maximizing the signal-to-noise from a planet very close to its parent star. We demonstrate that optimizing the number of principal components used in PCA proves most effective for pulling out a planet signal.

T. Meshkat, M. A. Kenworthy, S. P. Quanz, A. Amara

2.1 Introduction

The detection and characterization of extrasolar planets has grown dramatically as a field since the first detection in 1992 (Wolszczan & Frail 1992). The most successful detection techniques thus far are radial velocity (RV) and transit detection. Using ground and space based surveys (HARPS, *Kepler*, COROT, etc.), these indirect techniques have discovered over 800 planets (exoplanet.eu) as well as thousands more planet candidates.

The direct detection of planets provides a unique opportunity to study exoplanets in the context of their formation and evolution. It complements the underlying semi-major axis exoplanet distribution from RV surveys (from 100 AU down to a few AUs) and enables the characterization of the planet itself with an examination of its emergent flux as a function of wavelength. The detection of the planets HR8799 bcde (Marois et al. 2008), Fomalhaut b (Kalas et al. 2008), β Pic b (Lagrange et al. 2009), 2MASS1207 (Chauvin et al. 2004), 1RXS J1609–2105 b (Lafrenière et al. 2008), HD 95086 b (Rameau et al. 2013b), KOI-94 (Takahashi et al. 2013) as well as discoveries of protoplanetary candidates LkCa 15 b (Kraus & Ireland 2012) and HD100546 b (Quanz et al. 2013), demonstrate the potential breakthroughs of the technique. However, thus far, most dedicated high contrast imaging surveys have yielded null results (e.g., Rameau et al. 2013a; Vigan et al. 2012; Chauvin et al. 2010; Biller et al. 2007; Heinze et al. 2008). These null results are due to the lack of contrast at small orbital separations, where most planets are expected to be found. Since planets are concluded to be rare at large orbital separations (Chauvin et al. 2010; Lafrenière et al. 2007), high contrast imaging must probe close to the parent star to detect a planet.

High contrast imaging is limited by the diffraction limit, set by the telescope optics, which determines the minimum angular separation achievable under ideal conditions. Since planets are low mass, cold, and red compared to their parent star (Spiegel & Burrows 2012; Baraffe et al. 2003), the contrast ratio of their magnitudes is an additional constraint on their detectability. New instruments and techniques have been developed to combat these constraints at the acquisition and image processing stage.

Coronagraphs have been developed to reduce the light scattered in the telescope optics from diffraction during acquisition, but at a cost of throughput and angular resolution (Guyon et al. 2005). Coronagraphic optics allow us to probe smaller inner working angles, but are limited by the stellar "speckles" which can dominate the flux from a planet (Hinkley et al. 2009).

By turning off the telescope derotator on an alt-az telescope, the planet is able to "rotate" around the star, while the stellar PSF stays relatively stable and the speckles vary randomly in time. This technique is used in angular differential imaging (ADI; Marois et al. 2008). It takes advantage of this rotation to identify and subtract (in post-processing) the contribution from the stellar PSF and speckles. There are a number of image processing techniques aimed at modeling and subtracting the stellar PSF from every image, allowing the sky fixed planet signal to shine through. Locally optimized combination of images (LOCI; Lafrenière et al. 2007) is an extension of ADI, which models the local stellar PSF structure in every
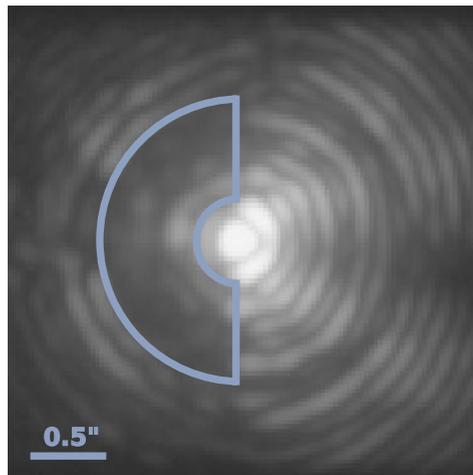
Figure 2.1 Image demonstrating the APP airy diffraction pattern with the diffraction suppressed region outlined in blue. This is the only region that is used in the data reduction.

image. Principal component analysis (PCA; Amara & Quanz 2012; Soummer et al. 2012; Brandt et al. 2013) models how the PSF varies in time by identifying the main linear components of the variation. Application of these image processing techniques has been demonstrated to increase the limiting magnitude achievable by up to a factor of five (Lafrenière et al. 2007; Amara & Quanz 2012).

In this work, we present a detailed study of LOCI and PCA image processing techniques in order to optimize the signal-to-noise ratio (S/N) of a planet at small angular separations with the apodizing phase plate (APP) coronagraph (Kenworthy et al. 2010, 2007). We compare our results to the previous result of Kenworthy et al. (2013).

The Fomalhaut dataset that is used in the following analyses are a deep but typical observing sequence and will act as an example for the rest of our surveys.

2.2   Data

Data were obtained of the star Fomalhaut at the Very Large Telescope (VLT)/UT4 with NaCo (Lenzen et al. 2003; Rousset et al. 2003) in 2011 July and August (087.C–0701(B)) and were analyzed and published in Kenworthy et al. (2013). Fomalhaut was used as the natural guide star with the visible band wavefront sensor. The L27 camera on NaCo was used with the $NB4.05$ filter ($\lambda = 4.051\mu$m and $\Delta\lambda = 0.02\mu$m) and the APP coronaraph (Kenworthy et al. 2010; Quanz et al. 2010) to provide additional diffraction suppression. We used pupil tracking mode to perform ADI (Marois et al. 2006). The PSF core is intentionally saturated to increase the signal from any potential companions.

The APP provides diffraction suppression over a 180° wedge on one side of the

target (Figure 2.1). Additional observations are required with a different position angle (P.A.) to cover the full 360° around the star. For these observations, we have three different datasets with different P.A.s ensuring full P.A. coverage around the target star. Each dataset has a large amount of field rotation: 119°, 117°, 120°.

Data were acquired in cube mode. Each data cube contains 200 frames, each with an integration time of 0.23 s. Approximately 70 cubes were obtained for each hemisphere dataset, totaling in an integration time of 160 minutes. A three point dither pattern was used to allow subtraction of the sky background and detector systematics as detailed in Kenworthy et al. (2013). Unsaturated short exposure data with the neutral density filter were also taken for photometry.

2.3 Creating the Simulated Data–Sets

Data cubes at each dither position were pairwise subtracted to remove the sky background and detector systematics. The cubes were shifted to move the core PSF into the middle of a square image and bad frames (open loop and poor AO) were discarded (5% of hemisphere 1, 16% of hemisphere 2, and 7% of hemisphere 3). The three different APP P.A. datasets were processed separately. Each hemisphere dataset has its own corresponding unsaturated data for photometry.

Fake planets are subsequently used to determine the limiting contrast after image processing. The unsaturated Fomalhaut data is used to add a fake planet in each saturated frame. One fake planet is added at a time, between $0\rlap{.}''2$ and $1\rlap{.}''0$ in steps of $0\rlap{.}''1$ and δ magnitudes in steps of 1 mag from $dM = 7$–13. Due to the asymmetric nature of the APP PSF, it is also necessary to determine the S/N of a planet at different P.A.s. For our analysis we placed a planet on opposite sides of the star (P.A.=45° and 225° relative to the sky) to take into account the asymmetric PSF of the APP. These two P.A. orientations ensure that the planet is on the dark side of the APP in at least two of the hemispheres at once. The mean of the limiting contrast at each P.A. is stored.

The final science frames are processed with several different algorithms to recover the fake planet signal. All of the algorithms take advantage of the fake planet's rotation in the sky around the star to model and subtract the stellar PSF from each image (ADI; Marois et al. 2006). Before each algorithm is applied, the innermost region is masked out ($r < 0\rlap{.}''15$) where the star has saturated the image and no planet could be detected. The method of modeling the stellar PSF differs between the algorithms, detailed in the following subsections.

One metric for detectability of planets is S/N. It is a measure of the detectability of a point source, assuming the noise is Gaussian and decorrelated between diffraction limited elements at that radius. The equation below is similar to those in the literature, describing local S/N:

$$\left(\frac{\mathrm{S}}{\mathrm{N}}\right)_{\mathrm{planet}} = \frac{F_{\mathrm{planet}}}{\sigma(r)\sqrt{\pi r_{\mathrm{ap}}^2}},$$

where F_{planet} is the sum of the planet flux in an aperture with radius $r_{\mathrm{ap}} = 3$ pixels and σ is the root mean square of the pixels in a 180°, 6 pixel wide arc at

the same radius, surrounding the star.

The equation above assumes statistically independent pixels, which in the case of speckle noise limited regimes is typically not the case. For the sake of consistency with other papers in the literature, we use one of the most common definitions of S/N calculation to facilitate comparison with other methods. This is a widely acknowledged issue in this research field, so while the S/N quoted may be off by a scaling factor, the conclusions in this paper do not rely on the absolute scaling as we are comparing analysis techniques.
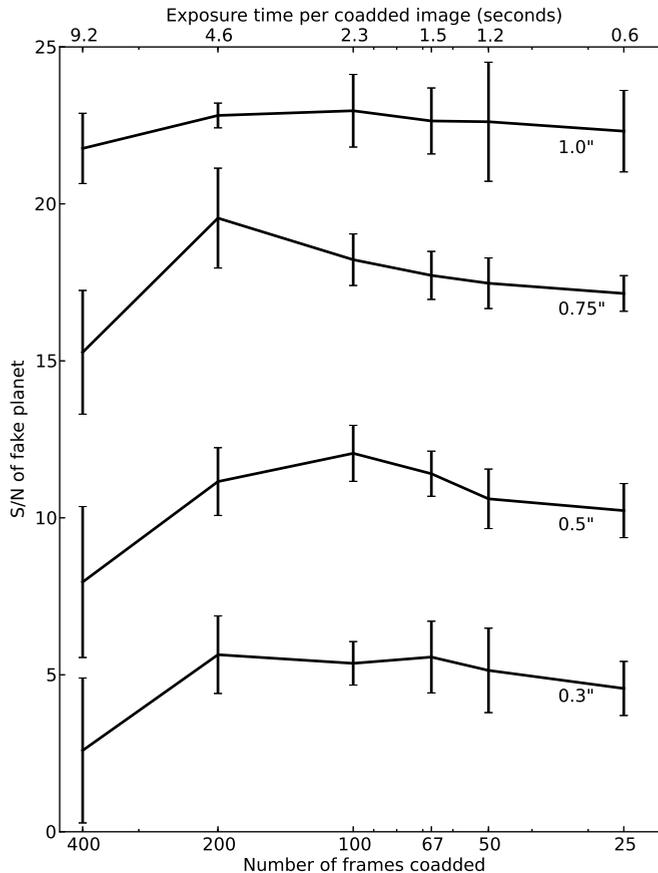
2.4   Data Analysis

Figure 2.2 Signal-to-noise ratio curves for a fake planet at four angular separations, with different amounts of frames coadded. At each angular separation, planets were added at four position angles and averaged. The error bars are $1\ \sigma$. The number of PCs is fixed at 20. Each contrast curve is offset from a S/N of 10 for clarity.

Coadding the frames in a data cube is a common practice but the best number of frames to coadd has not yet been thoroughly studied. We experimented with different numbers of coadded frames using fake planets. We ran the data through our PCA pipeline (detailed in Section 2.4.2) with different numbers of frames coadded (Figure 2.2). For example, 100 frames coadded means that twice as many images are passed to our pipeline as in the 200 coadded frames case. Figure 2.2 shows four S/N curves for planets injected a different angular separations, each with a S/N of approximately 10. The curves are offset from 10 for clarity. Coadding 200 or less frames yields a higher S/N. However, the S/N varies by less than a factor of two over all coadds, making this a relatively small effect. For the following analysis, we keep the coadds fixed at 200 frames, which yields S/N as good as less coadds, but is computationally much faster. This corresponds to ~70 coadded images in each hemisphere which are passed to our pipeline. Since there is little field rotation between individual frames in a data cube, the smearing effect within a cube is negligible.

2.4.1 LOCI

Locally optimized combination of images (Lafrenière et al. 2007) is a widely used planet detection algorithm which spatially models the stellar PSF to remove speckles. An image is divided into rings, which are subdivided into wedges. An optimal, linear combination of images subtracts speckles within that region. The least squares fit succeeds at minimizing speckles, but also reduces the planet flux through the subtraction for small angular separations.

Each hemisphere dataset is processed with LOCI independently and the final three hemisphere sky aligned cubes are collapsed. Since we are using the APP, we only perform LOCI on the "dark side" of the image frames. This 180° D shaped region (inner=$2\lambda/D$, outer=$7\lambda/D$) is the only part of each frame that is coadded in the final image.

Kenworthy et al. (2013) analysis of these data used the LOCI algorithm. Monte Carlo simulations exploring LOCI parameters ensured that this is the best sensitivity LOCI could produce.

2.4.2 Principal Component Analysis

Principal component analysis is a mathematical technique that relies on the assumption that every image in a stack can be represented as a linear combination of its principal orthogonal components, selecting structures that are present in most of the images. Its recent application to high contrast exoplanet imaging (Amara & Quanz 2012; Soummer et al. 2012) has been shown to be very effective. Unlike LOCI (Lafrenière et al. 2007) which models the local stellar PSF structure, PCA models the global PSF structure.

The full stack of images with sky rotation is used for PCA. However, since we are using the APP, only the "dark side" of each image is used in the fit. The S/N from a fake planet is lower if we include the "bright side". We follow the description of PCA outlined in Amara & Quanz (2012) for the following analysis.
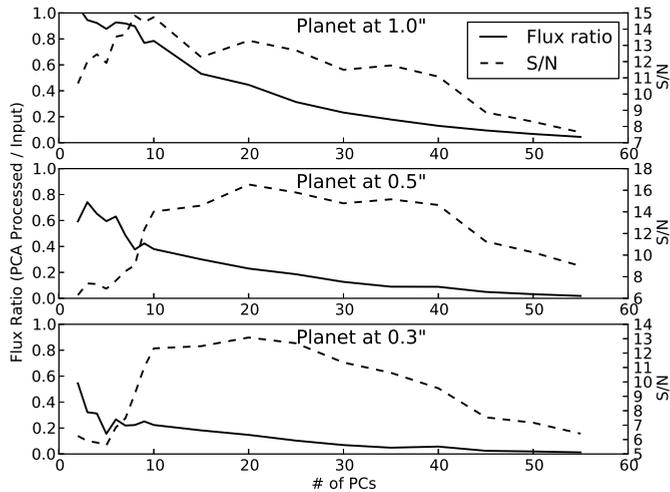
Figure 2.3 Comparison of the flux ratio and S/N based on number of PCs at different radii. The top panel is for a fake planet at 1″0, the middle panel is for 0″5 and the bottom panel is for 0″3. These panels demonstrate that, while the flux ratio does decrease with PCs, the S/N follows a different curve.

The number of PCs used determines how well the stellar PSF is fit. The first few components are the most stable, have less noise, and contain the most common structure in all the images. For our default analysis, we used 20 PCs to model the stellar PSF. PCA is run on each hemisphere dataset independently, as the PCs are correlated with time. The final de-rotated frames are coadded into one final image covering the full 360° around the star.

The following subsections discuss self-subtraction due to the PCA algorithm as well as a series of modifications we performed on PCA to optimize the detection of a planet at small λ/D.

Self-subtraction

Self-subtraction from the LOCI algorithm has been well documented by previous authors (Lafrenière et al. 2007; Marois et al. 2010), but its impact on PCA is not yet well studied. The LOCI algorithm requires that the frames nearest in time to the current frame are not considered in the least squares fit, thus limiting the self-subtraction of a potential planet. However, this frame rejection technique does not completely account for flux loss from a planet.

For our PCA analysis, we draw a distinction between two types of modes: detection and characterization. Characterization mode requires fully accounting for flux loss of the planet as a function of number of PCs as we map between the measured flux and the calibrated estimate of "true" flux. However, in detection mode, since we only care about our ability to separate the planet signal from the background noise, the main issue is the flux loss relative to the separation of the
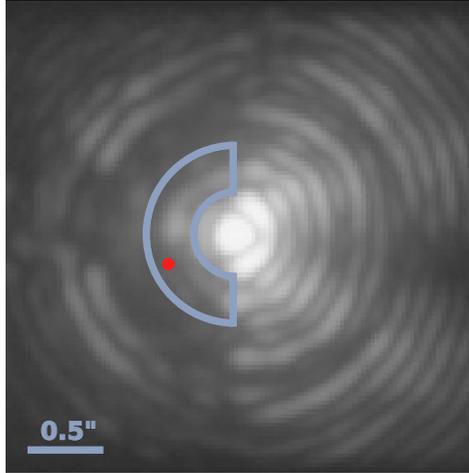
Figure 2.4 Image demonstrating the APP airy diffraction pattern with the radius limited region outlined in blue. This is the only region that is used in the data reduction.

background noise. In this paper, we address simply the detection mode.

Figure 2.3 shows three plots with the flux ratio and S/N versus the number of PCs it was processed with. The top figure is for a planet injected at $1''0$, middle is at $0''5$ and bottom is at $0''3$. The "flux ratio" is the ratio of the injected planet flux to the PCA processed flux in a 4 pixel aperture. For each angular separation, the L' contrast which yields a S/N of approximately 10 is plotted. This figure demonstrates that the PCA method is more efficient at capturing the patterns associated with the background fluctuations of the field than capturing information associated with the planet translation. This differential effect means that in detection mode, it is acceptable for the flux ratio to decrease as long as the noise is decreasing as or more rapidly.

PCA Modifications

1. *Frame Rejection*

   For our PCA code detailed above, all the frames are used in the fit and none are rejected. This was done under the assumption that self-subtraction of the planet happens less rapidly than the noise subtraction when using PCA. As discussed in Section 2.4.2, while we are in "detection mode", the important factor to consider is the S/N rather than planet flux. To test this, we used only a subset of the frames to determine the PCs. The frames nearest in time to the frame being fitted were rejected. These are frames where a potential planet would overlap by 0.5 FWHM or more. The number of frames to reject depends on the separation of the planet from the star. The total rotation of the planet is limited by the amount of sky rotation achieved during each dataset. A planet very far from its parent star
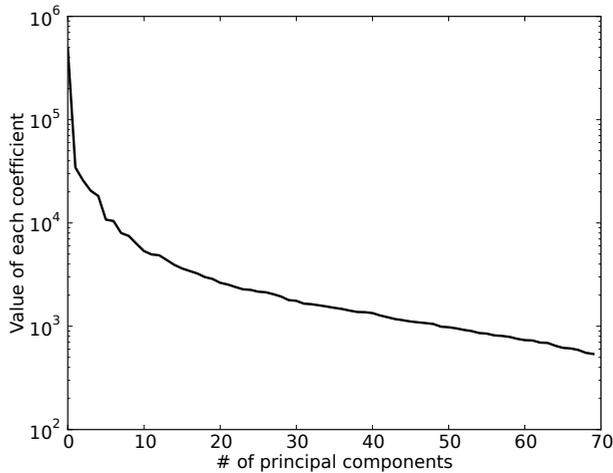
Figure 2.5 Plot of the PCA coefficient values. The highest PCA coefficient value corresponds to the most significant PC.

would appear to rotate faster between frames, thus less frames need to be rejected. This test allows us to compare the S/N of a fake planet processed with standard PCA and "0.5 FWHM rejection", where we mimic the routine in LOCI to reject the frames closest in time.

2. *Radius Limited*

   Next, we modified the PCA basis set by only using the image out to a certain radius. The outer radius (R_{out}) passed to the PCA code determines the amount of information provided to the SVD algorithm. Extra information does not necessarily provide a better fit. Our previous applications of PCA kept R_{out} fixed. The information passed to the SVD algorithm should be directly related to the stellar PSF. We modified our PCA code to vary R_{out} based on the location of the fake planet. The new R_{out} is 1 λ/D greater than the radius of the fake planet (see Figure 2.4), thus performing PCA on a smaller region. This experiment was performed to test how significant the stellar PSF fit was affected by radii greater than the planet location.

3. *Number of PCs*

   The main parameter which can be manipulated in PCA is the number of PCs used in the SVD fit. The first principal value (the highest singular value in the diagonal matrix) is the "variance" of the image stack from the mean, in the direction of the first PC. The same is true about the second principal value and so on.

   Figure 2.5 shows the PCA coefficient values in descending order for one of our datasets. The first few PCA coefficient values are significantly greater than the
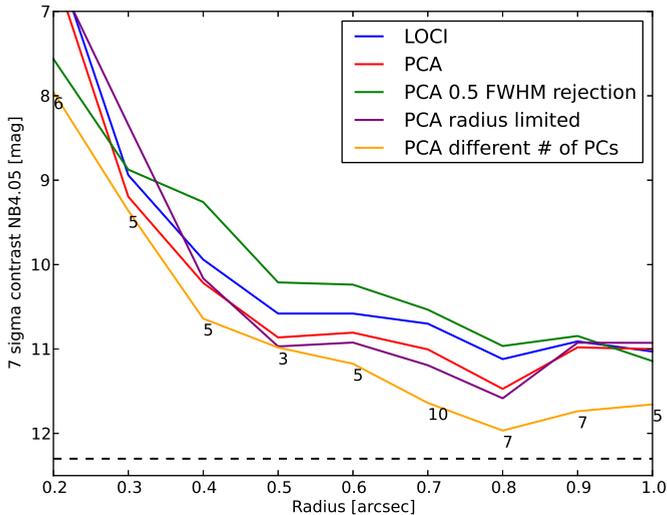
Figure 2.6 Contrast curves for a 7σ detection of a point source in our Fomalhaut APP data processed with LOCI, ADI, and variations of ADI. The LOCI curve is adapted from Kenworthy et al. (2013) to a 7σ detection. The numbers on the yellow curve signify the number of PCs which yield the highest S/N at that radius. The dashed line is the background limit. The PCA contrast curves are the mean value for fake planets inserted at two P.A.s on opposite sides of the star (P.A.=45° and 225°).

later values, implying that those PCs contain the most dominant features. Increasing the number of PCs in the stellar PSF fit can help bring out the planet signal by removing structure, however it also can add noise. Determining the optimal number of PCs for a certain stellar PSF fit is an essential but expensive task. The optimal number of PCs depends on the time variability of complex speckles.

For each dataset and fake planet angular separation, PCA was run with different numbers of PCs ranging from 5 to 60, in increments of 5.

2.5   Results and Discussion

Figure 2.6 shows the results of each image processing method detailed in Section 2.4.2. Each technique was run with varying planet contrasts at a given radius. We extrapolated between planet contrasts to determine contrast that yields a S/N of 7. For the method with varying PCs detailed in Section 2.4.2, we noted which number of PCs yielded the highest S/N at which radius. These are the numbers listed on the yellow curve in Figure 2.6.

Our standard PCA technique yields a better contrast curve than LOCI for our coronagraphic data. Our modifications to PCA, in some cases, yield better sensitivity.

Figure 2.7 Three-dimensional surface of the contrast achieved in a 7σ detection with varied numbers of PCs. Varying the number of PCs at small angular separations affects the 7σ detection limit by up to 8 mag. Beyond 0.″6, the number of PCs used is less significant.
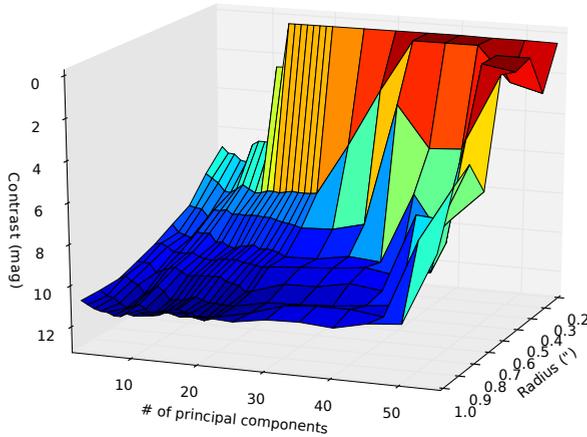
Unlike the LOCI algorithm, rejecting the frames nearest in time (detailed in Section 2.4.2) yields a worse contrast curve than our standard PCA. This is likely due to the noise being more correlated in frames closer in time, thus providing important information to the SVD algorithm and increasing the S/N of the planet. We did not reject any frames in our final data analysis approach.

Limiting the outer radius passed to the SVD algorithm yielded a slightly better contrast ratio than standard PCA from 0.″5 to 0.″8. However, this contrast increase is not significant and is only beneficial because it is less computationally expensive.

Our standard PCA contrast curve was generated with 20 PCs. By varying the number of PCs we can increase the S/N from a companion. Our PC-varying result yields a consistently more sensitive contrast curve then all the other methods. We gain between 0.5 and 1 mag contrast over our LOCI analysis from 0.″2 to 1.″0. From Figure 2.6 we see that the number of PCs which yield the highest S/N for a planet varies based on its angular separation.

Figure 2.7 is a three-dimensional (3D) surface plot showing how the number of PCs at each radius affects the contrast at 7σ for a planet at a fixed P.A. Fake planets were added between 2 and 20 PCs in smaller steps to emphasize the structure. This figure demonstrates that at small angular separations ($< 0.″6$), the S/N is sensitive to the number of PCs chosen. This is the region where the diffraction and speckles due to the star are more significant than the unstructured noise from thermal emission and the sky background. For example, at 0.″2 choosing a small number of PCs yields an 8 mag gain in sensitivity than a large number of PCs. Increasing the number of PCs quickly leads to nearly complete self-subtraction.
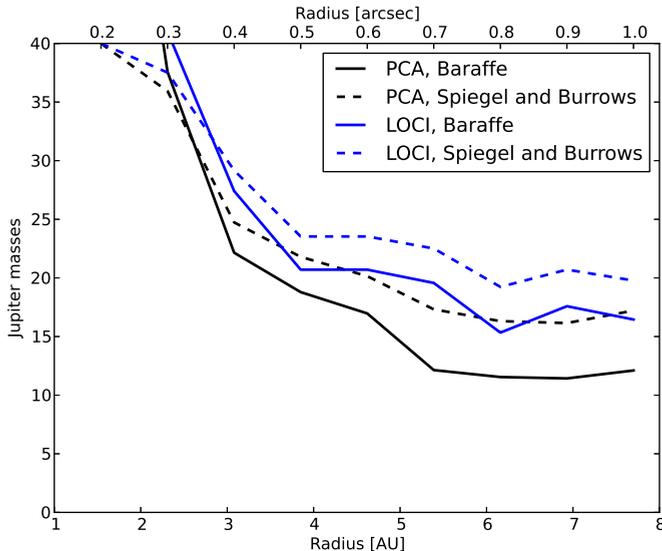
Figure 2.8 Detection limit for fake companions around Fomalhaut generated with PCA (black lines) and LOCI (blue lines, converted to 7σ detection from Kenworthy et al. 2013) using (Baraffe et al. 2003, solid lines) and (Spiegel & Burrows 2012, dashed lines).

This can be seen in Figure 2.7 as a contrast of nearly zero. As we move to larger radii the optimal number of PCs remains in the 5–20 PC range. Beyond $0\rlap{.}''6$ where the number of PCs shows no significant preference below 45 PCs.

2.5.1 Comparison with Kenworthy et al. (2013)

Our PCA re-analysis of these data improves sensitivity at small inner working angles, from $0\rlap{.}''2$ to 1", in some cases by 1 mag (see blue and yellow curves, Figure 2.6). We convert the best 7σ detection contrast curve to an upper mass limit for planets using the Baraffe et al. (2003) and Spiegel & Burrows (2012) atmospheric models (Figure 2.8) assuming an age of 440 Myr (Mamajek et al. 2012). We confirm the non-detection of companions with a model-dependent upper mass limit of 13–18 $M_{\rm Jup}$ from 4–10 AU. Our new upper mass limit is based on our more robust 7σ detection limit. The 1 mag increase in the contrast ratio at $0\rlap{.}''5$ translates to an increased sensitivity of $\Delta\,7\,M_{\rm Jup}$. The increase in sensitivity allows us to probe planetary masses ($<15\,M_{\rm Jup}$) at small angular separations.

2.5.2 Fainter Fomalhaut

We have shown that the number of PCs which yield the highest S/N depends on the planet's distance from the parent star (yellow line, Figure 2.6). At small angular separations ($<\,0\rlap{.}''6$), the S/N is sensitive to the number of PCs chosen
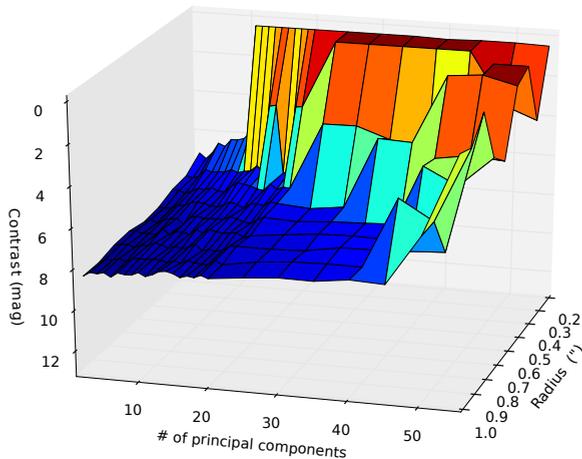
Figure 2.9 Similar to the 3D surface in Figure 2.7, but with Gaussian white noise added to the data. The resulting star is 1.5 mag fainter than Fomalhaut.

(Figure 2.7). This is the limit where the diffraction from the central star is equal to or less significant than the background noise.

We add Gaussian white noise to our data to test if this turnover point changes for a fainter target (Figure 2.9). Increasing the sky background noise makes Fomalhaut 1.5 mag fainter, while keeping the telescope conditions and Strehl identical. This is the ideal way to test how fainter targets will behave. Fake planets are once again injected and the best number of PCs at each angular separation is noted.

Changing the number of PCs used at each angular separation is still the best method for detecting companions. As expected, the regime of large numbers of PCs at small separations results in low contrast, which then improves down to a plateau at smaller PCs and larger radii. The turnover point remains near $0\rlap{.}''6$, beyond which the diffraction from the star is no longer significant and the optimal number of PCs is less clear. Beyond this separation, the background noise dominates the SVD fit and thus does not help subtract the stellar PSF.

2.6 Conclusion

We re-analyze our Fomalhaut APP/NaCo/NB4.05 data using PCA and compare it with the LOCI algorithm. PCA yields a more sensitive contrast curve than the LOCI algorithm at small inner working angles. We tested several modifications to PCA and gain up to 1 mag of contrast over our LOCI analysis from $0\rlap{.}''2$ to $1\rlap{.}''0$. The most effective parameter which optimized PCA was varying the number of principal components. The number of principal components chosen is sensitive for planets at small inner working angles. The detection limit of a planet at

small radii can vary by several magnitudes. Careful attention should be paid to determining the number of principal components used at radii where the speckles are more significant than the unstructured noise of thermal emission and the sky background. Running PCA for a range of principal components at each angular separation and generating a 3-D surface is a useful way to visualize the optimal number of principal components needed to pull out a faint planet signal.

Further analysis is needed in other wavelengths, as differing Strehl ratios may affect the turnover point where the stellar diffraction is less significant than the background noise. These results have direct application for current and future planet imaging campaigns, which will likely use a combination of PCA, LOCI, and other image processing techniques.

Acknowledgements

References

Amara, A., & Quanz, S. P. 2012, MNRAS, 427, 948

Baraffe, I., Chabrier, G., Barman, T. S., Allard, F., & Hauschildt, P. H. 2003, A&A, 402, 701

Biller, B. A., Close, L. M., Masciadri, E., et al. 2007, ApJS, 173, 143

Brandt, T. D., McElwain, M. W., Turner, E. L., et al. 2013, ApJ, 764, 183

Chauvin, G., Lagrange, A.-M., Dumas, C., et al. 2004, A&A, 425, L29

Chauvin, G., Lagrange, A.-M., Bonavita, M., et al. 2010, A&A, 509, A52

Guyon, O., Pluzhnik, E. A., Galicher, R., et al. 2005, ApJ, 622, 744

Heinze, A. N., Hinz, P. M., Kenworthy, M., Miller, D., & Sivanandam, S. 2008, ApJ, 688, 583

Hinkley, S., Oppenheimer, B. R., Soummer, R., et al. 2009, ApJ, 701, 804

Kalas, P., Graham, J. R., Chiang, E., et al. 2008, Science, 322, 1345

Kenworthy, M. A., Codona, J. L., Hinz, P. M., et al. 2007, ApJ, 660, 762

Kenworthy, M. A., Meshkat, T., Quanz, S. P., et al. 2013, ApJ, 764, 7

Kenworthy, M. A., Quanz, S. P., Meyer, M. R., et al. 2010, in Society of Photo-Optical Instrumentation Engineers (SPIE) Conference Series, Vol. 7735, Society of Photo-Optical Instrumentation Engineers (SPIE) Conference Series

Kraus, A. L., & Ireland, M. J. 2012, ApJ, 745, 5

Lafrenière, D., Jayawardhana, R., & van Kerkwijk, M. H. 2008, ApJL, 689, L153

Lafrenière, D., Doyon, R., Marois, C., et al. 2007, ApJ, 670, 1367

Lagrange, A.-M., Gratadour, D., Chauvin, G., et al. 2009, A&A, 493, L21

Lenzen, R., Hartung, M., Brandner, W., et al. 2003, in Society of Photo-Optical Instrumentation Engineers (SPIE) Conference Series, Vol. 4841, Society of Photo-Optical Instrumentation Engineers (SPIE) Conference Series, ed. M. Iye & A. F. M. Moorwood, 944–952

Mamajek, E. E., Quillen, A. C., Pecaut, M. J., et al. 2012, AJ, 143, 72

Marois, C., Lafrenière, D., Doyon, R., Macintosh, B., & Nadeau, D. 2006, ApJ, 641, 556

Marois, C., Macintosh, B., Barman, T., et al. 2008, Science, 322, 1348

Marois, C., Macintosh, B., & Véran, J.-P. 2010, in Society of Photo-Optical Instrumentation Engineers (SPIE) Conference Series, Vol. 7736, Society of Photo-Optical Instrumentation Engineers (SPIE) Conference Series

Quanz, S. P., Amara, A., Meyer, M. R., et al. 2013, ApJL, 766, L1

Quanz, S. P., Meyer, M. R., Kenworthy, M. A., et al. 2010, ApJL, 722, L49

Rameau, J., Chauvin, G., Lagrange, A.-M., et al. 2013a, A&A, 553, A60

Rameau, J., Chauvin, G., Lagrange, A.-M., et al. 2013b, ApJL, 772, L15

Rousset, G., Lacombe, F., Puget, P., et al. 2003, in Society of Photo-Optical Instrumentation Engineers (SPIE) Conference Series, Vol. 4839, Society of Photo-Optical Instrumentation Engineers (SPIE) Conference Series, ed. P. L. Wizinowich & D. Bonaccini, 140–149

Soummer, R., Pueyo, L., & Larkin, J. 2012, ApJL, 755, L28

Spiegel, D. S., & Burrows, A. 2012, ApJ, 745, 174

Takahashi, Y. H., Narita, N., Hirano, T., et al. 2013, ArXiv e-prints

Vigan, A., Patience, J., Marois, C., et al. 2012, A&A, 544, A9

Wolszczan, A., & Frail, D. A. 1992, Nature, 355, 145

Searching for Planets in Holey Debris Disks with the Apodizing Phase Plate

We present our first results from a high-contrast imaging search for planetary mass companions around stars with gapped debris disks, as inferred from the stars' bright infrared excesses. For the six considered stars, we model the disks' unresolved infrared spectral energy distributions (SEDs) in order to derive the temperature and location of the disk components. With VLT/NaCo Apodizing Phase Plate coronagraphic L'-band imaging, we search for planetary mass companions that may be sculpting the disks. We detect neither disks nor companions in this sample, confirmed by comparing plausible point sources with archival data. In order to calculate our mass sensitivity limit, we revisit the stellar age estimates. One target, HD 17848, at 540±100 Myr old is significantly older than previously estimated. We then discuss our high-contrast imaging results with respect to the disk properties.

Tiffany Meshkat, Vanessa P. Bailey, Kate Y. L. Su, Matthew A. Kenworthy, Eric E. Mamajek, Philip M. Hinz, Paul S. Smith

3.1 Introduction

Despite the large number of direct imaging surveys (SEEDS: Brandt et al. 2014; Janson et al. 2013, NICI: Biller et al. 2013; Nielsen et al. 2013; Wahhaj et al. 2013, GDPS: Lafrenière et al. 2007, IDPS: Vigan et al. 2012, and with NaCo: Desidera et al. 2014; Chauvin et al. 2014) and the hundreds of sources observed, few planets have been discovered from these surveys (HR8799 bcde from IDPS: Marois et al. 2008, 2010, GJ 504 b from SEEDS; Kuzuhara et al. 2013). This low detection rate is likely due to a combination of factors (e.g. the wavelength of the observations, the target selection, the lack of a dedicated exoplanet instrument, etc). The faint H-band detection of HD 95086 b (Galicher et al. 2014) and the non-detection companion candidate around HD 169142 (Reggiani et al. 2014; Biller et al. 2014) demonstrate that these low mass companions are extremely red. These results reinforce the importance of searching for planets in the thermal infrared with L'-band (3.8 μm), as the planet-to-star contrast is reduced and contamination from background stars is strongly suppressed.

We aim to find a signpost for planets; a trait of the stars or systems which might yield a higher planet detection rate than previous surveys. One possible signpost is the structure of debris disks with gaps, which dynamically may imply the presence of a planet (Quillen & Thorndike 2002; Quillen 2006). This includes both debris systems with a large hole in the center, generally classified as one-component disks, and debris systems with a large gap, generally classified as two-component (warm inner and cool outer) disks (Su & Rieke 2014). We have designed the "Holey Debris Disks" exoplanet direct imaging survey guided by this hypothesis. The targets were selected based on several criteria: youth, distance, brightness, and unresolved infrared excess indicative of the presence of a possibly-sculpted debris disk around the star using Spitzer data (Su et al. 2010). Our constraints on companion masses and locations will provide useful inputs for future debris disk/planet dynamical models.

We present the first results of the Holey Debris Disk survey, obtained at the Very Large Telescope (VLT) with the NaCo[1] (Lenzen et al. 2003; Rousset et al. 2003) instrument and Apodizing Phase Plate coronagraph (APP: Kenworthy et al. 2010; Quanz et al. 2010). The remainder of the survey data, obtained with the LMIRCam[2] (Skrutskie et al. 2010; Leisenring et al. 2012), Clio2 (Sivanandam et al. 2006), and NICI[3] (Chun et al. 2008) instruments, will be presented in a companion paper. Subsets of the SEEDS survey (Janson et al. 2013) and the NICI survey (Wahhaj et al. 2013) focused on similar debris disk targets at H-band; however, we chose to image our sample with NaCo in the thermal infrared (L'-band). This method does not rely on methane absorption in the planet's atmosphere (as Spectral Differential Imaging does; Marois et al. 2000), nor is it negatively impacted by the reddening effect of thick clouds. The majority of planets found to date, despite their relatively cool effective temperatures, lack

---

[1]Nasmyth Adaptive Optics System (NAOS) Near-Infrared Imager and Spectrograph (CONICA)

[2]L/M-band mid-InfraRed Camera

[3]Near-Infrared Coronagraphic Imager

Target	Observation dates[a] UT (Hem 1, Hem 2)	Total integration time (s)	On-sky rotation (°)	Average DIMM seeing (")
HD 28355	2012 Nov 17, 2013 Jan 14	2580, 2060	24.80, 19.56	0.57, 0.78
HD 17848	2012 Nov 22, 2013 Jan 15	1940, 2860	19.37, 28.55	0.755, 0.89
HD 37484	2013 Jan 21, 2013 Jan 25	1360, 2232	27.86, 10.82	1.16, 0.6
HD 95086	2013 Apr 26, 2013 May 16	3800, 3120	24.85, 20.50	0.76, 1.4
HD 134888	2013 Apr 21, –	3800, –	93.04, –	1.22, –
HD 110058	2013 Apr 25, –	3250, –	33.53, –	1.425, –

Table 3.1 Observing Log for APP NaCo/VLT runs 090.C-0148(A) and 091.C-0457(A).

[a]Data are listed in chronological order from when the first hemisphere was observed. The last two targets were only observed in one APP hemisphere. Any difference in integration time between hemispheres was unintentional, simply due to the conditions of the night.

methane absorption and have thick clouds (eg: HR8799 bcd and 2MASS 1207 b Skemer et al. 2014).

The direct detection of close-in planets is limited by instrumental diffraction and scattering effects on the point spread function (PSF) of the bright primary star. The scattered light may be much brighter than a companion. Pupil apodizing coronagraphs block the primary star's light, suppressing its PSF at the expense of throughput ($\sim 40\%$ suppressed for the APP: Quanz et al. 2010). We use the APP coronagraph on NaCo at the VLT to increase our sensitivity around our stars.

This is the first paper in a series for the Holey Debris Disks project, discussing the VLT/NaCo APP coronagraphic data and results. In Section 6.2 we describe the APP observations and data reduction. In Section 3.3 we present the methods and data used for deriving the disk properties. In Section 6.3 we show the resulting contrast curves for each of our targets and discuss the significance of our sensitivity with respect to the disk properties derived from disk models. We conclude in Section 3.5.

3.2 APP Observations and Data Reduction

3.2.1 Observations

The APP data were obtained in 2012 and 2013 (090.C-0148(A) and 091.C-0457(A), PI: Tiffany Meshkat) at the VLT/UT4 with NaCo. The APP was used for additional diffraction suppression from $0\rlap{.}''2$ to $1\rlap{.}''0$, increasing the chance of detecting faint companions close to the target stars. The infrared wavefront sensor was used with the target stars themselves as the natural guide star. Data were acquired with the L27 camera (27 mas/pix) and the L'-band filter ($\lambda = 3.80\mu m$ and $\Delta\lambda = 0.62\mu m$). We used pupil tracking mode for Angular Differential Imaging (ADI; Marois et al. 2006) and intentionally saturated the stellar point-spread-function (PSF) core to

increase the signal-to-noise (S/N) from possible faint companions. We also obtained unsaturated data to calibrate the photometry relative to the central star and determine the sensitivity achieved in each dataset.

The APP suppresses diffraction over a 180° hemisphere on one side of the target star. Thus, two datasets need to be acquired, with different initial position angles (P.A.) for full coverage around the target star. We observed six targets with the APP (see Table 6.2), however only four of these have complete APP hemisphere coverage around all P.A.s. One of the targets (HD 134888) has 270° coverage with only one APP hemisphere (from 135° to -135°), the final target (HD 110058) does not have sufficient coverage for a detailed analysis.

Data were obtained in cube mode. Each data cube contains 200 frames, with an integration time between 0.1 s to 0.3 s per frame, depending on the L' mag of the star. Details about total integration time and field rotation per target are contained in Table 6.2. A three-point dither pattern (with an amplitude of 4") was used on the detector to subtract the sky background systematics from each dataset, detailed in Kenworthy et al. (2013).

3.2.2   Data Reduction

Data cubes closest in time at different dither positions were subtracted from each other and centroided. The average is taken over the subtracted cube in order to decrease the full dataset size. The final averaged frames cover a rectangular area of 3″1 by 1″5 centered on the star. The reason for this asymmetry is that the APP can only observe on the upper quartile portion of the CCD, due to the wedge, deliberately introduced in the optics to avoid ghost images (Kenworthy et al. 2010). Thus, we have complete coverage around the star out to 1″5 and incomplete coverage beyond that radius.

Optimized principal component analysis (PCA) was run on each target APP hemisphere independently, following Meshkat et al. (2014). PCA processed frames were derotated, averaged over, and combined with the other hemisphere to generate the final image with North facing up. If two regions of APP data overlap, those regions were combined by average. We generated final PCA processed frames for a range of principal components (PCs) from 3 up to 20. This first test was to determine if there were any companion candidates in our data, and if so, how robust they were to the number of PCs used in the image reduction.

We next fixed the number of PCs (approximately 10% of cubes in the dataset). We injected artificial planets in the data cubes and ran the extraction pipeline to generate contrast curves of point sources sensitivity for 5σ. The artificial planets were generated from the data with unsaturated PSF cores. The unsaturated data was scaled to the same exposure time as the saturated data. Since the APP is in the pupil plane, it affects the PSF of every source in the FOV in the same way, thus we can use the unsaturated star itself to generate artificial planets. The artificial planets were added to the data before PCA. The planets were added at different angular separations from 0″18 to 3″0 in steps of 0″15 and at different contrasts from 5 to 12 mag in steps of 1 mag. This was repeated for two different P.A.s, in order to place a fake planet in each APP hemisphere. We smoothed the final

PCA image by a 1 λ/D aperture (Bailey et al. 2013). We measured the S/N of the injected planet and decreased the flux of the injected planet until it reached a S/N of 5. The S/N was determined by dividing the flux in one pixel at the center of the injected planet by the noise in a 2 pixel wide ring around the star at the planet separation (not including the planet). We then interpolated between the contrasts to determine the 5σ contrast limit.

3.3 Debris Disk SEDs and Derivation of Disk properties

For the five stars that have complete or nearly complete APP coverage, we derive disk properties using both *Spitzer* and *Herschel* data with SED models and quote the results of HD 95086 from Su et al. (in press). We focus on the properties of the cold component, because it is the dominant part of the debris disk SED and is also more relevant to our direct imaging observations for low-mass companions because of the inner working angle in our images.

3.3.1 Spitzer and Herschel data reduction

Our targets were selected based on the presence of a bright, unresolved infrared excess indicative of a dusty debris disk. Most of them have well covered SEDs using *Spitzer* broad-band and spectroscopic data and *Herschel* broad-band photometry. We collected all the published broad-band photometry from the literature, and performed our own photometry measurements if the data were not published. *Spitzer* MIPS 24 and 70 μm photometry is part of the *Spitzer* Debris Disk Master Catalog (Su et al. in prep.), where data reduction and photometry extraction were briefly summarized in Sierchio et al. (2014). *Herschel* PACS data reduction and photometry extraction were performed following the procedure published by Balog et al. (2014) for calibration stars, except that, as detailed in the following section, smaller apertures were used for photometry measurements to minimize background contamination. All our debris disk targets have existing *Spitzer* IRS low-resolution spectra. We downloaded the extracted spectra using the CASSIS database (Lebouteiller et al. 2011). Three of the targets have MIPS-SED low-resolution spectra covering 55 to 95 μm with a slit width of ~20". We reduced and calibrated the MIPS-SED data as described by Lu et al. (2008).

3.3.2 Spitzer and Herschel fluxes

Herschel photometry of HD 95086 has been published by Moór et al. (2013) and Su et al. (in press). Here we briefly summarize the *Hershel* photometry results for HD 134888, HD 28355 and HD17848. The PACS 70 and 160 μm observation for HD 134888 was obtained under Program *OT1_dpadget_1*. The source appears to be point-like surrounded by background cirrus structure apparent on the 160 μm data, therefore we used an aperture size of 6" at 70 μm and 11" at 160 μm to measure the photometry. Including the absolute calibration errors (7%, Balog
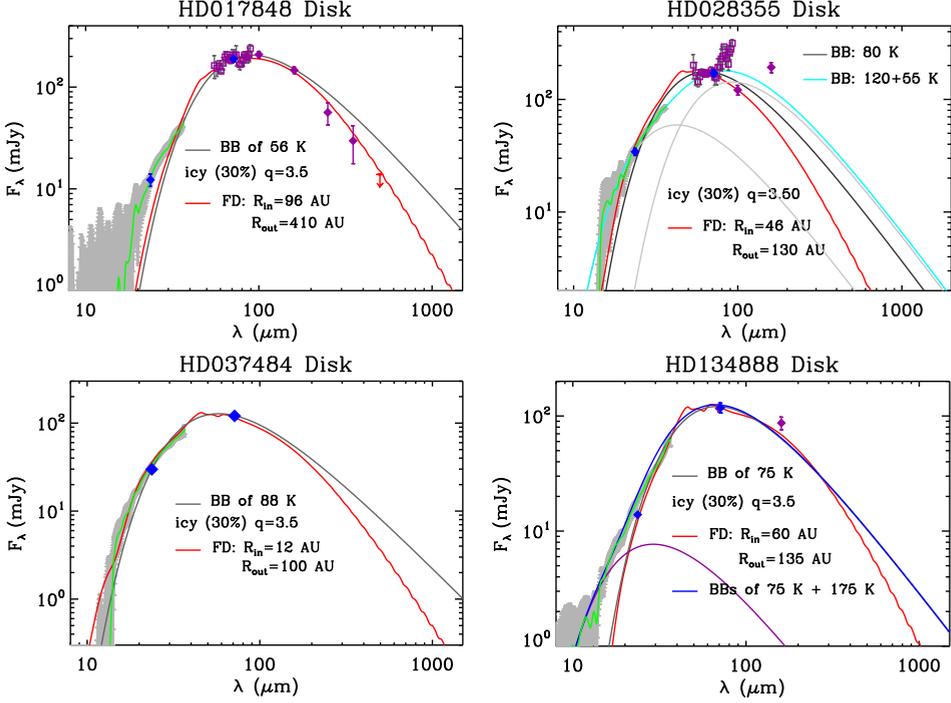
Figure 3.1 The SEDs of the four debris systems used to derive disk properties. For all the targets, the stellar photosphere has been subtracted. In all panels, the observed data are shown in various symbols and colors: blue diamonds: *Spitzer* MIPS 24 and 70 μm photometry; purple diamonds: *Herschel* PACS and SPIRE photometry; small green dots: *Spitzer* IRS spectrum; and purple squares: *Spitzer* MIPS-SED data. Various lines are SED fits: black solid lines for single blackbody emission, and red solid lines for the one-component icy grain SED model. For both the HD 28355 and HD 134888 disks, two blackbody temperature fit is also shown for comparison.

et al. 2014), the PACS photometry for HD 134888 is: 117±8.4 mJy and 87±11 mJy at 70 and 160 μm, respectively, and the PACS 70 μm photometry agrees with the MIPS 70 μm photometry (119±12 mJy) very well.

For HD 28355, PACS 100 and 160 μm data were obtained under Program *OT2_fmorales_3*. The source appears to be point-like, located near a bright source ~28" away. To avoid contamination from the nearby bright source which is extended at 160 μm, we used an aperture size of 6" to measure the photometry at both bands. Our adopted photometry for the HD 28355 system is 127±12 mJy and 195 mJy±20 mJy at 100 and 160 μm, respectively. The contamination from the nearby bright source explains the up-turn in the MIPS-SED data for wavelengths longward of ~70 μm (see Figure 3.1).

The PACS and SPIRE data for HD 17848 were obtained under program *OT1_pabraham_2*

using all the available photometry bands. The source appears to be elongated, suggesting a close to edge-on orientation to the disk. We used an aperture size of 22" to measure photometry at all three bands, at which radius the encircled flux reached the maximum and flattened afterwards. The final PACS fluxes are: 201±14 mJy, 213±15 mJy, and 148±11 mJy at 70, 100 and 160 μm, respectively. The PACS 70/100 μm photometry agrees well with the MIPS 70 μm and MIPS-SED data (see Figure 3.1). For the SPIRE data, we used the level 2 product for point sources provided by the *Herschel* Science Center (HIPE ver. 11). The source was detected at $\gtrsim 3 \sigma$ at both 250 and 350 μm, but not detected at 500 μm. The submillimeter fluxes are: 57±14 mJy, 30±12 mJy and <14 mJy (1σ) at 250, 350 and 500 μm, respectively. These values are consistent with the *Herschel* photometry recently published by Pawellek et al. (2014) within uncertainties.

The final disk SEDs were constructed by subtracting the best-fit Kurucz AT-LAS9 stellar atmosphere models (Castelli & Kurucz 2004) that fit the optical and near-infrared data. The uncertainties in the excess fluxes also included 2% photospheric extrapolation errors. Figure 3.1 shows the disk SEDs for our debris targets. We have excluded the disk SED for HD 95086, which will be published in Su et al. (in press), and for HD 110058, on which we did not obtain sufficient APP sky coverage for analysis.

3.3.3   Methodology of Deriving Disk Properties

To estimate the likely debris location, we performed basic SED modeling. We started with the simplest blackbody fitting for the disk SEDs (with a typical error of ±5 K) and used these temperatures to guide a more complicated SED model with adopted grain properties. Without spatial information, SED modeling is degenerate; therefore, our strategy is to minimize model parameters with some reasonable assumptions.

Similar to the SED model for HD 95086 (Su et al. in press), we adopted icy silicates as our grain properties. The particle size distribution was assumed to be a power-law form, $\sim a^{-q}$, where a is the grain radius with a minimum a_{min} and maximum a_{max} cutoffs. We adopted $q = 3.5$ for the power index of the particle distribution and $a_{max} = 1000$ μm for all the models. The minimum grain size is set to be close to the radiation blowout size estimated based on the grain density and stellar luminosity and mass. We assumed that the debris is uniformly distributed (constant surface density) from the inner radius (R_{in}) to the outer radius (R_{out}), and computed the thermal dust emission under optically thin conditions where the star is the only heating source. We then derived the best-fit inner and outer boundaries of the cold disk component, along with the total cold disk dust mass, quantifying the goodness of fit with reduced χ^2. As detailed in the following sections, we excluded any long wavelength data which was contaminated by nearby background galaxies, as well as any short wavelength data which might include a contribution from a warm disk component.

In some cases, weak warm excess shortward of $\sim 20\mu m$ was present. When the warm excess signal was greater than the uncertainty in photospheric subtraction, we also performed a blackbody fit to the short wavelength data to derive the warm

component's approximate temperature. Because the location of the tentative warm disks ($\lesssim 2$ to 10 AU) is less than the inner working angle of our high contrast observations, we do not perform detailed SED modeling for the warm excesses. We comment on the derived warm dust temperatures, but their nature will be discussed in a separate paper.

3.4   Results and Discussion

Target	Distance (pc)	L' (mag)	Age (Myr)	Cold disk temperature (K)	Cold disk inner/outer edge (AU)	Dust mass ($10^{-3} M_\oplus$)
HD17848	50.5±0.5	5.0	540	56	96^{+9}_{-37}, 410^{+24}_{-96}	1.3±0.7
HD28355	48.8±0.7	4.5	625	80	46±12, 130±30	1.8±0.7
HD37484	56.7±2.0	6.3	30	88	12^{+20}_{-4}, 100^{+100}_{-20}	2±1
HD95086	90.4±3.3	6.7	17	55	63±6, 189±13	200
HD134888	89.0±8.4	7.6	16	75	60±11, 135±29	32.5±14
HD110058	106.7±8.3	7.5	10	—	—	—

Table 3.2 Stellar and disk properties for targets.

The disk sizes (R_{in} and R_{out}) estimated from our simple SED modeling are only meant to provide a rough comparison between the expected disk location and the point-source detection contrast curves presented in Section 6.3. Some disks we modeled appear to have a very wide dust spatial distribution, and this is probably because we fit the SED with only one component. It is possible that such a cold disk SED (with a wide dust distribution) is composed of two different populations (warm/cold belts + disk halo) like the HD 95086 system (Su et al. in press). Furthermore, the SED from a typical debris disk, where the sizes of dust particles are in a steep power-law form, is dominated by small grains (less than a few times the blowout size) that are sensitive to non-gravitational forces. The fine debris distribution is expected to be broader than that of their parent bodies.

Three disks (HD 17848, HD 134888, and HD 28355) show signs of warm excesses in their disk SEDS (see Figure 3.1). In two cases (HD 17848 and HD 28355), the amount of warm excess is small and dominated by the errors from the photospheric subtraction. The temperatures of the tentative excesses for these two systems were reported in the literature. We report the blackbody fit for the warm component in the remaining system, HD 134888. As the focus of this survey was to search for companions sculpting the cold disk components, we only derived detailed parameters for the cold components.

We summarize the derived disk properties: cold disk inner and outer radii, and dust mass (grains up to 1 mm) in Table 5.1. In addition to the cold disk properties, Table 5.1 also lists the distance and L' mag for our sources (L' mag converted from the 2MASS survey Cutri et al. (2003) following Cox (2000)). The
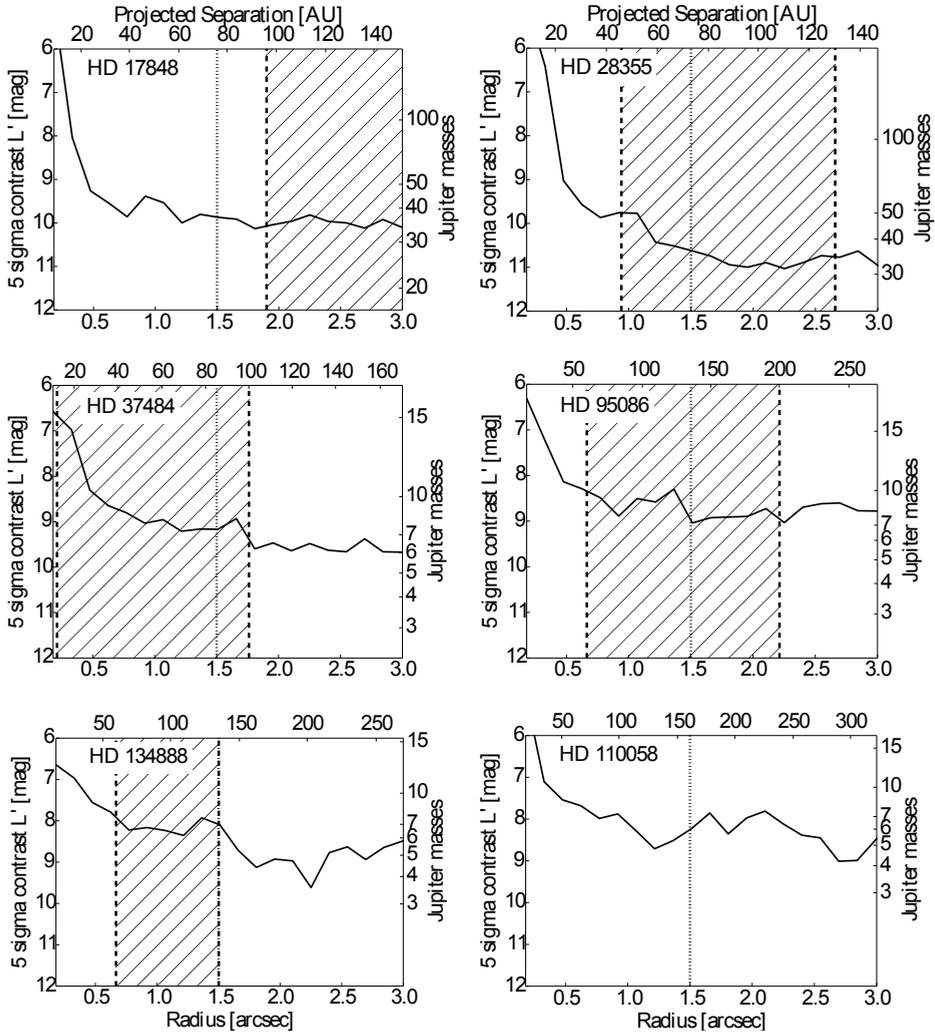
Figure 3.2 Sensitivity curves for the targets. Each target has the 5σ contrast curve in mag and Jupiter masses (based on the COND evolutionary tracks Baraffe et al. 2003) versus separation in arcseconds and AU. The vertical dotted line indicates the edge of the full FOV coverage ($1''.5$). The hashed region marks the mean value of the inner and outer edge of the cold disk based on our disk modeling. HD 134888 and HD 110058, have only one APP hemisphere coverage. HD 134888 has 270° coverage due to large sky rotation. The contrast axis (left) and radius in arcsec axis (bottom) is fixed relative to each figure for comparison.

disk properties for HD 110058 are not calculated due to the lack of sky coverage. The distances are extracted from the parallax (van Leeuwen 2007).

Figure 6.1 shows the resulting 5σ contrast curves for each of the targets. The dotted line is the edge of the full FOV coverage, beyond this line we have reduced coverage (see Figure 3.3). The hashed region is the mean value of the inner and outer edge of the cold debris belt, based on our SED modeling. For each target, we adopt the age of the system (discussion below) and convert the contrast limit to planet masses with the COND evolutionary models (Baraffe et al. 2003). On average we are sensitive to planetary mass companions ($\lesssim 13$ M_{Jup}) outward of $0\farcs5$ from the star, with the exception of HD 17848 and HD 28355 which are older than the other targets. HD 134888 and HD 110058 have only one APP hemisphere coverage. HD 134888 achieved 75% coverage (P.A.=135° to -135°, clock-wise passing through North) around the star due to large sky rotation. HD 110058 did not have large sky rotation (P.A.=100° to -90°, clock-wise passing through North), thus while the contrast curve is shown, we do not consider this target fully observed. Below we discuss each of the targets individually.

3.4.1   HD17848

HD 17848 (ν Hor) is an A2V (Houk & Cowley 1975) field star at distance $d = 50.5 \pm 0.5$ pc (adopting parallax $\varpi = 19.82 \pm 0.18$ mas from van Leeuwen 2007). We estimate the effective temperature to be $T_{\mathrm{eff}} = 8470 \pm 130$ K based on multiple photometric T_{eff} estimates: using UBVK$_s$ photometry with the color/T_{eff} table of Pecaut & Mamajek (2013), and the tight cluster of reported T_{eff} estimates in the literature (Allende Prieto & Lambert 1999; Paunzen et al. 2006; Rhee et al. 2007; Patel et al. 2014). Our adopted T_{eff} is systematically cooler than that reported by Chen et al. (2014) (9000 K), which is an outlier compared to the other estimates. Adopting the V magnitude from Mermilliod (1994) (V = 5.254 ± 0.005), van Leeuwen (2007) parallax, and adopted T_{eff}-appropriate bolometric correction BC$_V$ = -0.040 ± 0.034 (Pecaut & Mamajek 2013), we estimate ν Hor's luminosity to be $\log(L/L_\odot) = 1.222 \pm 0.016$ dex. Based on our HR diagram position for ν Hor, we use the evolutionary tracks of Bertelli et al. (2009) to infer an isochronal age of ~540 Myr and mass 1.90 $M_\odot$. Sampling a reasonable range of protostellar chemical compositions (Y = 0.26-0.27, Z = 0.014-0.017), we estimate isochronal age 1σ uncertainties of ±90 Myr (statistical) and ±60 Myr (systematic), and mass 1σ uncertainties of ±0.02 $M_\odot$ (statistical) and ±0.04 $M_\odot$ (systematic). Hence, we do not find support for the young age of ~100 Myr proposed by Rhee et al. (2007), and estimate ν Hor to be ~5× older than previously thought.

Its IRS spectrum was first analyzed by Ballering et al. (2013), and suggested the system is a two-component disk with dust temperatures of 164 K and 50 K. However, Chen et al. (2014) suggested a much warmer temperature, 353^{+4}_{-8} K, while the cold temperature (57±5 K) was consistent with the early result. The discrepancy is most likely due to how the excess flux in the mid-infrared range was determined (especially how the different modules of IRS spectra joined and pinned down to the photosphere). Therefore, the nature and amount of warm excess is still in debate. Using the observed dust temperature as gauges, the warm excess
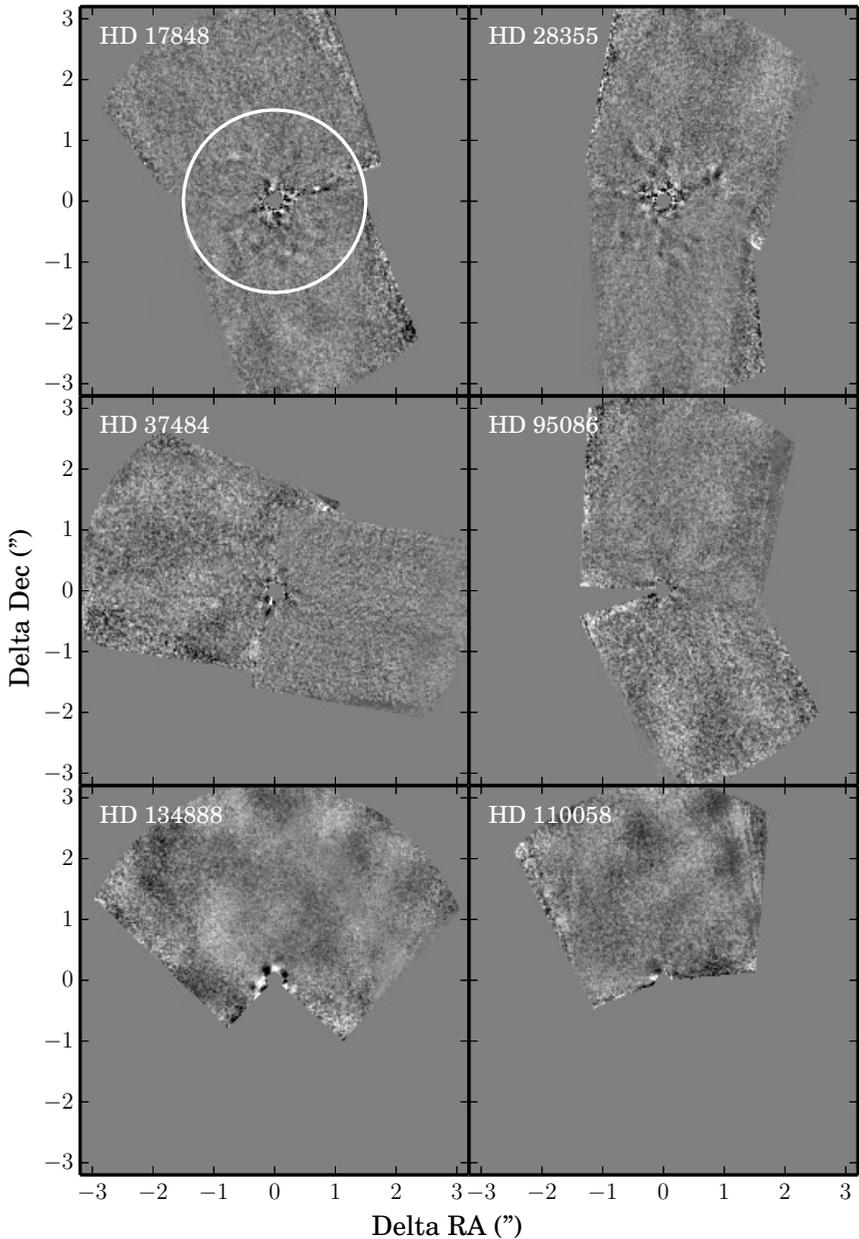
Figure 3.3 Final PCA reduced images of all six of our targets generated with optimized PCA. The full sensitivity FOV is indicated by the white circle in HD 17848 at 1″.5. Beyond 1″.5 we do not have full coverage because we only observe on the upper quartile portion of the CCD. The color range in each of the images is limited to $\pm 5\sigma$. The point source around HD 17848 is an artifact.

characterized by Ballering et al. (2013) would be asteroid-like with orbital distances of 9–12 AU, while the value from Chen et al. (2014) would be terrestrial-like with orbital distances of 2–3 AU. The new far-infrared photometry from *Herschel* and the MIPS-SED data confirm that the cold disk has a typical dust temperature of ~56 K (see Figure 3.1). We excluded data points shortward of ~30 μm in our SED model, resulting in an inner cold disk radius of 96^{+9}_{-37} AU and an outer cold radius of 410^{+24}_{-96} AU with a total dust mass of $(1.3\pm0.7)\times10^{-3}M_\oplus$.

No bright point sources were detected around HD 17848 (see Figure 3.3). The overlapping region between two APP hemispheres is noisy due to the edge of the dark APP hole. Therefore, the bright point (at $0\rlap{.}''7$ and P.A.=-74°) on the reduced image is probably a noise spike. We compared any possible faint point sources in our data with archival data obtained with NaCo/VLT from both 2011 (087.C-0142(A)) and 2009 (084.C-0396(A)) and verified that none of these faint point sources are present in all three datasets.

Based on the disk structure, we would expect to find companions inside $1\rlap{.}''9$ if the inner edge of the cold disk is maintained by unseen planet(s). Our high-contrast observations rule out the presence of a low-mass star down to the brown dwarf regime in the range of $0\rlap{.}''5$ –3"(~25–150 AU). Bear in mind, as shown in Figure 3.3, beyond $1\rlap{.}''5$ we do not have complete sky coverage around the star. As mentioned in Section 3.3.1, the HD 17848 disk may be an edge-on. This limits our ability to detect companions unless they are fortuitously at a projected separation outwards of $0\rlap{.}''5$.

3.4.2 HD 28355

HD 28355 is an A7V (Abt & Morrell 1995) member of the 650 Myr-old Hyades cluster (Su et al. 2006; De Gennaro et al. 2009) at a distance of 48.8 ± 0.6 pc away (van Leeuwen 2007). Its IRS spectrum along with MIPS 70 μm photometry has been published by several papers with different derived dust temperatures. Morales et al. (2011) suggest the disk SED is best described by two temperatures of 128 K and 60 K, which are consistent with the values (120 K + 54 K) published by Ballering et al. (2013) within errors. Analysis performed by Chen et al. (2014) gives the warm temperature of 176^{+7}_{-8} K and the cold temperature of 69^{+5}_{-6} K. As discussed in Section 3.3, HD 28355 is near a bright infrared source, which is extended at 160 μm, as a result its far-infrared fluxes are contaminated. The overall disk SED can be fit with two temperatures: ~120 K and ~55 K (see Figure 3.1). However, the contamination-free part of the SED (data shortward of ~80 μm) can also be described by one single temperature of ~80 K (within a few σ). Therefore, we excluded the *Herschel* 160 μm data and the MIPS-SED points longward of 85 μm in our one-component SED model. The inner boundary is estimated to be 46±12 AU, and the outer is 130±30 AU with a total dust mass of $(1.8\pm0.7)\times10^{-3}M_\oplus$.

No bright point sources were detected around HD 28355 (see Figure 3.3). The structure inwards of $1\rlap{.}''5$ is due to residuals from the APP PSF. We were not sensitive to planetary mass companions due to the older age of the star. We were able to rule out substellar companions from $0\rlap{.}''5$ –3"(~24–147 AU). Our single component SED model places the inner boundary of the disk at $0\rlap{.}''9$. Thus, if the

cold disk is shaped by a companion, it must be less than ~50 $M_{\rm Jup}$.

3.4.3   HD 37484

HD 37484 is a F3V (Houk 1982) star at a distance of $d = 56.8 \pm 2.0$ pc (adopting parallax $\varpi = 17.61 \pm 0.62$ mas from van Leeuwen 2007). Its $B - V$ vs. M_V position places it on the zero age main sequence (ZAMS), thus it must be >27 Myr in order to allow enough time for a ~1.36 $M_\odot$ star to reach the main sequence. Its position is commensurate with that of the Pleiades and IC2391 clusters, making it < 100 Myr. It has a brighter and hotter (~A5V) common proper motion companion 0.34 deg away (HR 1915). Both stars are considered Columba members by Malo et al. (2013), who list 10-40 Myr for the group. The companion appears to be on or below the ZAMS, consistent with an age of >19 Myr. HD 37484's HR diagram position is consistent with the previous assigned age of ~30 Myr. Given its Columba membership and consistency with the age of other Columba members, we adopt the age of 30 ± 10 Myr.

The disk SED is composed of data from *Spitzer* MIPS 24 and 70 *µm* photometry as well as IRS 10–35 *µm* spectroscopy. The disk SED is best fit with a blackbody temperature of ~88 K. The best fitting disk model has an inner radius of 12^{+20}_{-4} AU, outer radius of 100^{+100}_{-20} AU and dust mass of $(2\pm1)\times10^{-3}$ $M_\oplus$. This source does not have longer wavelength *Herschel* data, which makes the outer disk radius and dust mass fairly unconstrained.

We initially detected a faint point source around HD 37484 at 0″.97 (55 AU from the star), 9.0 magnitudes fainter than the host star at a P.A. of 103° in our APP data (see Figure 3.3). However, this point source was not detected in archival data with equivalent sensitivity taken in 2011 (088.C-0085(A)), allowing us to conclude that it is unlikely to be a real source. This false detection demonstrates the importance of archival data, which can be used to quickly confirm or deny the physical nature of a point source.

3.4.4   HD 95086

HD 95086 is a 17 Myr old A8 LCC member star at a distance of 90.4 ± 3.3 pc (Meshkat et al. 2013). The system was also resolved by *Herschel* at 70 and 100 *µ*m (Moór et al. 2013) with an estimated inclination of 25° from face-on. Re-analysis of the *Herschel* resolved images combined with detailed SED modeling reveal that the extended part of the images arises from a disk halo (Su et al. in press), similar to the disk halo found around HR 8799 (Su et al. 2009; Matthews et al. 2014). In the three-component disk model presented by Su et al. (in press), the inner belt is located from ~7 AU to ~10 AU, and the cold planetesimal disk likely ranges from 63±6 AU to 189±13 AU, and are surrounded by an extended halo up to ~800 AU.

A 5 $M_{\rm Jup}$ planet was discovered around HD 95086 by Rameau et al. (2013b). Our *H*-band NICI/Gemini non-detection provided a strict color lower limit for the planet of $H - L' > 3.1 \pm 0.5$ mag (Meshkat et al. 2013). The subsequent *H*-band Gemini Planet Imager (GPI) detection of HD 95086 b by (Galicher et al. 2014)

provides a red planet color of $H - L' = 3.6 \pm 1.0$. We also observed the system with the APP, but did not detect it due to decreased AO quality at high airmass (> 1.4) during the observation (APP hemisphere 2, see Figure 3.3). Due to lack of sky rotation, we are missing about 20° of coverage. Figure 6.1 shows that we achieve a sensitivity of ~10 $M_{\rm Jup}$ at the separation of the planet, however the detected planet is 5 ± 2 $M_{\rm Jup}$ (Rameau et al. 2013c).

3.4.5   HD 134888

HD 134888 is an F4V star, located 90^{+9}_{-8} pc away (adopting parallax $\varpi = 11.12 \pm 1.05$ mas from van Leeuwen 2007). We adopt an age of 16 Myr based on its membership in the Lower Centaurus-Crux (LCC) association, commensurate with isochronal age estimates for the star (16-25 Myr; Pecaut et al. 2012). Chen et al. (2014) conclude it has a two-component disk with the warm temperature of 387^{+6}_{-7} K and the cold temperature of 72 ± 5 K. The far-IR excesses along with the IRS excess longward of ~30 μm are consistent with a blackbody temperature of 75 K (see Figure 3.1). However, we found the warm excess is better fit with a dust temperature of ~175 K (i.e., asteroid-like). The derived temperature in the warm component is highly dependent on the amount and shape of the excess emission in the 10–20 μm region. Future mid-IR observations are needed to better characterize the warm component. We excluded data points shortward of ~30 μm in our SED fitting of the cold component. The best-fit one cold-component disk ranges from 60 ± 11 AU to 135 ± 29 AU with a dust mass of $3.25 \pm 1.4 \times 10^{-2}$ $M_\oplus$.

Based on our inferred disk structure, the ideal place for detecting the potential low-mass companion that sculpts the disk is interior of 60 AU ($0.''66$) or exterior of 135 AU ($1.''5$). A possible interesting point source appeared at $0.''2$ from the star, but after comparing with archival data (087.C-0142(A)), the point source appears to be an artifact of the data reduction. No believable point sources are detected in our reduced images around the star at any projected separation, however we cannot conclusively say there are no companions around HD 134888. From a P.A. of 135° to -135° (clock-wise, passing through North, see Figure 3.3), we do not detect any companions with an average mass limit of 5-7 $M_{\rm Jup}$.

3.4.6   HD 110058

HD 110058 is a A0V star (Houk 1978) and member of the LCC subgroup of Sco-Cen (de Zeeuw et al. 1999; Rizzuto et al. 2011). The revised Hipparcos parallax from van Leeuwen (2007) ($\varpi = 9.31 \pm 0.78$ mas) translates to a distance of 107^{+10}_{-8} pc. The star is situated near ℓ, $b = 301°$, $+13°.6$, in the northern part of LCC, which appears to be the oldest part of the subgroup (Preibisch & Mamajek 2008; Pecaut et al. 2012), so we follow Chen et al. (2014) and adopt an age of 17 Myr.

We did not achieve full 360° APP coverage around this star . Only one APP hemisphere was observed and it had poor sky rotation. Without full sky coverage, the contrast curve for HD 110058 (Figure 6.1) is only valid from a P.A. of ~ 100° to -90° (clock-wise, passing through North, see Figure 3.3). We are sensitive to 5–8 $M_{\rm Jup}$ from $0.''5$ –3". We detect no point sources in this limited region around

the star.

3.5   Conclusions

We present the first results from our survey searching for planets around stars with bright debris disks with gaps. In this paper, we present the data from six targets obtained with the APP coronagraph on NaCo/VLT. One of our targets, HD 95086, was found to harbor a planet on the inner edge of the outer debris belt (Rameau et al. 2013b; Moór et al. 2013; Galicher et al. 2014). While our data were not sensitive enough to detect this planet (Meshkat et al. 2013), its discovery demonstrates the strength of two-component disk targets.

For each of the targets, we derive disk properties based on our SED models. These properties (including disk mass and debris radial distribution) allow us to infer the likely location of gaps in the disk, which may be carved out by planets. We detect no companions in our APP data. A few plausible point sources were detected but ruled out after comparison with archival data. We were sensitive to planetary-mass companions for four of the six targets, using COND atmosphere models. If cool planets have substantial methane absorption and little cloud opacity, as is predicted by the COND evolutionary models (Baraffe et al. 2003), then L'-band will be less sensitive to planets. However, the majority of directly imaged planets do not behave like field brown dwarfs of similar effective temperature. Most cool planets do not show evidence of methane absorption (eg: HR8799bcd and 2M1207b Skemer et al. 2014) and are redder than predicted ($H - L' = 2$ to 3 mag: Galicher et al. 2014) Thus, our use of L'-band is comparable to the best H-band surveys at separations where we are contrast limited. The benefit of the APP for companion discovery over direct imaging is inconclusive, based on our sample of six observations. See Meshkat et al. (in prep.) for further discussion.

The sample size of six targets is too small to draw conclusions about the origins of the gaps in Holey Debris Disks. Our complete Holey Debris Disks sample (Bailey et al. in prep.) will allow stronger statements of whether the gaps in these disks are formed by one massive companion, multiple low-mass companions, or other mechanisms. We discuss each target individually and analyze the sensitivity of companions achieved relative to the boundaries of the debris disks, based on our disk models.

In order to detect lower mass planets at the inner edges of the cold outer debris belts, greater sensitivity needs to be achieved. In this paper, we have only modelled the outer single cold component, however many of our targets may be two-component disks. The projected separation of the warm inner disk components are much less than the inner working angle limit of current high-contrast imaging data, and so planets sculpting the warm disks would remain undetected. Discoveries like that of the low-mass planet HD 95086 b strengthen the notion that gaps need not be carved by a single very massive companions (Dodson-Robinson & Salyk 2011), and thus future surveys will require increased sensitivity in addition to smaller inner working angle.

Acknowledgements

References

Abt, H. A., & Morrell, N. I. 1995, ApJS, 99, 135

Allende Prieto, C., & Lambert, D. L. 1999, A&A, 352, 555

Bailey, V., Hinz, P. M., Currie, T., et al. 2013, ApJ, 767, 31

Ballering, N. P., Rieke, G. H., Su, K. Y. L., & Montiel, E. 2013, ApJ, 775, 55

Balog, Z., Müller, T., Nielbock, M., et al. 2014, Experimental Astronomy, 37, 129

Baraffe, I., Chabrier, G., Barman, T. S., Allard, F., & Hauschildt, P. H. 2003, A&A, 402, 701

Bertelli, G., Nasi, E., Girardi, L., & Marigo, P. 2009, A&A, 508, 355

Biller, B. A., Liu, M. C., Wahhaj, Z., et al. 2013, ApJ, 777, 160

Biller, B. A., Males, J., Rodigas, T., et al. 2014, ArXiv e-prints

Brandt, T. D., McElwain, M. W., Turner, E. L., et al. 2014, ArXiv e-prints

Castelli, F., & Kurucz, R. L. 2004, ArXiv Astrophysics e-prints

Chauvin, G., Vigan, A., Bonnefoy, M., et al. 2014, ArXiv e-prints

Chen, C. H., Mittal, T., Kuchner, M., et al. 2014, ApJS, 211, 25

Chun, M., Toomey, D., Wahhaj, Z., et al. 2008, in Society of Photo-Optical Instrumentation Engineers (SPIE) Conference Series, Vol. 7015, Society of Photo-Optical Instrumentation Engineers (SPIE) Conference Series, 1

Cox, A. N. 2000, Allen's astrophysical quantities

Cutri, R. M., Skrutskie, M. F., van Dyk, S., et al. 2003, VizieR Online Data Catalog, 2246, 0

De Gennaro, S., von Hippel, T., Jefferys, W. H., et al. 2009, ApJ, 696, 12

de Zeeuw, P. T., Hoogerwerf, R., de Bruijne, J. H. J., Brown, A. G. A., & Blaauw, A. 1999, AJ, 117, 354

Desidera, S., Covino, E., Messina, S., et al. 2014, ArXiv e-prints

Dodson-Robinson, S. E., & Salyk, C. 2011, ApJ, 738, 131

Galicher, R., Rameau, J., Bonnefoy, M., et al. 2014, A&A, 565, L4

Houk, N. 1978, Michigan catalogue of two-dimensional spectral types for the HD stars

—. 1982, Michigan Catalogue of Two-dimensional Spectral Types for the HD stars. Volume_3. Declinations -40_0 to -26_0.

Houk, N., & Cowley, A. P. 1975, University of Michigan Catalogue of two-dimensional spectral types for the HD stars.

Janson, M., Brandt, T. D., Moro-Martín, A., et al. 2013, ApJ, 773, 73

Kenworthy, M., Quanz, S., Meyer, M., et al. 2010, The Messenger, 141, 2

Kenworthy, M. A., Meshkat, T., Quanz, S. P., et al. 2013, ApJ, 764, 7

Kuzuhara, M., Tamura, M., Kudo, T., et al. 2013, ApJ, 774, 11

Lafrenière, D., Doyon, R., Marois, C., et al. 2007, ApJ, 670, 1367

Lebouteiller, V., Barry, D. J., Spoon, H. W. W., et al. 2011, ApJS, 196, 8

Leisenring, J. M., Skrutskie, M. F., Hinz, P. M., et al. 2012, in Society of Photo-Optical Instrumentation Engineers (SPIE) Conference Series, Vol. 8446, Society of Photo-Optical Instrumentation Engineers (SPIE) Conference Series, 4

Lenzen, R., Hartung, M., Brandner, W., et al. 2003, in Society of Photo-Optical Instrumentation Engineers (SPIE) Conference Series, Vol. 4841, Society of Photo-Optical Instrumentation Engineers (SPIE) Conference Series, ed. M. Iye

& A. F. M. Moorwood, 944–952

Lu, N., Smith, P. S., Engelbracht, C. W., et al. 2008, PASP, 120, 328

Malo, L., Doyon, R., Lafrenière, D., et al. 2013, ApJ, 762, 88

Marois, C., Doyon, R., Racine, R. & Nadeau, D. 2000, PASP, 112, 91

Marois, C., Lafrenière, D., Doyon, R., Macintosh, B., & Nadeau, D. 2006, ApJ, 641, 556

Marois, C., Macintosh, B., Barman, T., et al. 2008, Science, 322, 1348

Marois, C., Macintosh, B., & Véran, J.-P. 2010, in Society of Photo-Optical Instrumentation Engineers (SPIE) Conference Series, Vol. 7736, Society of Photo-Optical Instrumentation Engineers (SPIE) Conference Series

Matthews, B., Kennedy, G., Sibthorpe, B., et al. 2014, ApJ, 780, 97

Mermilliod, J.-C. 1994, Bulletin d'Information du Centre de Donnees Stellaires, 45, 3

Meshkat, T., Kenworthy, M. A., Quanz, S. P., & Amara, A. 2014, ApJ, 780, 17

Meshkat, T., Bailey, V., Rameau, J., et al. 2013, ApJL, 775, L40

Moór, A., Ábrahám, P., Kóspál, Á., et al. 2013, ApJL, 775, L51

Morales, F. Y., Rieke, G. H., Werner, M. W., et al. 2011, ApJL, 730, L29

Nielsen, E. L., Liu, M. C., Wahhaj, Z., et al. 2013, ApJ, 776, 4

Patel, R. I., Metchev, S. A., & Heinze, A. 2014, ApJS, 212, 10

Paunzen, E., Schnell, A., & Maitzen, H. M. 2006, A&A, 458, 293

Pawellek, N., Krivov, A. V., Marshall, J. P., et al. 2014, ArXiv e-prints

Pecaut, M. J., & Mamajek, E. E. 2013, ApJS, 208, 9

Pecaut, M. J., Mamajek, E. E., & Bubar, E. J. 2012, ApJ, 746, 154

Preibisch, T., & Mamajek, E. 2008, The Nearest OB Association: Scorpius-Centaurus (Sco OB2), ed. B. Reipurth, 235

Quanz, S. P., Meyer, M. R., Kenworthy, M. A., et al. 2010, ApJL, 722, L49

Quillen, A. C. 2006, MNRAS, 372, L14

Quillen, A. C., & Thorndike, S. 2002, ApJL, 578, L149

Rameau, J., Chauvin, G., Lagrange, A.-M., et al. 2013a, ApJL, 779, L26

—. 2013b, ApJL, 772, L15

Reggiani, M., Quanz, S. P., Meyer, M. R., et al. 2014, ArXiv e-prints

Rhee, J. H., Song, I., Zuckerman, B., & McElwain, M. 2007, ApJ, 660, 1556

Rizzuto, A. C., Ireland, M. J., & Robertson, J. G. 2011, MNRAS, 416, 3108

Rousset, G., Lacombe, F., Puget, P., et al. 2003, in Society of Photo-Optical Instrumentation Engineers (SPIE) Conference Series, Vol. 4839, Society of Photo-Optical Instrumentation Engineers (SPIE) Conference Series, ed. P. L. Wizinowich & D. Bonaccini, 140–149

Sierchio, J. M., Rieke, G. H., Su, K. Y. L., & Gáspár, A. 2014, ApJ, 785, 33

Sivanandam, S., Hinz, P. M., Heinze, A. N., Freed, M., & Breuninger, A. H. 2006, in Society of Photo-Optical Instrumentation Engineers (SPIE) Conference Series, Vol. 6269, Society of Photo-Optical Instrumentation Engineers (SPIE) Conference Series, 0

Skemer, A. J., Marley, M. S., Hinz, P. M., et al. 2014, ApJ, 792, 17

Skrutskie, M. F., Jones, T., Hinz, P., et al. 2010, in Society of Photo-Optical Instrumentation Engineers (SPIE) Conference Series, Vol. 7735, Society of Photo-Optical Instrumentation Engineers (SPIE) Conference Series, 3

Su, K. Y. L., & Rieke, G. H. 2014, in IAU Symposium, Vol. 299, IAU Symposium, ed. M. Booth, B. C. Matthews, & J. R. Graham, 318–321

Su, K. Y. L., Rieke, G. H., Stansberry, J. A., et al. 2006, ApJ, 653, 675

Su, K. Y. L., Rieke, G. H., Stapelfeldt, K. R., et al. 2009, ApJ, 705, 314

van Leeuwen, F. 2007, A&A, 474, 653

Vigan, A., Patience, J., Marois, C., et al. 2012, A&A, 544, A9

Wahhaj, Z., Liu, M. C., Nielsen, E. L., et al. 2013, ApJ, 773, 179

Chapter 4

FURTHER EVIDENCE OF THE PLANETARY NATURE OF HD 95086 B FROM GEMINI/NICI H-BAND DATA

We present our analysis of the Gemini/NICI H-band data of HD 95086, following the discovery of the planet HD 95086 b in L'. The H-band data reach a contrast of 12.7 mag relative to the host star at 5σ levels in the location of HD 95086 b, and no point source is found. Our non-detection and $H - L'$ color limit rules out the possibility that the object is a foreground L/T dwarf and that, if it is bound to HD95086, it is a genuine planetary mass object. We estimate a new pre-main-sequence isochronal age for HD 95086 of 17±4 Myr, which is commensurate with previous mean age estimates for the Lower Cen-Crux subgroup. Adopting an age of 17 Myr, the color limit is inconsistent with the COND model, marginally consistent with the BT-SETTL model, and consistent with the DUSTY model.

T. Meshkat, V. Bailey, J. Rameau, M. Bonnefoy, A. Boccaletti, E. E. Mamajek, M. Kenworthy, G. Chauvin, A.-M. Lagrange, K. Y. L. Su, and T. Currie

4.1 Introduction

Rameau et al. (2013b) reported the probable detection of a 4 to 5 Jupiter mass companion to HD 95086 lying at a projected separation of 56 AU. The host is a young (17±4 Myr; see Section 4.4.1) A8 type star. The large infrared excess (Chen et al. 2012) suggests that the star is harboring a debris disk, as yet unresolved.

The discovery at the *L'* band (3.8 μm), using the angular differential imaging technique (ADI; Marois et al. 2006), was a 9σ detection in the first epoch. The second epoch suffered from poor observing conditions, resulting in a 3σ re-detection of the planet. The astrometric precision allowed for the rejection of a background object with nearly 3σ probability. Rameau et al. (2013b) also carried out *Ks* (2.18 μm) observations that also suffered from bad observing conditions. This resulted in low *Ks* sensitivity and a non-detection. These observations were used to conclude that the detection at *L'* was likely inconsistent with a background star. Such a non-detection rejected the background hypothesis and suggested a red object with *Ks-L'*>1.2 mag.

With a predicted temperature of $T_{\text{eff}} \simeq 1000$ K (compared to the 1600–1700 K of β Pic b, and 800–1100 K for HR8799 bcde; Bonnefoy et al. 2013; Currie et al. 2011; Skemer et al. 2012), a giant planet will have an atmosphere close to the L-T spectral transition, where the effect of reduced surface gravity (characteristic of young and low-mass companions) is expected to dramatically affect the balance between dust formation and settling in the atmosphere (Stephens et al. 2009). If the companion is real, it would be a benchmark for spectroscopic studies of low-mass giant planets since it would be one of the lightest directly imaged planets, [1] and key to testing predictions about dust settling in low-gravity atmospheres. The methane bands seen in mature brown-dwarfs at a similar temperature as HD 95086 b might also be reduced (or lacking) due to the effect of reduced surface gravity, which in turn triggers non-equilibrium chemistry of CO/CH_4 (Hubeny & Burrows 2007).

Low-resolution spectroscopy is highly challenging with the present instrumentation given the contrast and faintness of HD 95086 b (Vigan et al. 2012). Broad band photometry is currently the only way to derive the color of the companion and constrain its atmospheric properties. We examine our *H*-band NICI data[2] taken in 2012, the same epoch as the *L'* discovery image. We do not detect the companion in our *H*-band data, allowing us to derive a lower limit to the *H-L'* color and reject a foreground contamination hypothesis.

In Sections 6.2 and 4.3, we describe our observations and our derived upper *H*-band limit. In Section 4.4, we discuss the age as determined by isochrone fitting and we show that the very red color rejects the foreground contamination hypothesis.

---

[1]HR8799 b (Marois et al. 2008) might be as light as HD 95086 b but its low mass estimate was derived from dynamical instability rather than from atmospheric models which give higher mass, and Fomalhaut b might be a dwarf planet and only the reflecting dust is detected (Kalas et al. 2008; Currie et al. 2012).

[2]Taken as part of a survey of young stars with debris disks (PI: V. Bailey).

Date (UT)	2012 Mar 19	2012 Mar 26	2012 Mar 30
Total integration time (s)	2695	3520	3520
Frames observed	49	64	64
Frames rejected	5	4	4
On-sky rotation (°)	18.24	25.13	25.19
Parallactic angle (°)	18.89/37.13	342.14/07.27	347.71/12.90
DIM seeing (")	0.6	0.6	0.6

Table 4.1 Observing Log for NICI H-band 2012 Data

4.2 Observations

4.2.1 Data

Observations of HD 95086 were taken on UT 2012 March 19, 26, and 30 using the NICI camera (Toomey & Ftaclas 2003) on Gemini South in the H-filter ($\lambda = 1.65\mu$m and $\Delta\lambda = 0.29\mu$m) as part of a survey looking for gas giant planets around young stars with IR excesses (PI: V. Bailey). The camera was configured with the broad H-band filter and the $0\rlap{.}''32$ coronagraphic mask. The integration times for individual science frames are 55.0 s (5 coadded readouts of 11.0 s each). The details of the observing log for these data is listed in Table 1. Five percent of the frames are rejected per night due to poor alignment of the central star under the mask. The instrument was configured in telescope pupil tracking mode to keep the point spread function (PSF) structure from the telescope optics fixed with respect to the orientation of the detector. As a consequence, the position angle (PA) of the sky on the detector underwent rotation of 19°, 25°, and 25° on each of the nights, respectively.

4.2.2 NICI Data Reduction

Calibration data consists of dark frames with the same integration time and flats from the nights of March 19 and 26. The flat field images were dark-subtracted, and all individual flat field images were normalized by their median and combined together with a clipped mean to form a final normalized flat field image.

The dark frames were subtracted from the science frames and then the dark-subtracted science frames were divided by the normalized flat field frame. A bad pixel mask was constructed from pixels in the flat field frame that were greater than 1.2 or less than 0.8 in value. These bad pixels were interpolated over using adjacent good values in the science frames. Hot, cold, and flaky pixels were found and interpolated over in individual science frames by their values being more than 1000 counts different from the median of a 3×3 box centered on that pixel. Finally, the NICI distortion correction was applied to the images in order to perform astrometry on the additional background sources in the field of view.

4.2.3 Photometric Calibration

Due to the radial transmission function of the apodizer (Wahhaj et al. 2011) and the level of adaptive optics (AO) correction on the central star, photometric calib-

ration was performed using a background star visible 4″5 away from the primary star in the images. It was first detected by Kouwenhoven et al. (2005) and confirmed as a background object by Rameau et al. (2013b). This background star was used as a photometric reference to determine the flux calibration and sensitivity in our *H*-band data. The NICI coronagraphic transmission curve is not yet published, thus to determine the near-infrared photometry of the background star, we utilize archival photometry from *Hubble Space Telescope* (*HST*) NICMOS data taken in 2007 (program 11157, PI: Joseph Rhee). The calibrated mosaic files provided by the *HST* archive are background-subtracted and normalized by exposure time. Two images, one per roll angle, are taken in each F110W and F160W; each of the four images has a total exposure time of 895 s. We roll-subtracted each pair of images, and used the aperture diameter and corresponding aperture correction recommended by the NICMOS data reduction handbook for NIC2. We derived the magnitudes in F110W and F160W of 13.63 ± 0.05 and 12.81 ± 0.05 for the background star. We used the transformations of Stephens et al. (2000) to derive *J* and *H* magnitudes of 13.25 ± 0.10 and 12.81 ± 0.10, respectively.

4.3 Image Processing

The data were centroided in a smaller frame which ensured the background visual binary star is clearly visible at an angular separation of 4″5 and a PA of 330°. The unsaturated visual binary star is crucial for photometry, as the host star was blocked by the coronagraph, and the transmission of the light from the star is not well constrained. Kouwenhoven et al. (2005) estimated this star to have a *Ks* magnitude of 12.67 mag. Rameau et al. (2013b) found the background star to have a $Ks - L'$ color of -0.3 ± 0.2 mag. Using our NICMOS-derived *H*-band magnitude of the background star, we estimate a $H - Ks$ color of 0.14 ± 0.10 mag for the background star.

To understand the impact of imaging processing on the detectability of faint sources, we processed the data with artificially added planets with three independent pipelines: one by Meshkat et al. (2013) based on principal component analysis (PCA; Amara & Quanz 2012), one by Boccaletti et al. (2013) using locally optimized combination of images (LOCI; Lafrenière et al. 2007), and one by Chauvin et al. (2012) using ADI. The three pipelines agree with each other, and here we only show the results using PCA.

The PCA pipeline was run separately for the data from each night, with an inner radius of 0″50 corresponding to the edge of the coronagraphic mask. For each dataset, five principal components were used to create a model of the stellar coronagraphic image. This optimal number of principal components was determined by injecting artificial components at the same angular separation with a different PA from the expected planet. The final de-rotated datacubes from each night are averaged for a final image.

Figure 4.1 shows the PCA reduced image in the upper left corner. No point sources are seen at the expected position (see the white circle in Figure 4.1). The other images are with an artificial planet injected with the contrast and angular
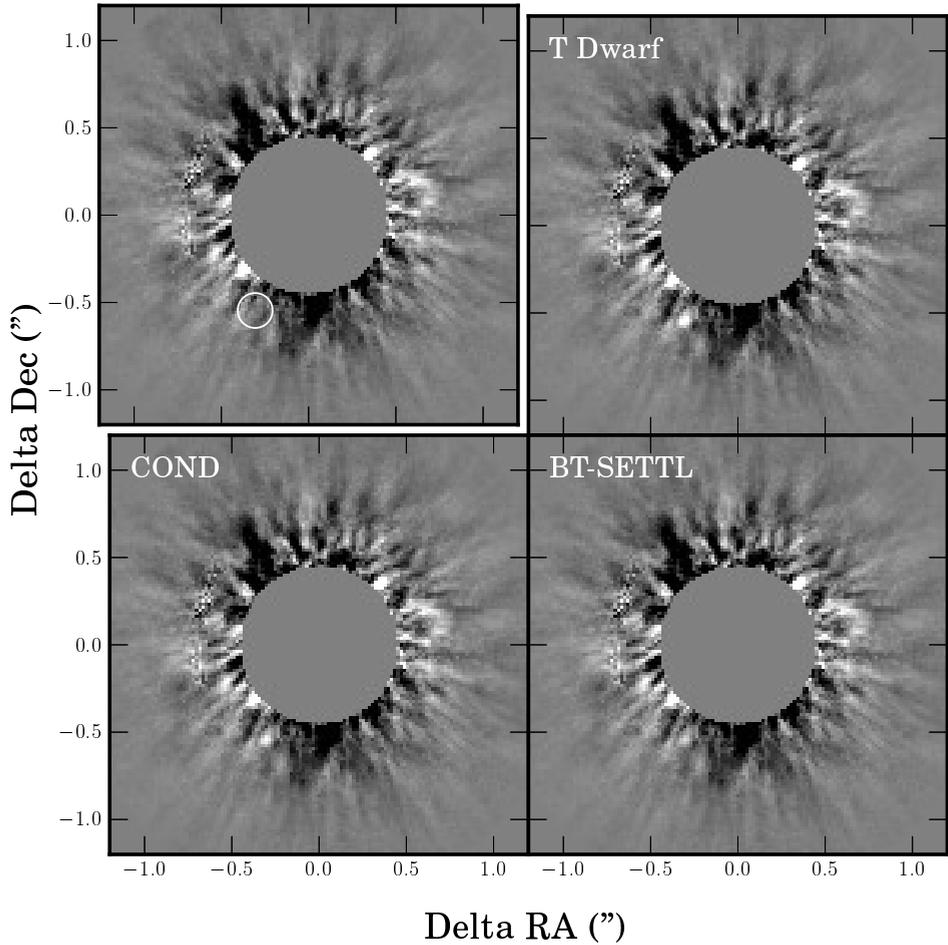
Figure 4.1 Upper left: the combined NICI *H*-band image reduced with PCA with a white circle at the expected location of the companion. The three other images have a fake companion injected into the raw data at the location of the expected planet. The contrast of the artificial companions are 11.6 mag for the T dwarf, 12.0 mag for the COND model, and 12.5 mag for the BT-SETTL model.
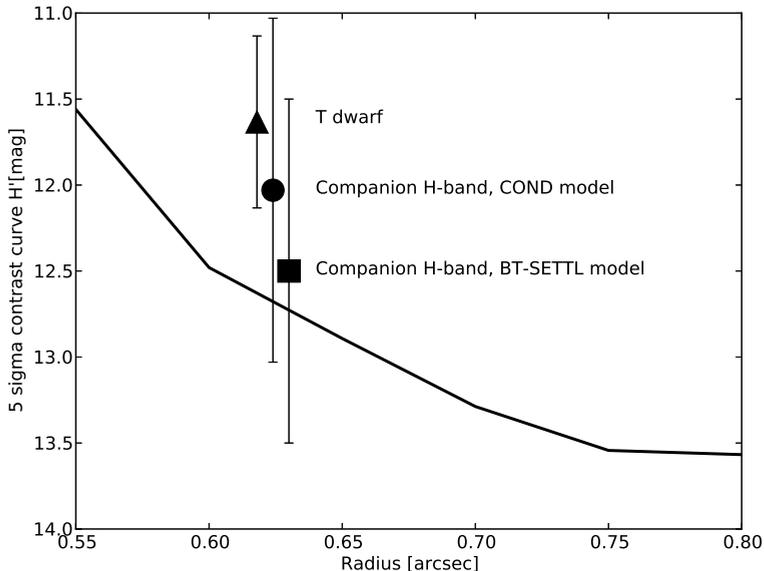
Figure 4.2 Contrast curve for *H*-band NICI data on HD 95086 generated by inject-ing artificial planets in the three nights of data. The circle, square, and triangle indicate the expected *H*-band contrast for a 17 Myr COND model planet, BT-SETTL model planet, and T dwarf, respectively. The square and triangle are slightly offset from the expected angular separation (0.′′624) for clarity.

separation (0.′′624) of the expected companion if it were a T dwarf (11.6 mag), COND model planet (12.0 mag), and BT-SETTL model planet (12.5 mag) (for details see Section 4.4.2).

We injected artificial sources in all three nights of data combined to determine the 5σ detection limit. The background star was used to generate the artificial planets by rescaling the flux to between 10 and 14 mag fainter than the primary star, from 0.′′55 to 0.′′8 in 0.′′05 increments.

The signal-to-noise (S/N) of the resulting fake planet is determined by the following equation:

$$(S/N)_{\mathrm{planet}} = \frac{F_{\mathrm{planet}}}{\sigma(r)\sqrt{\pi r_{\mathrm{ap}}^2}}$$

where F_{planet} is the sum of the flux in an aperture with a radius, r_{ap}, of 2 pixels, σ is the root mean square of the pixels in a 340° arc at the same radius around the star (excluding the planet itself), and r is the width of the arc (2 pixels). We can then construct the distribution of S/N at various source magnitudes, and determine the 5σ detection limit by interpolation at a given radius from the star. The 5σ contrast curve is shown in Figure 5.2.

To make sure the source brightness is not affected by the NICI coronagraph, we

extrapolated the transmission measured in the CH_4 filter (Boccaletti et al. 2013) assuming a linear relation with wavelength, and concluded that it should have nearly 100% transmission at greater than $0\rlap{.}''6$. Since the planet is detected at a separation of $0\rlap{.}''624$, this is within the 100% transmission regime.

4.4   Analysis

4.4.1   Stellar Parameters and Age

HD 95086 was kinematically selected as a member of Lower Cen-Crux (LCC) based on its *Hipparcos* astrometry by de Zeeuw et al. (1999), and it has been included in several later studies as a member (e.g., Rizzuto et al. 2012; Chen et al. 2012). The *mean* age of the LCC subgroup defined by the >1 $M_\odot$ stars is ~16–17 Myr, however, the inferred age spread of the group (~10 Myr) hints that adoption of the mean subgroup age for a given star may be problematic (Mamajek et al. 2002; Preibisch & Mamajek 2008; Pecaut et al. 2012). The revised *Hipparcos* astrometry for the star from van Leeuwen (2007) differs negligibly from the original value, and indeed Rizzuto et al. (2012) again included HD 95086 in a recent analysis, so we regard the kinematic membership as secure.

The *Hipparcos* catalog quotes photometry of $V = 7.36$ and $B - V = 0.230 \pm 0.004$. If the intrinsic colors of HD 95086 are similar to that of A8V dwarf stars, then their mean color is $B - V = 0.25$ (Pecaut & Mamajek 2013), with an rms spread of ± 0.04 mag. This is not surprising, as low reddening values ($E(B - V) < 0.05$ mag) are ubiquitous for stars within 90 pc in the general direction of HD 95086 (Reis et al. 2011). Based on this discussion, we adopt $A_V = 0.02 \pm 0.02$ mag as a reasonable estimate that brackets the range of plausible extinctions and confirm the spectral type discussion in Rameau et al. (2013b).

We calculate an absolute magnitude of $M_V \simeq 2.6$, which places the star near the main sequence (MS). The combined constraints of spectral type A8 ± 1 (assumed uncertainty) and restricting the plausible reddening value to be $E(B - V) < 0.05$ leads to an effective temperature estimate of 7550 ± 100 K ($\log(T_{\rm eff}) = 3.878 \pm 0.006$) and V-band bolometric correction of $BC_V = 0.040 \pm 0.002$ mag (statistical) ± 0.026 mag (systematic), where the systematic uncertainty reflects differences in the bolometric magnitude scales among six studies (Code et al. 1976; Balona 1994; Flower 1996; Bessell et al. 1998; Bertone et al. 2004; Masana et al. 2006). Combining the *Hipparcos* V magnitude (assuming ± 0.01 mag uncertainty), the revised *Hipparcos* parallax, and our stated extinction and bolometric magnitude values, we estimate the following parameters for HD 95086: apparent bolometric flux $f_{\rm bol} = 28.52 \pm 0.9$ pW m^{-2}, absolute V magnitude $M_V = 7.38 \pm 0.03$, absolute bolometric magnitude 2.60 ± 0.09, $\log(L/L_\odot) = 0.863 \pm 0.035$ dex.

In Figure 4.3, we plot the H-R diagram point for HD 95086 with Dartmouth isochrones from Dotter et al. (2008) adopting approximately protosolar composition of $Y = 0.26$ and $Z = 0.017$. The star is slightly above the zero-age main sequence (ZAMS), and appears consistent with pre-MS age 16 ± 2 Myr. Using three other sets of pre-MS evolutionary tracks, we find the following ages: 15 Myr (D'Antona et al. 1997), 17 Myr (Yi et al. 2003), and 24 Myr (Siess et al. 1997). Note that
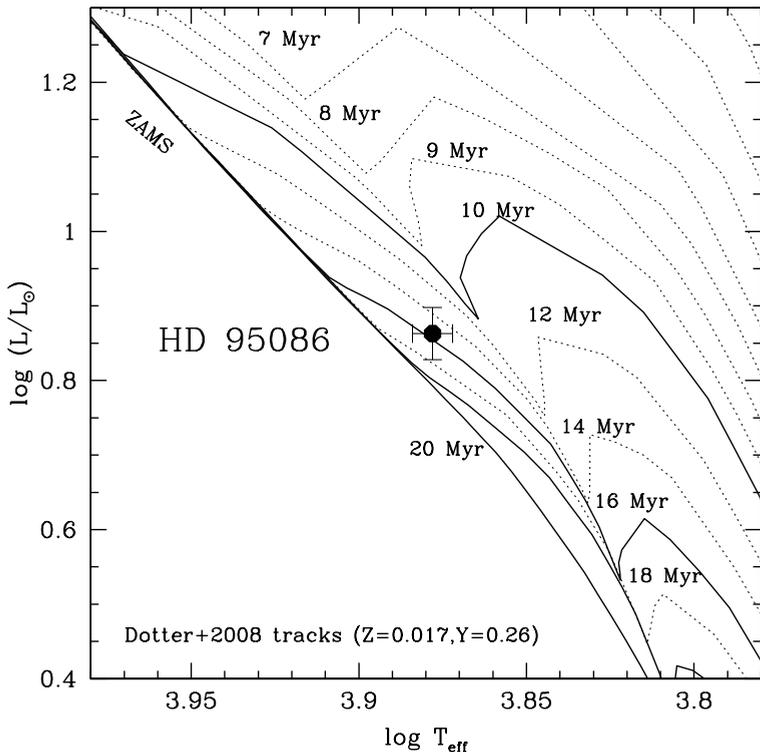
Figure 4.3 H-R diagram for HD 95086 with Dartmouth isochrones overlaid.

models are in general agreement on the mass of HD 95086: ~1.7 $M_\odot$. Taking into account the different models and observational uncertainties, we estimate a final individual pre-MS isochronal age estimate of HD 95086 of 17 Myr (±2 Myr statistical, ±4 Myr systematic, total uncertainty ~ ±4 Myr). This is commensurate with the mean LCC subgroup age (Mamajek et al. 2002; Pecaut et al. 2012).

Two factors which could conspire to ruin our age estimate are (1) unresolved binarity (which would move the star older, closer to the ZAMS), and (2) if the star is an interloper whose H-R diagram position and kinematics could conspire to masquerade the star appear as a likely LCC member. In the unlikely scenario that the star is an interloper, its H-R diagram position would be consistent with an MS isochronal age of ~270 Myr.

4.4.2 Color Constraints

At the angular separation of the planet ($0\rlap{.}''624$), we are sensitive to an H-band contrast of 12.7 mag relative to the host star for a 5σ point source detection. This is an apparent magnitude of 19.57 mag. Using the Rameau et al. (2013b) apparent L' magnitude of 16.49, we derive an $H-L'$ lower limit of 3.1±0.5 mag for the planet at 5σ.
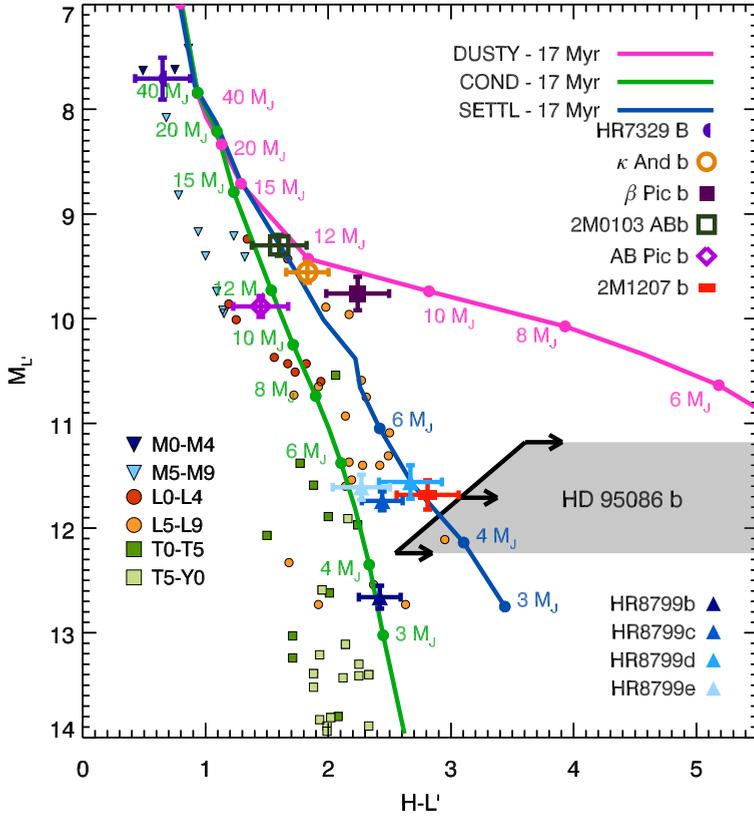
Figure 4.4 Color magnitude diagram showing the $M_{L'}$ vs. $H - L'$ color of various substellar objects as well as tracks from evolutionary and atmospheric models. The shaded area is defined as a lower limit on the color of the HD 95086 companion.

The expected H-band contrast of the planet, given the measured L' magnitude (Rameau et al. 2013b), is 12.03±1.0 mag based on the COND model (Baraffe et al. 2003) and 12.50±1.0 mag based on the BT-SETTL model (Allard et al. 2013, ; Figure 5.2). The error is propagated from the uncertainty in the L' magnitude in Rameau et al. (2013b). The contrast curve demonstrates that our data are sensitive enough to detect a planet for the COND models (S/N>~4) and the BT-SETTL models (S/N>~2.5). Instead, we detect no point sources at such brightness in our H-band data.

The expected H magnitudes for an unreddened A/F star, M dwarf, and T dwarf interlopers which are at the same distance as HD 95086 are 16.5, 17.5, and 18.5 (see triangle, Figure 5.2), respectively. This is far brighter than our 19.57 detection limit at the angular separation of the companion. If the companion were a T dwarf at the distance of HD 95086 or closer, we would have seen it based on our color and sensitivity limits. An unreddened K giant would have to be at 40

kpc in order to have the same L' magnitude as the companion, and its $H - L'$ color would be 0.17, which we would have detected. The companion is very unlikely to be a background source due to the proper motion seen in Rameau et al. (2013b).

We compared the constraints on the photometry of HD 95086 b (shaded area) in a color–magnitude diagram (Figure 4.4) to the photometry of field M, L, and T dwarfs (Leggett et al. 2013), of young (12–30 Myr) companions (HR7329 B, Neuhäuser et al. (2011); Kappa And b, Carson et al. (2013); Bonnefoy et al. (2013a); β Pic b, Lagrange et al. (2010), Bonnefoy et al. (2013); 2M0103 ABb, Delorme et al. (2013); AB Pic b, Chauvin et al. (2005); 2M1207 b, Chauvin et al. (2004); HR8799 bcde, Marois et al. (2008), Skemer et al. (2012), and to the COND model, the DUSTY model Chabrier et al. (2000), and the BT-SETTL model generated for an age of 17 Myr. The $H - L'$ color of HD 95086 b makes it one of the reddest companions directly imaged so far. It is inconsistent with COND models, consistent with 4–5 M_{Jup} BT-SETTL models, and consistent DUSTY models at an age of 17 Myr. The color is also at least 2 mag redder than the ones of typical M field dwarfs and 1 mag redder than the colors of early-L dwarfs. The location of the companion with respect to the sequence of field brown dwarfs and to evolutionary tracks suggest a high dust content in its photosphere (possibly in the form of thick clouds; Currie et al. 2011). In summary, current constraints on the photometry of HD 95086 b further suggest that the source is likely a bound companion with peculiar atmospheric properties related to low surface gravity. A new astrometric epoch is still mandatory to confirm that the companion is comoving with the star, and then exclude the possibility that it could be an extincted or intrinsically red background or foreground object.

4.4.3   Proper Motion of Background Sources

There are 20 additional point sources visible in the H-band distortion corrected images, ranging from 2" to 10" away from HD 95086. Using NICMOS *HST* data from 2007 (PI: J. Rhee), we examine the proper motion of these sources relative to HD 95086 with a five-year baseline. The proper motion of all the point sources in the field of view are consistent with background sources.

4.5   Conclusion

We analyze H-band NICI data aiming to re-detect the planet HD 95086 b. We detect no point source in our data, verified through three independent pipelines. Our deep dataset provides an $H - L'$ lower limit, which rules out foreground L/T dwarfs and distant background K giant contaminants. If the object is bound to HD 95086, our color limit is inconsistent with the COND model, marginally consistent with the BT-SETTL model, and consistent with the DUSTY model at our derived age of 17±4 Myr. Future astrometric observations are necessary to establish the nature of this object. This extremely red object demonstrates the importance of L' band for planet detection as planets may be much redder than models predict.

Acknowledgements

References

Allard, F., Homeier, D., Freytag, B., et al. 2013, Memorie della Societa Astronomica Italiana Supplementi, 24, 128

Amara, A., & Quanz, S. P. 2012, MNRAS, 427, 948

Balona, L. A. 1994, MNRAS, 268, 119

Baraffe, I., Chabrier, G., Barman, T. S., Allard, F., & Hauschildt, P. H. 2003, A&A, 402, 701

Bertone, E., Buzzoni, A., Chávez, M., & Rodríguez-Merino, L. H. 2004, AJ, 128, 829

Bessell, M. S., Castelli, F., & Plez, B. 1998, A&A, 333, 231

Boccaletti, A., Lagrange, A.-M., Bonnefoy, M., Galicher, R., & Chauvin, G. 2013, A&A, 551, L14

Bonnefoy, M., Currie, T., Marleau, G.-D., et al. 2013a, ArXiv e-prints

Bonnefoy, M., Boccaletti, A., Lagrange, A.-M., et al. 2013b, A&A, 555, A107

Carson, J., Thalmann, C., Janson, M., et al. 2013, ApJL, 763, L32

Chabrier, G., Baraffe, I., Allard, F., & Hauschildt, P. 2000, ApJ, 542, 464

Chauvin, G., Lagrange, A.-M., Dumas, C., et al. 2004, A&A, 425, L29

Chauvin, G., Lagrange, A.-M., Zuckerman, B., et al. 2005, A&A, 438, L29

Chauvin, G., Faherty, J., Boccaletti, A., et al. 2012, A&A, 548, A33

Chen, C. H., Pecaut, M., Mamajek, E. E., Su, K. Y. L., & Bitner, M. 2012, ApJ, 756, 133

Code, A. D., Bless, R. C., Davis, J., & Brown, R. H. 1976, ApJ, 203, 417

Currie, T., Burrows, A., Itoh, Y., et al. 2011, ApJ, 729, 128

Currie, T., Debes, J., Rodigas, T. J., et al. 2012, ApJL, 760, L32

D'Antona, F., Caloi, V., & Mazzitelli, I. 1997, ApJ, 477, 519

de Zeeuw, P. T., Hoogerwerf, R., de Bruijne, J. H. J., Brown, A. G. A., & Blaauw, A. 1999, AJ, 117, 354

Delorme, P., Gagné, J., Girard, J. H., et al. 2013, A&A, 553, L5

Dotter, A., Chaboyer, B., Jevremović, D., et al. 2008, ApJS, 178, 89

Flower, P. J. 1996, ApJ, 469, 355

Hubeny, I., & Burrows, A. 2007, ApJ, 669, 1248

Kalas, P., Graham, J. R., Chiang, E., et al. 2008, Science, 322, 1345

Kouwenhoven, M. B. N., Brown, A. G. A., Zinnecker, H., Kaper, L., & Portegies Zwart, S. F. 2005, A&A, 430, 137

Lafrenière, D., Marois, C., Doyon, R., Nadeau, D., & Artigau, É. 2007, ApJ, 660, 770

Lagrange, A.-M., Bonnefoy, M., Chauvin, G., et al. 2010, Science, 329, 57

Leggett, S. K., Morley, C. V., Marley, M. S., et al. 2013, ApJ, 763, 130

Mamajek, E. E., Meyer, M. R., & Liebert, J. 2002, AJ, 124, 1670

Marois, C., Lafrenière, D., Doyon, R., Macintosh, B., & Nadeau, D. 2006, ApJ, 641, 556

Marois, C., Macintosh, B., Barman, T., et al. 2008, Science, 322, 1348

Masana, E., Jordi, C., & Ribas, I. 2006, A&A, 450, 735

Meshkat, T., Kenworthy, M., Quanz, S. P., & Amara, A. 2013, submitted to ApJ

Neuhäuser, R., Ginski, C., Schmidt, T. O. B., & Mugrauer, M. 2011, MNRAS, 416, 1430

Pecaut, M. J., & Mamajek, E. E. 2013, ArXiv e-prints

Pecaut, M. J., Mamajek, E. E., & Bubar, E. J. 2012, ApJ, 746, 154

Preibisch, T., & Mamajek, E. 2008, Handbook of Star Forming Regions, Volume II, 235

Rameau, J., Chauvin, G., Lagrange, A.-M., et al. 2013, ApJL, 772, L15

Reis, W., Corradi, W., de Avillez, M. A., & Santos, F. P. 2011, ApJ, 734, 8

Rizzuto, A. C., Ireland, M. J., & Zucker, D. B. 2012, MNRAS, 421, L97

Siess, L., Forestini, M., & Dougados, C. 1997, A&A, 324, 556

Skemer, A. J., Hinz, P. M., Esposito, S., et al. 2012, ApJ, 753, 14

Stephens, A. W., Frogel, J. A., Ortolani, S., et al. 2000, AJ, 119, 419

Stephens, D. C., Leggett, S. K., Cushing, M. C., et al. 2009, ApJ, 702, 154

Toomey, D. W., & Ftaclas, C. 2003, Proc. SPIE, 4841, 889

van Leeuwen, F. 2007, A&A, 474, 653

Vigan, A., Bonnefoy, M., Chauvin, G., Moutou, C., & Montagnier, G. 2012, A&A, 540, A131

Wahhaj, Z., Liu, M. C., Biller, B. A., et al. 2011, ApJ, 729, 139

Yi, S. K., Kim, Y.-C., & Demarque, P. 2003, ApJS, 144, 259

Chapter 5

Discovery of a Low-Mass Companion to the F7V star HD 984

We report the discovery of a low-mass companion to the nearby ($d = 47$ pc) F7V star HD 984. The companion is detected $0\farcs19$ away from its host star in the L' band with the Apodizing Phase Plate on NaCo/VLT and was recovered by L'-band non-coronagraphic imaging data taken a few days later. We confirm the companion is co-moving with the star with SINFONI integral field spectrograph $H + K$ data. We present the first published data obtained with SINFONI in pupil-tracking mode. While HD 984 has been argued to be a kinematic member of the 30 Myr-old Columba group, and its HR diagram position is not altogether inconsistent with being a ZAMS star of this age, we independently estimate a main sequence isochronal age of $2.0^{+2.1}_{-1.8}$ Gyr which does not rely on this kinematic association. The mass of directly imaged companions are usually inferred from theoretical evolutionary tracks, which are highly dependent on the age of the star. Based on the age extrema, we demonstrate that with our photometric data alone, the companion's mass is highly uncertain: between 33 and 120 M_{Jup} (0.03-0.11 $M_\odot$) using the COND evolutionary models. We compare the companion's SINFONI spectrum with field dwarf spectra to break this degeneracy. Based on the slope and shape of the spectrum in the H-band, we conclude that the companion is an M6.0 ± 0.5 dwarf. The age of the system remains unconstrained, as M dwarfs are poorly fit on low-mass evolutionary tracks. This discovery emphasizes the importance of obtaining a spectrum to spectral type companions around F-stars.

T. Meshkat, M. Bonnefoy, E. E. Mamajek, S. P. Quanz, G. Chauvin, M. A. Kenworthy, J. Rameau, M. R. Meyer, A.-M. Lagrange, J. Lannier, P. Delorme
Submitted to *Monthly Notices of the Royal Astronomical Society*

5.1 Introduction

Young stars are the primary targets of exoplanet imaging surveys because associated planets are warm and therefore bright in the infrared. A handful of brown dwarfs and low-mass stellar companions have been found in these surveys (PZ Tel B; Biller et al. 2010, CD-35 2722 B; Wahhaj et al. 2011, HD 1160 B,C; Nielsen et al. 2012). Masses of directly imaged companions are estimated from the companion's luminosity and theoretical evolutionary models, which are very sensitive to the age and distance of the host star.

The companion mass-ratio distribution (CMRD) quantifies the mass ratio of a binary system (Reggiani & Meyer 2013). Based on observational data, the initial mass function (IMF) for brown dwarfs and very-low-mass-stars (0.08-$0.2 M_\odot$) likely differs from stars (Thies et al. 2015). The primary formation mechanisms for these low-mass companions, including fragmentation and capture, is still under debate, making each new discovered low-mass companion an important test case for the theoretical formation mechanisms of low-mass companion. The orbital motion of the companion around the primary star, measured as a small arc on the sky, can be used to find orbital solutions (Pearce et al. 2015). Some orbital properties, such as eccentricity, can be constrained with only two measurements (Biller et al. 2010). Additionally, with multiple epoch astrometric measurements from direct imaging and radial velocity data, the dynamical mass of a companion can be measured. This acts as an important comparison with the inferred companion masses from theoretical evolutionary models (Bonnefoy et al. 2009; Dupuy et al. 2015; Close et al. 2007).

We report the detection of a companion around the F7V star HD 984 (HIP 1134). This star has been part of many imaging surveys searching for planets (Brandt et al. 2014; Rameau et al. 2013a) due to its proximity, brightness ($d = 47.1 \pm 1.4$ pc; V $= 7.3$; ESA 1997; van Leeuwen 2007), and proposed youth (30 Myr, Zuckerman et al. 2011). However, no comoving companions have yet been reported. Ground-based sub-mm and *Spitzer* infrared photometry of HD 984 have not detected any evidence of a dusty debris disk (Mamajek et al. 2004; Carpenter et al. 2009; Ballering et al. 2013).

In Section 6.2 we describe our coronagraphic and non-coronagraphic observations with NaCo on the VLT, and our SINFONI/VLT integral field spectrographic data. In Section 5.3 we measure the companion's photometry and astrometry. In Section 5.4 we discuss previous age estimates of HD 984, and estimate its main sequence isochronal age. In Section 5.5 we estimate the mass of the companion based on evolutionary models and spectral analysis. We conclude in Section 5.6.

5.2 Observations

5.2.1 NaCo/VLT

Observations of HD 984 were taken on UT 2012 July 18 and 20 (089.C-0617(A), PI: Sascha Quanz) at the Very Large Telescope (VLT)/UT4 with NaCo (Lenzen et al. 2003; Rousset et al. 2003). The Apodized Phase Plate coronagraph (APP;

Kenworthy et al. 2010; Quanz et al. 2010) was used for diffraction suppression thus increasing the chances of detecting a companion very close to the target star. Data were obtained with the L27 camera, in the L'-band filter ($\lambda = 3.80\mu$m and $\Delta\lambda = 0.62\mu$m). The visible wavefront sensor was used with HD 984 as the natural guide star. We observed in pupil tracking mode (Kasper et al. 2009) for Angular Differential Imaging (ADI; Marois et al. 2006). We intentionally saturated the PSF core to increase the signal-to-noise from potential companions in each exposure. Unsaturated data were also obtained to calibrate photometry relative to the central star.

The APP suppresses diffraction over a 180° wedge on one side of the target star. Excess scattered light is increased on the other side of the target that is not used in the data analysis. Two datasets were obtained with different initial position angles (P.A.) for full 360° coverage around the target star. The field rotation was 47°.4 in the first hemisphere and 42°.5 in the second hemisphere.

Direct imaging observations of HD 984 were obtained on VLT/NaCo on UT 2012 July 20 (089.C-0149(A), PI: Julien Rameau). The data were taken with the L27 camera on NaCo in ADI pupil tracking mode. Both the saturated and unsaturated data were imaged in L'-band with the same exposure time, but in the unsaturated images a neutral density filter (ND_LONG) was used. The field rotation was 41°.3 in the direct imaging data. All datasets were obtained in cube mode. Each APP cube contains 120 frames, with an integration time of 0.5 s per frame. The total integration time in the APP was 60 min in hemisphere 1 (60 cubes) and 66 min in hemisphere 2 (66 cubes). Unsaturated APP exposures were 0.056 s per frame (222 frames in 12 cubes), with a total time on target of 150 seconds. The direct imaging cubes contain 100 frames, with 0.2 s per frame, with a total integration time of 48 min for the saturated data and 202 seconds for the unsaturated data.

A dither pattern on the detector was used to subtract sky background and detector systematics from both datasets, as detailed in Kenworthy et al. (2013). Data cubes are subtracted from each other, centroided and averaged over. Optimized principal component analysis (PCA) is run on both of the APP hemispheres and direct imaging data independently, following Meshkat et al. (2014). Six principal components are used to model the stellar PSF, which results in the highest signal-to-noise detection of the companion. PCA processed frames are derotated and averaged to generate the final image with North facing up.

5.2.2   SINFONI/VLT

Data were obtained on HD 984 with the AO-fed integral field spectrograph SIN-FONI (Eisenhauer et al. 2003; Bonnet et al. 2004) at the VLT on UT 2014 September 9 (093.C-0626, PI: G. Chauvin) in $\sim 0\rlap{.}''5$ seeing. The $H + K$ grating was used, which has a resolution of ~1500. The spatial sampling was 12.5 mas×25 mas (in the horizontal and vertical directions, respectively) resulting in a field of view of $0\rlap{.}''8 \times 0\rlap{.}''8$. We obtained 42 raw cubes of the target, each consisting of 10×4s coadded exposures. Similar to the NaCo observations, data were obtained in pupil tracking (PT) mode (Hau et al. in prep). The companion rotated 49.26° around

the center of the field of view during our 28 min integration.

The instrument pipeline version 2.5.2 [1] was used to correct the raw science frames from hot and non-linear pixels, detector gain, and distortion. Final cubes were reconstructed from the resulting frames, associated wavelength map, and slitlet positions. Data cubes were corrected for OH lines and background emission using a dedicated algorithm (Davies 2007) implemented in the pipeline.

The wavelength-dependent drift in the star position, caused by the atmospheric refraction, was registered (modeled by a 3rd order polynomial) and corrected. We took the mean of the parallactic angle values at the beginning and end of a given exposure, which is stored in the cube file headers. We processed the cubes with the classical-ADI (CADI) algorithm (Marois et al. 2006) to suppress the stellar flux independently at each wavelength (2172 independent spectral resolution elements).

Data were corrected for telluric absorption lines using the observations of an A3V standard star (HD 2811) obtained close in time to HD 984 and at a comparable airmass. The resulting spectrum of HD 984 was flux-calibrated using the 2MASS *H*-band magnitude of the star (Cutri et al. 2003) and a spectrum of Vega.

5.3   Photometry and Astrometry of HD 984 B

5.3.1   NaCo/VLT

The companion was clearly detected very close to the star (Figure 5.1, APP hemisphere 1 on top-left and direct imaging on top-right). The companion detection was confirmed using the *Pynpoint* pipeline (Amara & Quanz 2012) and the IPAG-ADI pipeline (Chauvin et al. 2012). The detection was robust against changing the number of principal components used in the stellar PSF model.

We used artificial negative companions to determine the astrometry and photometry of the companion (following Meshkat et al. 2015). The unsaturated stellar PSF was used to generate artificial companions in the APP and direct imaging data. A scaling factor of 0.018 was applied to the direct imaging unsaturated data to account for the attenuation from the neutral density filter. We injected artificial negative companions into the data near the expected position of the companion in steps of 0.1 pixels. The artificial companion contrast was varied from 5.0 to 7.0 in steps of 0.01 mag. The chi-squared minimization over the λ/D patch at the location of the artificial negative companion yielded the following results.

Based on this analysis, the companion contrast in the APP data is best approximated as $\Delta L' = 6.0 \pm 0.2$ mag ($L' = 12.0 \pm 0.2$mag). The angular separation of the companion is $0''.19 \pm 0.02$, which corresponds to a projected separation of 9.0 ± 1.0 AU for the stellar distance of 47.1 ± 1.4 pc from van Leeuwen (2007). The position angle (P.A.) of the companion is $108°.8 \pm 3°.0$. The error in the measurements is due to the range in artificial companions which successfully subtract the companion signal.

The companion contrast in the direct imaging data is $\Delta L' = 5.9 \pm 0.3$ mag at $0''.208 \pm 0.023$ (9.8 ± 1.1 AU). The P.A. of the companion is $108°.9 \pm 3°.1$ corrected

---

[1]http://www.eso.org/sci/software/pipelines/sinfoni/sinfoni-pipe-recipes.html
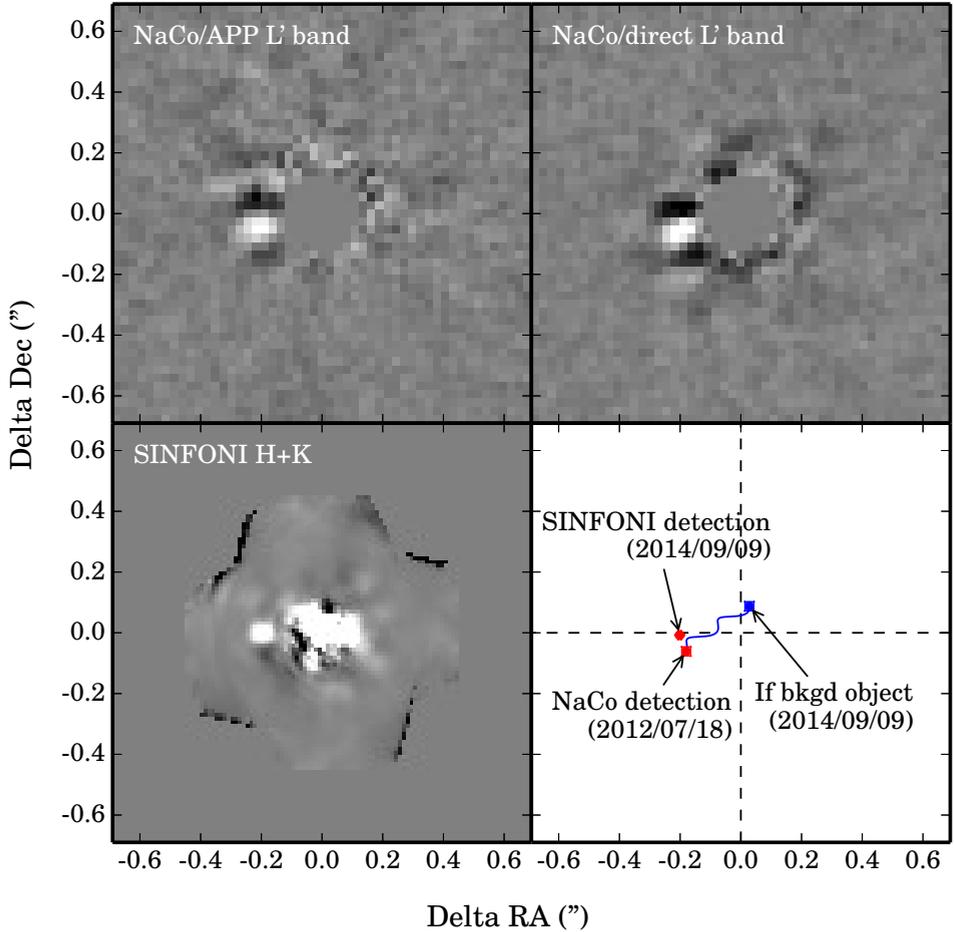
Figure 5.1 Top-left: Final PCA processed image of HD 984 APP hemisphere 1 data with North facing up. Twenty principal components were used to model the stellar PSF in this image. Top-right: Final PCA processed image of HD 984 from direct imaging data with North facing up. Six principal components were used to model the stellar PSF. Bottom-left: Collapsed $H + K$ SINFONI IFS data cubes processed with CADI, with North facing up. All three images are displayed in the same color scale. Bottom-right: The position of the companion is plotted as red points for both the VLT/NaCo dataset epoch (UT 2012 July 18) and the VLT/SINFONI epoch (UT 2014 September 9). The blue point is the position of the companion if it were a background source at the time of the VLT/SINFONI dataset epoch (UT 2014 September 9). Error bars are included for all points.
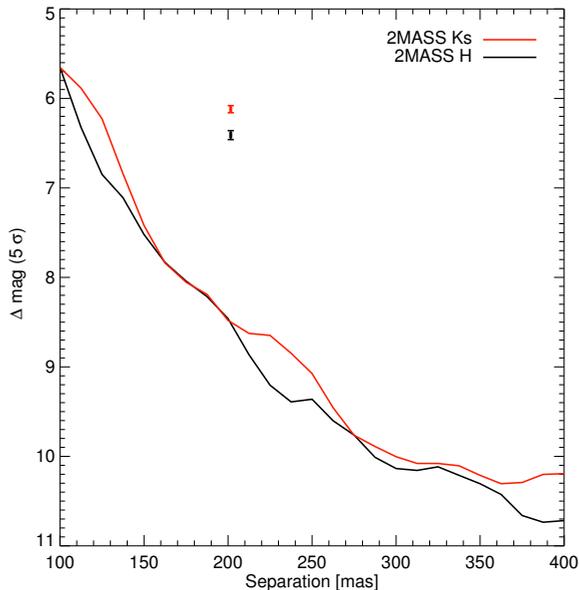
Figure 5.2 Contrast curves for the SINFONI HD 984 *H* (black curve) and *Ks* (red curve) data, for CADI processing. The companion detection is shown as a point with error bars in *H* (black) and *Ks* (red), respectively.

to true North orientation, calibrated using θ Ori, observed at the same epoch with the same mode. The θ Ori stars TCC058, 057, 054, 034, and 026 were used to determine the true North 0.41±0.07° with a plate scale of 27.11±-0.02 mas (Rameau et al. 2013a). The astrometry and photometry of the companion is in good agreement between the two datasets. Since the two datasets were only taken two days apart, we do not consider them separate epochs, but rather a confirmation that this companion is not an artifact.

5.3.2   SINFONI

The companion was detected in *H+K* band IFS SINFONI data (Figure 5.1 bottom-left). These data are the first published results demonstrating the capabilities of the SINFONI instrument in PT mode. The parallactic angle associated with each of the 43 data cubes was estimated by taking the mean of the parallactic angle at the beginning and the end of an exposure. We applied an additional clockwise rotation of 210.92° to the frames at the ADI reduction step to properly realign the field of view to the North. True North was estimated using GQ Lup SINFONI observations on UT 2013 August 24, which were calibrated with NaCo observations of the same source on UT 2012 March 3, assuming orbital motion is negligible between the epochs (following the formulae described in the Appendix).

The companion is detected in all of our ADI analyses. We discovered that subtracting the stellar halo of the data cubes collapsed in wavelength followed by

a realignment of the frame to the North also allowed detection of the companion. Unlike ADI processing, this allows for a measurement of the position of the companion without the biases associated with the self-subtraction of the companion PSF (Bonnefoy et al. 2011). We selected 10 frames corresponding to the first 10 cubes of the PT sequence and median-combined them after realigning to true North. This provided a good removal of residual speckles from the stellar halo. We found that HD 984 B lies at a PA=$92.2 \pm 0.5°$ and a separation $\rho = 201.6 \pm 0.4$ mas. The error considers uncertainties in our fitting function as well as true North. We also make the assumption that the instrument absolute orientation on sky did not vary between our UT 2014 September 9 observations and the True North calibration (UT 2013 August 24) with GQ Lup. The separation assumes a plate scale of 12.5 mas/pixel reported in the instrument user manual. The plate scale at the time of HD 984 observations could not be measured.

HD 984 is a relatively high proper motion star, with $\mu_{\alpha*}$, μ_{δ} = 102.79 ± 0.78, -66.36 ± 0.36 mas yr^{-1} (van Leeuwen 2007). If the companion were a background source, it should be due North of HD 984 and at a projected separation of $< 0''1$ in the SINFONI data (Figure 5.1, bottom-right). We estimate that the companion is very unlikely to be a stationary background source, with an estimated χ^2 <1E-6 based on the two epoch companion detections, stellar proper motion, distance estimates, and the astrometric error on the SINFONI dataset (which is dependent on the plate scale). The new P.A. of the companion is consistent with Keplerian orbital motion. Based on the astrometry of the companion, we confirm it is bound to the star and not a background object.

The companion flux was integrated in a 6 pixel wide circular aperture in the processed CADI cubes to generate the spectrum. We applied the same procedure to HD 984. We corrected for flux losses in the companion's spectrum (caused by the image processing algorithms) by adding artificial sources. We used the unsaturated primary star itself to scale and inject artificial sources in the data. Artificial sources were added in each wavelength at the same projected separation as the companion, but with a P.A. difference of -90, +90, and +180°. The resulting spectrum was corrected for the telluric lines using the primary spectrum. We obtained the final flux-calibrated spectrum of the companion by multiplying the flux ratio between the system components and the flux-calibrated spectrum of the star. Based on the flux ratio between HD 984 and B in *H* and *Ks*-band, we estimate H_{2MASS} = 12.58 ± 0.05 mag and Ks_{2MASS} = 12.19 ± 0.04 mag for the companion. The spectrum of the companion is analyzed in Section 5.5.

Figure 5.2 shows contrast curves comparing the sensitivity to point sources in the data processed with the CADI algorithm in *H* and *Ks*-band. The contrast curve was generated following Chauvin et al. (2015). We injected fake planets every 10 pixels radially at P.A.s of 0, 120, and 240° between 125 and 375 mas, in order to correct for flux losses. The fake planets are created by scaling the flux of the primary star. We created a pixel-to-pixel noise map by sliding a box of 5×5 pixels from the star to the limit of the SINFONI field of view. The 5σ detection limit is found by dividing the pixel-to-pixel noise map by the flux loss, taking into account the relative calibration between the fake planet and the primary star.
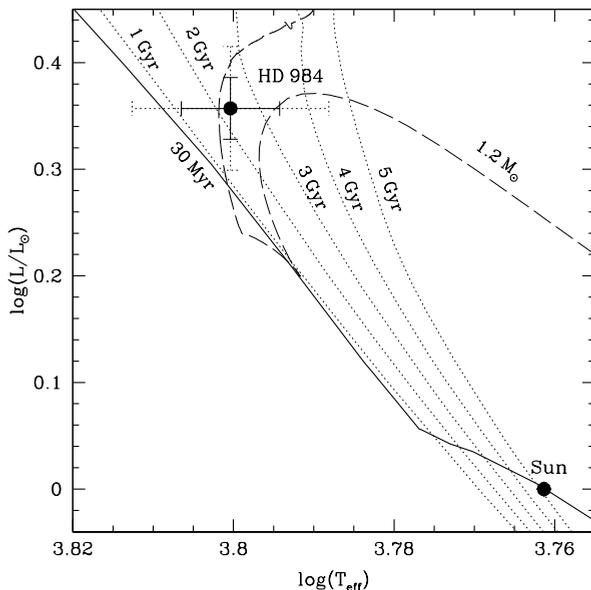
Figure 5.3 HR diagram position of HD 984 and the Sun, with isochrones and evolutionary tracks from Bressan et al. (2012) overlaid (z = 0.017), with 1σ solid line and 2σ dotted line error bars. The solid line is a 30 Myr isochrone corresponding to the purported age of the Columba group. Dotted lines are isochrones with ages of 1, 2, 3, 4, 5 Gyr. The dashed line is a 1.20 ± 0.06 (95%CL) $M_\odot$ track.

5.4 Age of HD 984

5.4.1 Previous Age Estimates

Zuckerman et al. (2011) and Malo et al. (2013) consider HD 984 to be a member of the Columba group with an age of 30 Myr (Torres et al. 2008). However, isochronal ages of <0.48 Gyr (68%CL; Takeda et al. 2007), $1.2^{+0.7}_{-0.9}$ Gyr (Valenti & Fischer 2005), and $3.1^{+1.0}_{-1.6}$ Gyr (Holmberg et al. 2009) have been estimated. HD 984 is notably chromospherically and coronally active. Wright et al. (2004) estimate an age of 0.49 Gyr based on chromospheric activity, however the star has mass ~1.2 $M_\odot$, so activity-age or gyrochronology relations for Sun-like stars are inapplicable (e.g. Mamajek & Hillenbrand 2008). Malo et al. (2013) have convincingly shown that HD 984 is consistent with comoving with Columba. However, there remains the possibility that HD 984 could be a kinematic interloper.

5.4.2 Stellar Parameters and Isochronal Age

HD 984 is a V = 7.32 mag (ESA 1997) F7V star (Houk & Swift 1999) at distance 47.1 ± 1.4 pc (van Leeuwen 2007, $\varpi = 21.21 \pm 0.64$ mas). It is not listed in latest

Property	HD 984		HD 984 B
Distance (pc)[a]		47.1 ± 1.4	
Age (Myr)[b]		$2.0^{+2.1}_{-1.8}$	
A_V [c]		0.02 ± 0.02	
$T_{\rm eff}$	6315 ± 89		2777^{+127}_{-130} [d]
			2900 ± 200 [e]
Spectral type	F7V		M6.0 $\pm$ 0.5
$\log(L/L_\odot)$	0.36 ± 0.03		-2.815$\pm$0.024
Separation (")		201.6 ± 0.4	
P.A.(°)		92.2 ± 0.5	
H	6.170 ± 0.023		12.58 ± 0.05
Ks	6.073 ± 0.038		12.19 ± 0.04
L'	6.0 ± 0.1		12.0 ± 0.2

[a] *Hipparcos* catalog (van Leeuwen 2007).
[b] This work.
[c] Schlegel et al. (1998) and Reis et al. (2011).
[d] Based on the spectral type conversion scale of Stephens et al. (2009).
[e] Based on BT-COND and GAIA synthetic spectra.

Table 5.1 System properties

version[2] of the Washington Double Star catalog (Mason et al. 2001). Considering the star's proximity, and the reddening maps of Schlegel et al. (1998) and Reis et al. (2011), we adopt $A_V = 0.02 \pm 0.02$ mag, $A_{Ks} = 0.002 \pm 0.002$ mag.

Numerous estimates of the effective temperature have been reported (e.g. Valenti & Fischer 2005; Masana et al. 2006; Schröder et al. 2009; Casagrande et al. 2011). We adopt the recent value from Casagrande et al. (2011) (6315 ± 89 K). From fitting the optical-infrared photometry to the dwarf color sequences from Pecaut & Mamajek (2013), and taking into account the previously mentioned extinction constraints, we derive an apparent bolometric magnitude of HD 984 to be $m_{bol} = 7.23 \pm 0.03$ and bolometric flux of 32.7 ± 0.9 pW m^{-2}. Employing the van Leeuwen (2007) parallax, this bolometric flux translates to a luminosity of $\log(L/L_\odot) = 0.36 \pm 0.03$ dex. Adopting the Casagrande et al. (2011) $T_{\rm eff}$, this is consistent with a stellar radius of 1.26 ± 0.06 R$_\odot$.

The HR diagram position of HD 984 is plotted in Figure 5.3 along with isochrones from Bressan et al. (2012) (for Z = 0.017). HD 984 is a main sequence star, and any derived isochronal age will have large uncertainties. Simulating the HR diagram position and interpolating their ages and masses, the isochronal ages are consistent with $2.0^{+2.1}_{-1.8}$ (95%CL) Gyr and 1.20 ± 0.06 (95%CL) M$_\odot$ (dashed line). However, as Figure 5.3 shows, a 2σ deviation (dashed error bar line) in both $T_{\rm eff}$ and $\log(L/L_\odot)$ are consistent with the 30 Myr isochrone. Based on the HR diagram, the age of HD 984 is between ZAMS ($\sim$ 30 Myr) and 4 Gyr.

5.5   Companion Characteristics

Based on the NaCo L' photometry alone, the companion mass can only be estimated from theoretical models which are highly dependent on the age of the star and lead to large uncertainties in the determined mass. Using the COND evolu-

[2]17 November 2014 version at http://vizier.cfa.harvard.edu/viz-bin/Cat?B/wds.
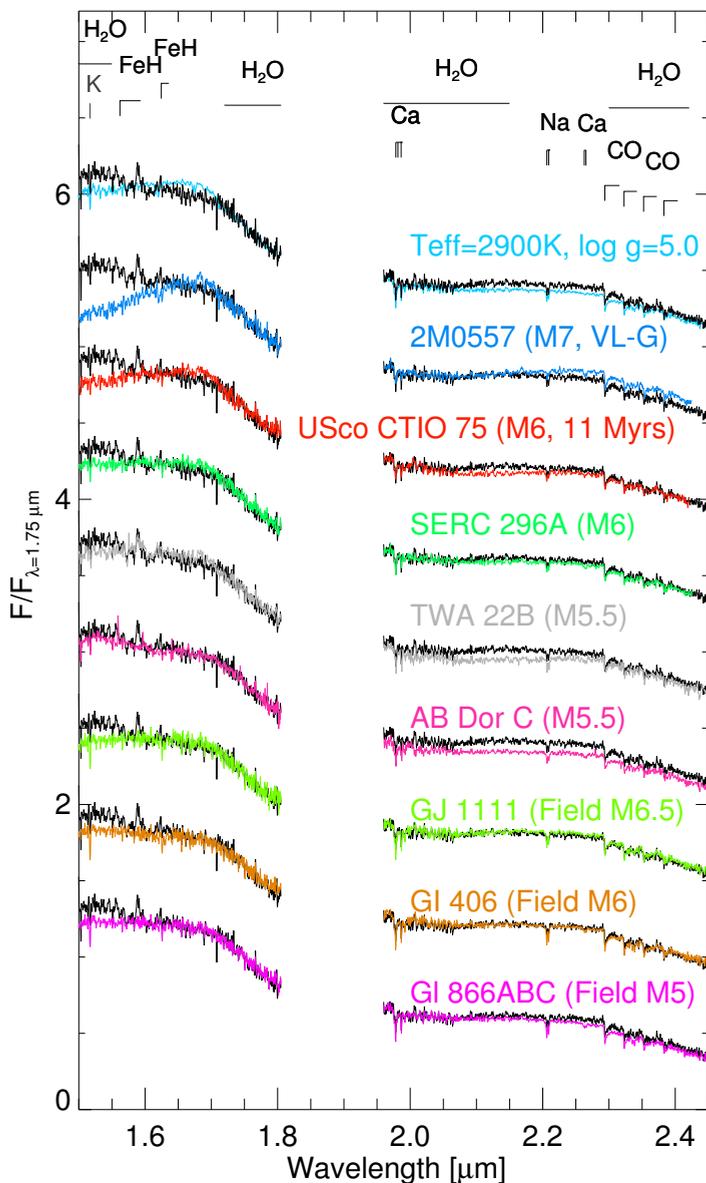
Figure 5.4 Comparison of HD 984 B spectrum (black) to those of field dwarfs, young companions, isolated objects, and to the best-fitting BT-COND spectrum. It enables us to conclude that HD 984 B is an M6.0 ± 0.5 dwarf.
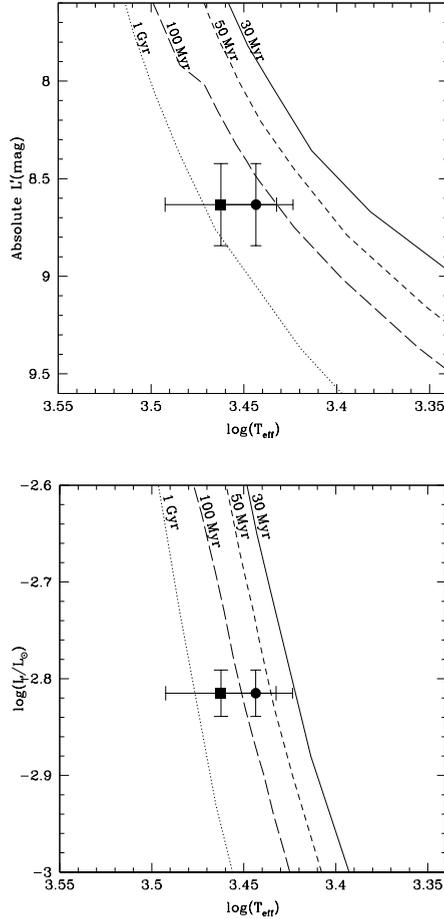
Figure 5.5 HR diagram position of HD 984 B in L'-band absolute mag (left) and bolometric luminosity (right) based on our spectral type estimate and adopting the Stephens et al. (2009) T_{eff} scale (circle), BT-COND and GAIA synthetic spectra (Brott & Hauschildt (2005); Allard et al. (2013): square). The COND evolutionary tracks (Baraffe et al. 2003) are plotted for 30, 50, 100 Myr and 1 Gyr. The >1 Gyr isochrones overlap with 1 Gyr in the COND model and thus are not shown. The companion L'-band position on the evolutionary tracks allows us to rule out an age of 50 Myr and younger. However, the companion bolometric luminosity position is nearly consistent with all evolutionary tracks, including those <50 Myr. Due to this inconsistency, the age of the system remains unconstrained.

tionary tracks (Baraffe et al. 2003), if the system is 30 Myr, the companion may be a $33 \pm 6M_{\mathrm{Jup}}$ young brown dwarf. If the system is 4 Gyr, the companion may be a $0.12 \pm 0.01 M_{\odot}$ low mass star, likely an M5-M6 dwarf. The errors are based on the uncertainty in the photometry and the distance of the star and do not include systematic uncertainties in the models. The range of companion masses based on the DUSTY evolutionary model (Chabrier et al. 2000) is within the errors of the values derived from the COND model: 30 Myr and $34 \pm 6M_{\mathrm{Jup}}$ or 4 Gyr and $0.12 \pm 0.01 M_{\odot}$. Thus, the companion mass estimation based on photometry is not significantly impacted by the evolutionary model chosen.

We compare our CADI analysis of the SINFONI spectrum (black spectrum, see Figure 5.4) with field dwarfs from the IRTF library (Rayner et al. 2009). We perform a least squares fit of the spectra to determine the best fit. In addition to the overall spectral slope from 1.5 to 2.45 μm, we aim to fit the following spectral features: the K I band at 1.516 μm, the Ca I triplet near 1.98 μm, the Na I doublet near 2.207 μm, the CO overtones longward of 2.3 μm, and the overall shape of the Ks-band which is sensitive to the collision-induced absorption of molecular hydrogen, thus to the atmospheric pressure and surface gravity. The companion has features later than M5 and midway between those of M5.5 and M6.5 field dwarfs. The SINFONI spectra of the young ($\leq$150 Myr) mid-M companions AB Dor C and TWA 22 B (Close et al. 2007; Bonnefoy et al. 2009) reproduce the pseudo-continuum in the H-band, but have bluer slopes than our companion, suggesting a later spectral type for HD 984 B. Spectra of other young mid-M dwarfs have a more triangular H-band shape than our object. The companion fits well with the M6 object SERC 296A (Thackrah et al. 1997; Allers & Liu 2013), which does not appear to be a good candidate member to any nearby associations based on its kinematics (Gagné et al. 2014), but has an age below $\sim$ 200 Myr due to lithium absorption. We therefore conclude that the HD 984 B is more likely a M6.0$\pm$0.5 object, which is younger than the typical field dwarf age ($\gg$1 Gyr). The subtype accuracy is due to the companion features being intermediate between a M5.5 and an M6.5.

The spectral type of M6.0 $\pm$ 0.5 corresponds to T_{eff} = 2777^{+127}_{-130} K using the conversion scale of Stephens et al. (2009). The T_{eff} accuracy is the quadratic combination of the spectral type estimate and systematic uncertainty. Conversely, the companion's pseudo-continuum shape and main absorption features are best reproduced by BT-COND and GAIA synthetic spectra (Brott & Hauschildt 2005; Allard et al. 2013) with T_{eff} = 2900 $\pm$ 200 K and log g=5.0-5.5 dex. The accuracy on T_{eff} is limited by the intrinsic differences and uncertainties between the atmospheric model grids (H-band is known to be badly reproduced by models, see Bonnefoy et al. 2013). Rajpurohit et al. (2013) find a T_{eff} range of 2700 to 3000 K for M5.5 to M6.5 dwarfs by fitting BT-Settl (Allard et al. 2013) spectra to optical spectra of M-dwarfs. This is consistent with our spectral type and derived temperature.

We calculate the bolometric luminosity based on our derived spectral type and H, Ks and L'-band companion magnitude measurements. We adopt bolometric corrections of $BC_{H(B)}$ = 2.588 $\pm$ 0.032 mag, $BC_{Ks(B)}$ = 2.940 $\pm$ $-$0.015 mag, and $BC_{L'(B)}$ = 3.260 $\pm$ 0.022 mag by interpolating between an M6 and M7 dwarf, using

bolometric correction and color information for M dwarfs from Pecaut & Mamajek (2013), Schmidt et al. (2014), and Dupuy & Liu (2012). By taking the weighted mean of our bolometric luminosity calculations from H, Ks and L'-band measurements, we find $\log(L/L_\odot)$=-2.815±0.024 dex. These results are summarized in Table 5.1.

Figure 5.5 compares the derived T_{eff} of the companion against COND evolutionary tracks of different ages. The companion absolute L' does not fit with COND evolutionary tracks less than 50 Myr (Figure 5.5). This older age is consistent with the lack of triangular H-band shape, the surface gravity inferred from the atmospheric models, and suggests that HD 984 is a Columba interloper. However, comparing our derived bolometric luminosity with COND evolutionary tracks suggests that the companion is consistent with an age of $\geq$30 Myr. This discrepancy is likely due uncertainties in atmospheric models and a systematic difference in the T_{eff} scale of Stephens et al. (2009) compared with the colors from the COND model (Baraffe et al. 2003). A similar model discrepancy was shown in Mamajek et al. (2013), where the COND evolutionary tracks do not accurately predict the empirical main sequence on a color-magnitude diagram. HD 984 B demonstrates the challenges in fitting M-dwarfs on low mass evolutionary tracks. Thus, the age of the system remains unconstrained, but we have demonstrated that this companion is consistent with an M6.0 ± 0.5 object.

5.6 Conclusion

We report the discovery of a low-mass companion to the F7V star HD 984. This companion was detected in L'-band with the Apodizing Phase Plate coronagraph and non-coronagraphic photometry with the NaCo instrument on the VLT. HD 984 has been reported to be part of the 30 Myr old Columba association. However, based on our independent analysis of its HR diagram position, we estimate a main sequence isochronal age of $2.0^{+2.1}_{-1.8}$ Gyr. Due to the age uncertainty, the companion mass may range from a low mass brown dwarf ($\sim$33 M_{Jup}) to an M dwarf ($\sim$0.11 $M_\odot$), using the COND evolutionary models.

We analyze the slope and shape of SINFONI $H + K$ IFU data of the companion compared with field M dwarfs. We conclude the companion is an M6.0 ± 0.5 dwarf. Using our derived spectral type, we aim to determine the age of the system by placing the companion L'-band absolute magnitude and bolometric luminosity on COND evolutionary tracks. While the L'-band HR diagram position allows us to rule out an age less than 50 Myr, the companion's bolometric luminosity position is consistent with an age of $\geq$30 Myr. Thus, we cannot set age constraints on the companion, due to this discrepancy between the companion's position on evolutionary tracks.

Given its small projected separation of just $\sim$9 AU, HD 984 B will show significant orbital motion over the next few years, allowing the potential for dynamical mass determination. In order to determine the individual mass components of the HD 984 system, RV data must be obtained. Using the current projected separation as an approximation for the semi-major axis and assuming a circular orbit, we

would expect to detect a maximum semi-amplitude from RV of 1.01 km/s for an M-dwarf companion and 0.27 km/s for a brown dwarf. This calculation assumes the orbit is edge-on ($i=90°$), however based on our two epoch astrometric measurements, its orbit is unlikely to be edge-on. Even if the companion is nearly face-on ($i=1°$), the semi-amplitude of 0.018 km/s for an M-dwarf and 0.005 km/s for a brown dwarf is within the detection limits of RV. Thus, the dynamical mass of this companion can be achieved with RV measurements and will provide a crucial comparison with the theoretical evolutionary models for mass determination.

We have demonstrated that, given the difficulty in deriving a reliable age for HD 984 that is independent of its purported group membership, the derived color and spectral parameters of the companion are necessary to determine the companion mass. These results suggest that caution should be used when estimating the masses of companions based on photometric data and stellar age based on kinematic group membership alone. It reinforces the importance of future near-infrared high contrast integral field spectrographs to the characterization of low-mass stellar and substellar companions.

Acknowledgments

5.7   Appendix

We calibrated the absolute orientation of the field of view of SINFONI using observations of GQ Lup B from UT 2013 August 24 (technical program ID 60.A-9800). These observations were obtained using the pre-optics offering a 50×100 mas sampling in the $H+K$ band. During the 54 min pupil tracking (PT) sequence, 100×7s integrations were recorded. The field rotated by 12.84°. We reduced these data following the same procedure as HD 984 B. Once the cubes were corrected for atmospheric refraction, we removed the halo from the primary star centered in the field of view with a radial profile.

We found that a clockwise rotation by the *ADA.POS ANG + C* values of each data cubes re-aligned the final GQ Lup data cubes with the North. *ADA.POS ANG* is a variable found in the image header, corresponding to the position angle of the rotator at the Cassegrain focus at the time of the observations. *C* is an additional offset related to the calibration of the instrument rotator true North position.

We define *ROT.PT.OFF* + *C* = 180° + *ADA.PUPILPOS* + *C*, the angular offset needed to realign the frames to the North when the parallactic angle is 0. *ADA.PUPILPOS* is a keyword stored into the file header, which depends on the telescope pointing position and time of observation. It is redefined at the beginning of any PT sequence, but it remains constant during a PT observing sequence.

We verified that this relation remains valid for other datasets obtained in PT mode on GQ Lup during the same night, on AB Dor C (UT 2013 October 17, 60.A-9800), and on HD 984 B (UT 2014 October 10, 2014 December 3,5,8 094.C-0719), and of the astrometric binary HD 179058 AB (UT 2014 April 26, 60.A-9800). We note that we could not use the observations of the HD179058 AB to properly calibrate the instrument plate scale and absolute orientation since the binary had likely moved on its orbit since its latest independent astrometric measurement (Tokovinin et al. 2010).

For the case of GQ Lup B, the *ADA.PUPILPOS* keyword was fixed to -0.07297. Therefore, we adopted ROT.PT.OFF=179.927. We estimated a value of C=0.0 ± 0.5° comparing the resulting position angle in the derotated cubes to the position angle of the system measured from VLT/NaCo data obtained on 2012 March 3 and reported in Ginski et al. (2014). We note that this value of C assumes that the companion did not have significant orbital motion in the course of one year. This is reasonable given the available VLT/NaCo astrometry of the system recorded since 2008 (see Table 2 of Ginski et al. 2014). We also deduce from the SINFONI data of GQ Lup B that the mean square plate scale is 49.30 ± 0.14 mas/spaxel when the 50×100 mas and *H + K* band mode of the instrument are chosen.

References

Allard, F., Homeier, D., Freytag, B., et al. 2013, Memorie della Societa Astronomica Italiana Supplementi, 24, 128

Allers, K. N., & Liu, M. C. 2013, ApJ, 772, 79

Amara, A., & Quanz, S. P. 2012, MNRAS, 427, 948

Ballering, N. P., Rieke, G. H., Su, K. Y. L., & Montiel, E. 2013, ApJ, 775, 55

Baraffe, I., Chabrier, G., Barman, T. S., Allard, F., & Hauschildt, P. H. 2003, A&A, 402, 701

Biller, B. A., Liu, M. C., Wahhaj, Z., et al. 2010, ApJL, 720, L82

Bonnefoy, M., Chauvin, G., Dumas, C., et al. 2009, A&A, 506, 799

Bonnefoy, M., Lagrange, A.-M., Boccaletti, A., et al. 2011, A&A, 528, L15

Bonnefoy, M., Boccaletti, A., Lagrange, A.-M., et al. 2013, A&A, 555, A107

Bonnet, H., Abuter, R., Baker, A., et al. 2004, The Messenger, 117, 17

Brandt, T. D., McElwain, M. W., Turner, E. L., et al. 2014, ApJ, 794, 159

Bressan, A., Marigo, P., Girardi, L., et al. 2012, MNRAS, 427, 127

Brott, I., & Hauschildt, P. H. 2005, in ESA Special Publication, Vol. 576, The Three-Dimensional Universe with Gaia, ed. C. Turon, K. S. O'Flaherty, & M. A. C. Perryman, 565

Carpenter, J. M., Bouwman, J., Mamajek, E. E., et al. 2009, ApJS, 181, 197

Casagrande, L., Schönrich, R., Asplund, M., et al. 2011, A&A, 530, A138

Chabrier, G., Baraffe, I., Allard, F., & Hauschildt, P. 2000, ApJ, 542, 464

Chauvin, G., Faherty, J., Boccaletti, A., et al. 2012, A&A, 548, A33

Chauvin, G., Vigan, A., Bonnefoy, M., et al. 2015, A&A, 573, A127

Close, L. M., Thatte, N., Nielsen, E. L., et al. 2007, ApJ, 665, 736

Cutri, R. M., Skrutskie, M. F., van Dyk, S., et al. 2003, VizieR Online Data Catalog, 2246, 0

Davies, R. I. 2007, MNRAS, 375, 1099

Dupuy, T. J., & Liu, M. C. 2012, ApJS, 201, 19

Dupuy, T. J., Liu, M. C., Leggett, S. K., et al. 2015, ArXiv e-prints

Eisenhauer, F., Abuter, R., Bickert, K., et al. 2003, in Society of Photo-Optical Instrumentation Engineers (SPIE) Conference Series, Vol. 4841, Instrument Design and Performance for Optical/Infrared Ground-based Telescopes, ed. M. Iye & A. F. M. Moorwood, 1548–1561

ESA. 1997, VizieR Online Data Catalog, 1239, 0

Gagné, J., Lafrenière, D., Doyon, R., Malo, L., & Artigau, É. 2014, ApJ, 783, 121

Ginski, C., Schmidt, T. O. B., Mugrauer, M., et al. 2014, MNRAS, 444, 2280

Holmberg, J., Nordström, B., & Andersen, J. 2009, A&A, 501, 941

Houk, N., & Swift, C. 1999, Michigan catalogue of two-dimensional spectral types for the HD Stars ; vol. 5

Kasper, M., Amico, P., Pompei, E., et al. 2009, The Messenger, 137, 8

Kenworthy, M. A., Meshkat, T., Quanz, S. P., et al. 2013, ApJ, 764, 7

Kenworthy, M. A., Quanz, S. P., Meyer, M. R., et al. 2010, in Society of Photo-Optical Instrumentation Engineers (SPIE) Conference Series, Vol. 7735, Society of Photo-Optical Instrumentation Engineers (SPIE) Conference Series

Lenzen, R., Hartung, M., Brandner, W., et al. 2003, in Society of Photo-Optical Instrumentation Engineers (SPIE) Conference Series, Vol. 4841, Society of Photo-Optical Instrumentation Engineers (SPIE) Conference Series, ed. M. Iye & A. F. M. Moorwood, 944–952

Malo, L., Doyon, R., Lafrenière, D., et al. 2013, ApJ, 762, 88

Mamajek, E. E., & Hillenbrand, L. A. 2008, ApJ, 687, 1264

Mamajek, E. E., Meyer, M. R., Hinz, P. M., et al. 2004, ApJ, 612, 496

Mamajek, E. E., Bartlett, J. L., Seifahrt, A., et al. 2013, AJ, 146, 154

Marois, C., Lafrenière, D., Doyon, R., Macintosh, B., & Nadeau, D. 2006, ApJ, 641, 556

Masana, E., Jordi, C., & Ribas, I. 2006, A&A, 450, 735

Mason, B. D., Wycoff, G. L., Hartkopf, W. I., Douglass, G. G., & Worley, C. E. 2001, AJ, 122, 3466

Meshkat, T., Bailey, V. P., Su, K. Y. L., et al. 2015, ApJ, 800, 5

Meshkat, T., Kenworthy, M. A., Quanz, S. P., & Amara, A. 2014, ApJ, 780, 17

Nielsen, E. L., Liu, M. C., Wahhaj, Z., et al. 2012, ApJ, 750, 53

Pearce, T. D., Wyatt, M. C., & Kennedy, G. M. 2015, MNRAS, 448, 3679

Pecaut, M. J., & Mamajek, E. E. 2013, ApJS, 208, 9

Quanz, S. P., Meyer, M. R., Kenworthy, M. A., et al. 2010, ApJL, 722, L49

Rajpurohit, A. S., Reylé, C., Allard, F., et al. 2013, A&A, 556, A15

Rameau, J., Chauvin, G., Lagrange, A.-M., et al. 2013, A&A, 553, A60

Rayner, J. T., Cushing, M. C., & Vacca, W. D. 2009, ApJS, 185, 289

Reggiani, M., & Meyer, M. R. 2013, A&A, 553, A124

Reis, W., Corradi, W., de Avillez, M. A., & Santos, F. P. 2011, ApJ, 734, 8

Rousset, G., Lacombe, F., Puget, P., et al. 2003, in Society of Photo-Optical Instrumentation Engineers (SPIE) Conference Series, Vol. 4839, Society of Photo-Optical Instrumentation Engineers (SPIE) Conference Series, ed. P. L. Wizinowich & D. Bonaccini, 140–149

Schlegel, D. J., Finkbeiner, D. P., & Davis, M. 1998, ApJ, 500, 525

Schmidt, S. J., West, A. A., Bochanski, J. J., Hawley, S. L., & Kielty, C. 2014, PASP, 126, 642

Schröder, C., Reiners, A., & Schmitt, J. H. M. M. 2009, A&A, 493, 1099

Stephens, D. C., Leggett, S. K., Cushing, M. C., et al. 2009, ApJ, 702, 154

Takeda, G., Ford, E. B., Sills, A., et al. 2007, ApJS, 168, 297

Thackrah, A., Jones, H., & Hawkins, M. 1997, MNRAS, 284, 507

Thies, I., Pflamm-Altenburg, J., Kroupa, P., & Marks, M. 2015, ApJ, 800, 72

Tokovinin, A., Mason, B. D., & Hartkopf, W. I. 2010, AJ, 139, 743

Torres, C. A. O., Quast, G. R., Melo, C. H. F., & Sterzik, M. F. 2008, Young Nearby Loose Associations, ed. B. Reipurth, 757

Valenti, J. A., & Fischer, D. A. 2005, ApJS, 159, 141

van Leeuwen, F. 2007, A&A, 474, 653

Wahhaj, Z., Liu, M. C., Biller, B. A., et al. 2011, ApJ, 729, 139

Wright, J. T., Marcy, G. W., Butler, R. P., & Vogt, S. S. 2004, ApJS, 152, 261

Zuckerman, B., Rhee, J. H., Song, I., & Bessell, M. S. 2011, ApJ, 732, 61

Chapter 6

Searching for gas giant planets on Solar System scales - A NACO/APP *L'*-band survey of A- and F-type Main Sequence stars

We report the results of a direct imaging survey of A- and F-type main sequence stars searching for giant planets. A/F stars are often the targets of surveys, as they are thought to have more massive giant planets relative to solar-type stars. However, most imaging is only sensitive to orbital separations > 30 AU, where it has been demonstrated that giant planets are rare. In this survey, we take advantage of the high-contrast capabilities of the Apodizing Phase Plate coronagraph on NACO at the Very Large Telescope. Combined with optimized principal component analysis post-processing, we are sensitive to planetary-mass companions (2 to 12 $M_{\rm Jup}$) at Solar System scales (≤30 AU). We obtained data on 13 stars in *L'*-band and detected one new companion as part of this survey: an M6.0 ± 0.5 dwarf companion around HD 984. We re-detect low-mass companions around HD 12894 and HD 20385, both reported shortly after the completion of this survey. We use Monte Carlo simulations to determine new constraints on the low-mass (<80 $M_{\rm Jup}$) companion frequency, as a function of mass and separation. Assuming solar-type planet mass and separation distributions, normalized to the planet frequency appropriate for A-stars, and the observed companion mass-ratio distribution for stellar companions extrapolated to planetary masses, we derive a truncation radius for the planetary mass companion surface density of <80 AU at 95% confidence. Finally, we compare the performance of the APP with direct imaging for four of our targets and discuss when the sensitivity is improved.

T. Meshkat, M. A. Kenworthy, M. Reggiani, S. P. Quanz, E. E. Mamajek,
M. R. Meyer
Submitted to *Monthly Notices of the Royal Astronomical Society*

6.1   Introduction

Stellar properties are an important metric in the search for planets, as they guide the target selection for detection surveys. In particular, stellar mass and metallicity are significant quantities in determining both the formation and evolution of stars and planets (Johnson et al. 2010). Several radial velocity (RV) studies have shown that the giant planet frequency increases with stellar metallicity (Santos et al. 2004; Fischer & Valenti 2005). The giant planet population as a function of stellar mass, however, is not consistent between different planet detection techniques (Quanz et al. 2012; Clanton & Gaudi 2014; Vigan et al. 2012). While progress has been made in linking the RV and microlensing populations (Clanton & Gaudi 2014), this is a challenging problem involving the synthesis of different biases and parameter spaces covered by all the detection techniques.

Hot, gas giant planets ($> 1\ M_{\text{Jup}}$) are the only directly imaged planets thus far, due to their increased self-luminous thermal emission and decreased contrast at infrared wavelengths with the star. Planet populations derived from RV surveys are often extrapolated to larger orbital separations to analyze the frequency of giant planets in direct imaging surveys (e.g. Lafrenière et al. 2007; Biller et al. 2013).

Planet formation scenarios (Alibert et al. 2011) and simulations extrapolating RV planet populations (Crepp & Johnson 2011; Johnson et al. 2007) suggest that massive stars($>1.3 M_{\odot}$) are the most favorable targets for directly imaging planets, since they have proportionally more material to form giant planets. Indeed many directly imaged planetary mass companions have been found around A or F stars: HR8799 bcde (Marois et al. 2008, 2010), β Pic b (Lagrange et al. 2009, 2010), HD 95086 b (Rameau et al. 2013b,c), HD 106906 b (Bailey et al. 2014). The detection of the HR8799 planets was the result of the Vigan et al. (2012) International Deep Planet Survey. Most surveys, however, have yielded null results (Desidera et al. 2015; Chauvin et al. 2015; Janson et al. 2013; Rameau et al. 2013a; Biller et al. 2013; Chauvin et al. 2010; Heinze et al. 2010; Lafrenière et al. 2007; Kasper et al. 2007). These null results are likely due to the lack of contrast at small orbital separations. Typical detection limits for these surveys are 5-20 M_{Jup} for > 30 AU. Planets are rare at large orbital separations (Chauvin et al. 2010; Lafrenière et al. 2007; Nielsen & Close 2010) but at Solar System scales ($\leq$ 30 AU), stars are largely unexplored.

The main limitations for direct imaging are stellar "speckles" which can appear brighter than a companion (Hinkley et al. 2009). Coronagraphs are used in order to reach smaller angular separations around stars. They reduce the diffraction due to scattered stellar light in the telescope optics but at a cost of reduced throughput. The Apodizing Phase Plate (APP; Kenworthy et al. 2010; Quanz et al. 2010, 2013) coronagraph suppresses the diffraction in a 180° wedge around a star, increasing the chances of detecting a very close-in companion. Several studies have demonstrated the APP's capability of reaching $\leq$ 30 AU (Meshkat et al. 2015; Kenworthy et al. 2013; Quanz et al. 2011).

We aim to probe down to Solar System scales ($\leq$ 30 AU) around 13 A- and F-type main sequence stars in order to detect giant planets as well as set constraints

on the planet frequency. We use the APP coronagraph on NACO at the Very Large Telescope (VLT), the L'-band filter, and optimized Principal Component Analysis (PCA) to achieve deep sensitivity limits (2 to 10 $M_{\rm Jup}$ at $\leq$ 30 AU).

In Section 6.2 we describe our target selection process, the coronagraphic observations, our data reduction method and how we determine the sensitivity of our data. In Section 6.3 we discuss the sensitivity achieved, our new detection of an M6.0 $\pm$ 0.5 dwarf companion to HD 984, and our re-detection of companions to HD 12894 and HD 20385. We run Monte Carlo simulations to determine the probability distribution of our results, in order to compare different planet population models for A- and solar-type stars. In Section 6.4 we compare our results with other surveys searching for low-mass companions and discuss the performance of the APP coronagraph. Our conclusions are in Section 6.5.

6.2 Observations and Data Reduction

Our sample was carefully selected to derive the best possible constraints on the frequency of giant exoplanets on Solar System scales: nearby, young, and massive main sequence stars. Young planets are still warm from their contraction (Spiegel & Burrows 2012). By converting gravitational energy into luminosity, they are bright in the infrared. However, determining the age of a main-sequence star can be extremely challenging. One way to deal with this difficulty is to only select targets which are members of nearby associations with well established ages. If they are all bona-fide members of the group, we can assume the stars are of a similar age. Except for one[1], our targets are all members of nearby young moving groups or associations: β Pic Moving Group (23 $\pm$ 3 Myr; Mamajek & Bell 2014), Tuc-Hor Association (40 Myr; Kraus et al. 2014), AB Dor Association (125 $\pm$ 15 Myr; Barenfeld et al. 2013). Nearby stars allow us to search for companions at smaller physical separations. We aim to reach planet sensitivity on Solar System scales, where we expect more planets to reside (Chauvin et al. 2010; Lafrenière et al. 2007; Nielsen & Close 2010). Thus, we have selected only stars which are less than 66 pc away.

At the time of selection, most[2] of the targets were known to be single stars (Mason et al. 2011; Pourbaix et al. 2009) and not in the denser nucleus of their association. However, shortly after our survey was completed, a companion was discovered around one of our targets, HD 12894, by Biller et al. (2013) and Rameau et al. (2013a). Another target, HD 20385, was found to have a companion shortly after our data were acquired (Hartkopf et al. 2012).

6.2.1 Observations at the VLT

Data were obtained for 13 targets from 2011 to 2013 (088.C-0806(B), 089.C-0617(A) PI: Sascha Quanz) at the Very Large Telescope (VLT)/UT4 with NACO

---

[1]At the time of our observations, HD 984, was believed to be a 30 Myr member of Columba association. Based on our detection of a low-mass stellar companion to HD 984 and independent isochrone fitting, we estimate the age of HD 984 to be ~2 Gyr (Meshkat et al. *submitted*).

[2]HD 20385 was known to have a wide binary 12" away.

Target	Mass ($M_\odot$)	L' mag	Spectral type	Distance (pc)	Age (Myr)
HD 203	1.40	5.2	F3V	39.4 ± 0.6	23
HD 12894	1.39	5.5	F4V	47.8 ± 1.0	40
HD 25457	1.21	4.3	F6V	18.8 ± 0.1	125
HD 35114	1.16	6.2	F6V	8.3 ± 0.9	40
HD 20385	1.13	6.4	F6V	49.2 ± 1.5	40
HD 102647	1.9	1.9	A3Va	11.0 ± 0.1	40
HD 984	1.18	6.0	F7V	47.1 ± 1.4	2000
HD 13246	1.18	6.2	F7V	44.2 ± 0.9	40
HD 40216	1.24	6.2	F7V	54.4 ± 1.3	40
HD 30051	1.38	6.0	F2/3IV/V	63.6 ± 4.2	40
HD 25953	1.16	6.6	F5	55.2 ± 2.9	125
HD 96819	2.09	5.2	A1V	55.6 ± 1.7	23
HD 123058	1.30	6.7	F4V	64.1 ± 3.5	40

Distances are extracted from parallaxes in the Hipparcos catalog (van Leeuwen 2007). The L'-band mag is converted from K-band mag in the 2MASS survey (Cutri et al. 2003) to using Cox (2000). The masses are from Casagrande et al. (2011) and Chen et al. (2014). All ages are taken from Mamajek & Bell (2014); Kraus et al. (2014); Luhman et al. (2005); Barenfeld et al. (2013) except for HD 984 which we compute in Meshkat et al. *submitted*. The bottom six targets were only observed in one APP hemisphere.

Table 6.1 Overview of stellar values used for each target.

(Lenzen et al. 2003; Rousset et al. 2003) and the APP coronagraph (Kenworthy et al. 2010). The variation in the observing time for each target depends on the observing conditions on the night; if the observing conditions fell below a threshold during the night, the data acquisition was cancelled. Data were obtained with the L27 camera, in the L'-band filter ($\lambda = 3.80\mu m$ and $\Delta\lambda = 0.62\mu m$) and the NB 4.05 filter ($\lambda = 4.051\mu m$ and $\Delta\lambda = 0.02\mu m$) depending on the star's L'-band magnitude. The visible wavefront sensor was used with each target star as its own natural guide star. We observed in pupil tracking mode to perform Angular Differential Imaging (ADI; Marois et al. 2006). We intentionally saturated the point spread function (PSF) core (on average out to ~0$''$08) to increase the signal-to-noise (S/N) from potential companions in each exposure. Unsaturated data were also obtained to calibrate photometry relative to the central star.

The APP generates a dark D-shaped wedge on one half of a target. Excess scattered light is increased on the other side of the target, which is not used in the data analysis. Two datasets were obtained with different initial position angles (P.A.) for full 360° coverage around the target star. Data were obtained in cube mode. Table 6.1 lists the stellar properties for each of our targets. Table 6.2 lists the observing conditions for all the data obtained. 13 targets were observed in at least one APP hemisphere.

6.2.2   Data Reduction

A dither pattern on the detector was used to subtract sky background and detector systematics from the raw data, as detailed in Kenworthy et al. (2013). Subtracted data cubes are centroided and averaged over. The two APP hemispheres obtained for each target must be processed separately, since they were observed on different nights and thus have different speckle noise patterns. Optimized PCA was run on both of the APP hemispheres independently for each target, following Meshkat

Target	Observation dates UT (Hem 1, Hem 2)	Number of data cubes	Total integration time (s)	On-sky rotation (°)	Average DIMM seeing (")
HD 203	2011 Oct 12, 2011 Nov 07	154, 64	4605.3, 3480.75	46.65, 60.43	0.90,1.19
HD 12894	2011 Dec 10, 2011 Dec 24	65, 55	3333, 2828	31.97, 27.92	0.78,1.23
HD 25457	2011 Dec 11, 2011 Dec 21	71, 65	2606.4, 2389.2	28.63, 25.92	1.44,0.65
HD 35114	2011 Dec 13, 2012 Jan 02	35, 35	1818, 1818	31.98, 28.20	0.75,1.02
HD 20385	2011 Dec 21, 2012 Jan 08	47, 35	2424, 1818	30.54, 24.61	1.82,1.25
HD 102647	2012 Jun 01, 2013 Apr 26	47, 56	2839.2, 3371.6	20.34, 24.71	1.61, 0.76
HD 984	2012 Jul 18, 2012 Jul 20	59, 65	3267, 3593.7	47.41,42.46	0.65, 0.86
HD 13246	2011 Dec 07, −	107, −	5454, −	45.43, −	0.99, −
HD 40216	2012 Jan 03, −	11, −	606, −	11.74, −	0.88, −
HD 30051	2012 Jan 07, −	56, −	2878.5, −	2.7, −	1.68, −
HD 25953	2012 Jan 13, −	79, −	4040, −	42.76, −	0.77, −
HD 96819	2012 May 02, −	49, −	2835, −	105.46, −	0.64, −
HD 123058	2012 May 21, −	62, −	3811.5, −	29.44, −	0.77, −

Data are in chronological order based on first Hemisphere observed. The last six targets were only observed in one APP hemisphere. Targets are listed in the same order as Table 6.1.

Table 6.2 Observing Log for NACO/VLT 088.C-0806(B) and 089.C-0617(A)

et al. (2014). This involves creating a linear combination of principal components (PCs) from the data itself in order to model and subtract away the stellar diffraction. Only the 180° D-shaped dark hemisphere was used in the PCA analysis. We fixed the number of PCs at approximately 10% the number of input frames, as this yields the optimal PSF subtraction close ($< 1\rlap{.}''0$) to the star. We searched for point sources using this method for all 13 of our targets, despite not having full 360° coverage for 6 of them.

We injected fake planets into our data (before PCA processing) in order to determine the 5σ sensitivity limit for each target. Unsaturated data of the star was used to inject the fake planets. We scaled the unsaturated data to the same exposure as the saturated data. The star was added to the data with a contrast of 5 to 12 mag in steps of 1 mag and from $0\rlap{.}''18$ to $1\rlap{.}''36$ in steps of 0.13. The outer radius limit was chosen because the field-of-view (FOV) of the APP is limited to only the upper quarter of the detector (Kenworthy et al. 2010). The planet injected data was processed with PCA, de-rotated, and averaged over for the final image with North facing up.

The final image was smoothed by a λ/D aperture, in order to remove features which are not the expected planet size or shape (Amara & Quanz 2012; Bailey et al. 2013). We define the S/N of the injected planet to be the value of a single pixel at the location of the planet divided by the root mean square (rms) of a ring around the star at the angular separation of the planet, excluding the planet itself. Only the statistically independent pixels (one smoothing kernel apart) were used
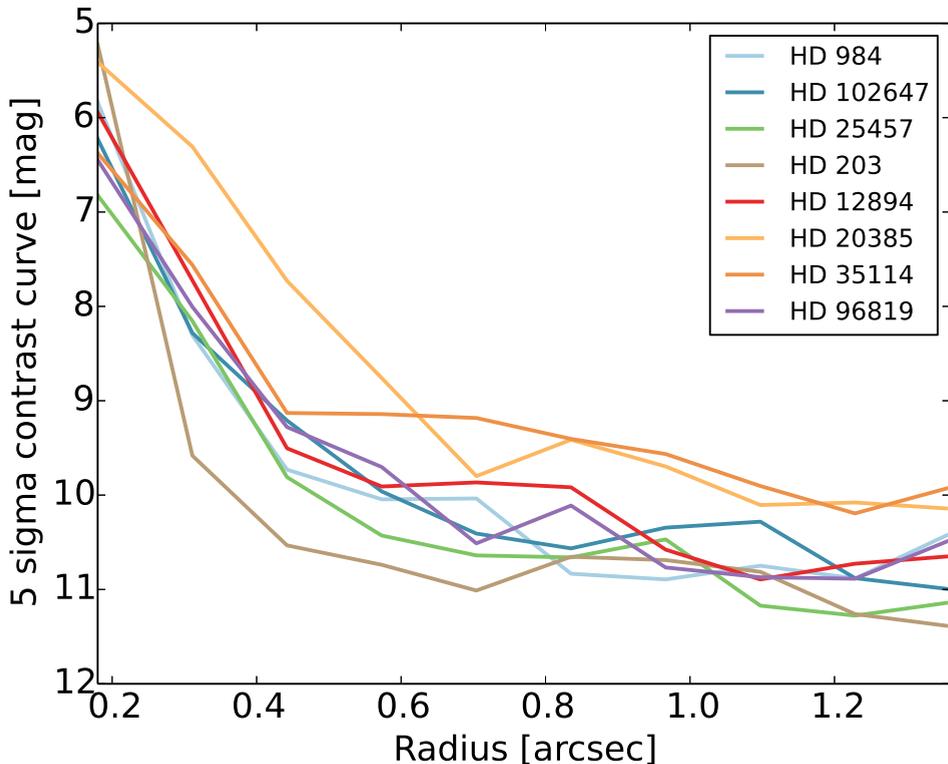
Figure 6.1 5σ contrast curves for the targets with full 360° APP coverage around the star and one target, HD 96819, with nearly 360° coverage.

to compute the rms. Figure 6.1 shows the 5σ contrast curves for all 7 targets with two APP hemispheres and one target (HD 96819) with nearly full sky coverage in one APP hemisphere[3]. For targets with two APP hemispheres, fake planets were added at a fixed P.A. in each hemisphere. The average S/N of the injected fake planets in each hemisphere is used (at the same separation). In the overlapping region between the two hemispheres, the number of frames varies slightly. However, since these regions are small and the number of frames never varies by more than 20%, the impact on the contrast curves is small.

On average, we achieved a contrast of 9 mag at 0.''4 and 10 to 11 mag at > 0.''6. The decreased sensitivity at < 0.''7 around HD 20385 is an outlier compared to the other targets. One possible explanation is the extremely bright companion detected at ∼ 0.''8 (discussed in Section 6.3.2), which affects the PCA component determination.

We used the COND evolutionary tracks (Baraffe et al. 2003) to convert the contrast curves to planet mass detection limits (Figure 6.2). For all but one of

---

[3]HD 96819 has on sky rotation of 105.°46. Since we are in ADI mode, the 180° APP "dark hole" region rotates on the sky and only a ∼ 74.°9 wedge is missing.
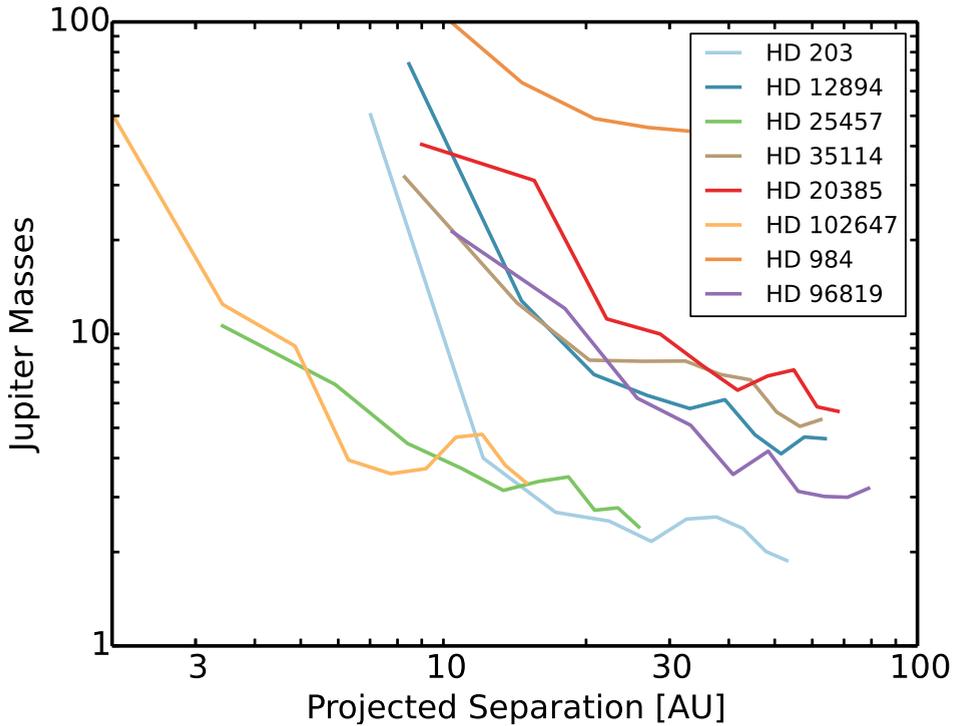
Figure 6.2 Detection limits in Jupiter masses versus projected separation in AU for all targets with full APP coverage (and HD 96819). We are sensitive to planet mass companions ($< 12M_{\text{Jup}}$) for all of our targets, except HD 984 which we demonstrate is much older than previously suggested (Meshkat et al. *submitted*). HD 102647 is more sensitive at smaller projected separation because it is much closer than the rest of the targets (11 pc). We do not plot the sensitivity beyond 1″5 for each target, due to the limited FOV of the APP.

Target	Date	Separation (arcsec)	P.A. (deg)	$\Delta L'$ (mag))	Mass ($M_\odot$)
HD12894 B	2011 Nov 24	0.31 ± 0.01	240.24 ± 1.36	2.89 ± 0.14	0.49 ± 0.04
HD20385 B	2011 Dec 21	0.87 ± 0.01	118.67 ± 0.7	2.52 ± 0.10	0.43 ± 0.03
HD984 B	2012 July 18	0.19 ± 0.02	108.9 ± 3.1	6.0 ± 0.2	0.11 ± 0.01

Table 6.3 Companion properties of our targets.

our targets[4], we were sensitive to planetary mass objects ($< 12\,M_{\rm Jup}$) at different projected separations, depending on the target distance. The outer radius for the sensitivity curves is based on the limited FOV of the APP (Kenworthy et al. 2010). Thus, while the sensitivity curves appear to flatten out, we cannot extend these curves beyond 1.′′5 since we were not sensitive completely around the star.

6.3   Results

We detect one new M6.0 ± 0.5 dwarf companion to HD 984, and re-detect companions to HD 12894 and HD 20385. To estimate the astrometry, we first determine the centroid of the three companions. In this way, we verify that our star was well centered in our data. Since the APP has an asymmetric PSF, this step is crucial. We then injected fake negative companions at the location of the companion to determine the photometry and astrometry with error bars. We also varied the flux of the fake negative companions to cancel out the companion flux, which in some cases varies up to 20% due to atmospheric fluctuations.

We iteratively converged on the P.A., angular separation, and Δ magnitude by varying the position and contrast and taking a χ^2 minimization over the λ/D aperture at the location of the companion. For the very bright companions to HD 12894 and HD 20385, we determined the photometry and astrometry from ADI alone rather than PCA. Minor variations in the brightness and position of the companion in each frame can lead to "striping" in the final PCA processed image. This striping occurs when PCA fits the remaining flux around of the companion after the fake companion is subtracted, since we never perfectly subtract the companion in individual frames due to seeing variability. Table 6.3 lists the properties of the companions we detect based on our APP data. The error on the P.A. includes uncertainties from true North orientation, based on direct imaging observations ($\sim 0.5°$, Rameau et al. 2013a).

6.3.1   HD 12894

Rameau et al. (2013a) and Biller et al. (2013) reported the discovery of HD 12894 B. Rameau et al. (2013a) detected a $\Delta L' = 2.7 \pm 0.1$ mag point source 14 AU from the star. They concluded that it was likely bound to the star, based on a non-detection in 1999 2MASS data, because a background source would be detected due to proper motion of HD 12894. Based on the contrast and an age of 30 Myr, they concluded that the companion was a $0.8 M_\odot$ K6 star. Biller et al. (2013)

---

[4]We were not sensitive to planet masses around HD 984, since it is much older than previously reported (Meshkat et al. *submitted*).
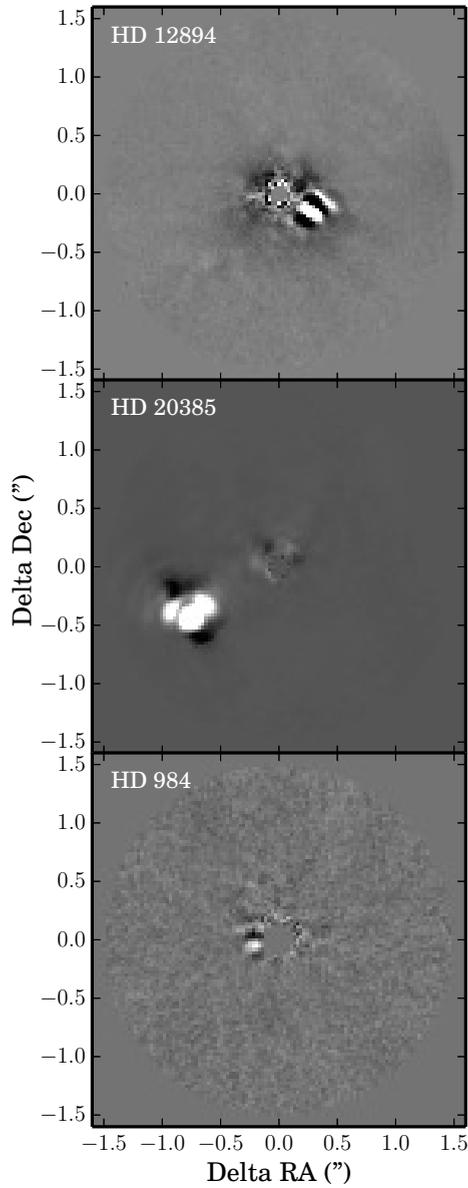
Figure 6.3 Top: HD 12894 ADI processed image, with the companion at $0\rlap{.}''31$. Middle: HD 20385 ADI processed image, with the companion at $0\rlap{.}''87$. The shape of the companion PSF is due to the APP PSF. Bottom: HD 984 PCA processed image with the companion $0\rlap{.}''192$ from star.

concluded it was a co-moving $0.46 \pm 0.08\ M_\odot$ companion 15.7 ± 1.0 AU away from its star, based on contrast of $\Delta H = 3.0$ mag. The discovery was made with the VLT/NACO instrument in L'-band as well as the NICI instrument on Gemini South in H-band, respectively.

At the time our data were acquired, the companion was not known. We detect the companion with a $\Delta L' = 2.89 \pm 0.14$ mag at a PA of $240.24 \pm 1°27$ and separation of $0''31 \pm 0''01$. This corresponds to a projected separation of 14.8 ± 0.8 AU, with d$=47.8 \pm 1.0$ pc for the distance to the star (van Leeuwen 2007). Figure 6.3 shows the ADI processed image of the companion. Using the COND evolutionary models (Baraffe et al. 2003) and the age of the star (40 Myr: Kraus et al. 2014), we estimate the mass of the companion is $0.49 \pm 0.04\ M_\odot$. Our analysis of this companion is consistent with Biller et al. (2013).

6.3.2   HD 20385

At the time we proposed to observe this target, it was a known wide binary, with a companion TOK 78 B 12" away. Hartkopf et al. (2012) reported the discovery of a new, close companion around HD 20385 at $0''88$, $\Delta I =3.5$ mag, $\Delta y = 5.2$ mag. They estimated the companion has a period of 200 years. Due to its variable radial velocity, they suggested the companion could be two unresolved companions.

We detect the companion in our data at $0''87 \pm 0''01$ with a P.A. of $118°67 \pm 0°49$ and contrast of $\Delta L' = 2.52 \pm 0.10$ mag. Using the stellar distance of 49.2 ± 1.5 pc (van Leeuwen 2007), this companion is at a projected separation of 42.8 ± 1.8 AU. Figure 6.3 shows the ADI processed image of the companion to HD 20385. The companion's PSF clearly shows the APP PSF structure, with the bright lobes smeared due to the rotation on the sky. The age of the system is 40 Myr based on membership in the Tuc-Hor Association (Kraus et al. 2014). Using COND models (Baraffe et al. 2003), we estimate the companion to have a mass of $0.33 \pm 0.03\ M_\odot$.

6.3.3   HD 984

As reported in Meshkat et al. (*submitted*), we detected a companion around HD 984 in our APP data, as well as in archival direct imaging data. Figure 6.3 shows our PCA reduced image with 20 PCs. We confirmed the companion is co-moving with HD 984 and determined that is an M6.0 $\pm$ 0.5 dwarf based on SINFONI integral field spectroscopy (see Table 6.3).

6.3.4   Monte Carlo Simulations

We ran 10000 Monte Carlo simulations of the target stars in order to determine the probability distribution of detecting substellar companions in our data assuming power-law slopes for the mass and semi-major axis distributions, for both planets and brown dwarfs (BDs), following Reggiani et al. *submitted*. For the BD distribution, we adopted the stellar companion mass ratio distribution (CMRD) from Reggiani & Meyer (2013) and a log-normal separation distribution (De Rosa et al. 2014). We included all of our targets in these simulations, including those with
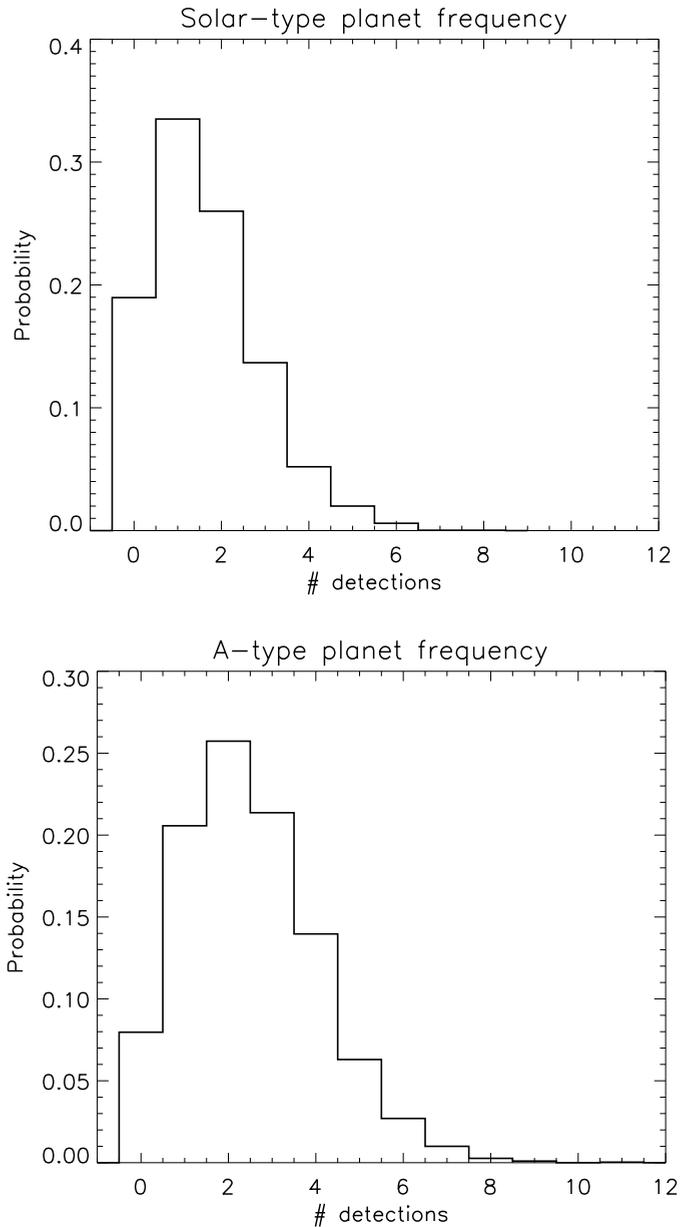
Figure 6.4 Detection probability distributions for our survey, assuming an outer-radius cutoff of 80 AU for the planet separation distributions (Reggiani et al., *submitted*). We run the simulations for both solar-type stars and A-stars. With our null result, we rule out the A-star frequency beyond a cutoff of 100 AU at the 95% confidence level. (Top: solar-type stars, Bottom: A-type stars).

only one APP hemisphere coverage. In order to account for the targets without full sky coverage in our simulations, we multiplied the overall planet frequency per target by the fraction of sky coverage achieved.

For the planets, we adopted two different model distributions. The first one assumes the planet frequency, mass and separation distributions measured by RV surveys for solar-type stars, and extrapolated at larger separations (Heinze et al. 2010, based on Cumming et al. 2008). According to Cumming et al. (2008), the planet mass and semi-major axis distributions are modeled with power laws of index α=-1.31 and β=-0.61 ($dN \sim M^{-1.31}dM$ and $dN \sim a^{-0.61}da$). This results in a planet frequency of f=0.0329 for planets in the range 1-13 M_{Jup} and 0.3-2.5 AU. The second model, more appropriate for A-type primaries, consists of the same planet mass and separation distribution measured for Sun-like stars, but adopts the values corresponding to the median sensitivity achieved in the RV data presented in Bowler et al. (2010) and Johnson et al. (2010) (f=11 ± 2% for planets in the ranges 0.5-14 M_{Jup} and 0.1-3.0 AU).

For both planets and BDs, we assume a random distribution of inclinations and the eccentricity distribution given by Jurić & Tremaine (2008). In each simulation, we assigned each target a number of planets and BDs from a Poisson distribution, according to the average number of planets and BDs per star, calculated from the aforementioned distributions. As this is given by the BD and planet mass and separation probability distributions, it is different in the two models for the planet population. We also varied the outer radius cutoff: 20, 30, 80, and 100 AU. The introduction of an upper limit for the planet separation distribution has been suggested by the results of previous direct imaging surveys (Chauvin et al. 2010; Vigan et al. 2012).

If a target turns out to have one or more companions in the simulation, we assigned each companion a mass and the orbital parameters (semi-major axis, eccentricity, inclination) randomly drawn from the assumed distributions. The mass is converted into apparent magnitude, given the distance and age of the star and assuming the same family of evolutionary models as in Section 6.2.2 (COND Baraffe et al. 2003). The semi-major axis was converted into a projected separation, given the eccentricity and inclination and taking into account the time spent on the orbit. If the combination of brightness and separation lies above the contrast curve (Figure 6.1), then the companion is detectable. Thus, at the end of every simulation, we know how many companions are created and how many are detected. After 10000 simulations, we determined the average detection probability for our A and F main sequence star survey (Figure 6.4). Three companions were detected in this survey, but none of them were sub-stellar (<80 M_{Jup}). Thus, the probability of detecting 0 companions for each model is given in Table 6.4.

Given these probabilities, our null result allows us to reject the A-type star model with a scaled up planet frequency for $r_{cutoff} > 100$ AU, with more than 95% confidence. This null result is also consistent with previous surveys that found that high mass planets at large orbital separations are rare (Nielsen et al. 2013; Biller et al. 2013; Desidera et al. 2015; Chauvin et al. 2015), noting that our simulations include both the planetary-mass companions as well as extrapolation of the BD companion mass ratio distribution. Based on RV measurements of A

r_{cutoff}	P(0) [%] sun-like star planet frequency	P(0) [%] A-type star planet frequency
20 AU	57	51
30 AU	49	39
80 AU	15	5
100 AU	10	3

Table 6.4 Probability of a null result in our A and F main sequence star survey.

stars, Bowler et al. (2010) suggest positive values for the power law indexes of the mass and separation distributions, with high confidence. According to our Monte Carlo simulations, if we assume positive power law indexes, the probability of a null result is less than 0.1%, regardless of the planet frequency or the radius cutoff assumed. As suggested by Vigan et al. (2012), the inconsistency of direct imaging survey results with the distribution parameters from RV observations around A-stars (Bowler et al. 2010) suggests that different planet populations are probed by RV measurements at small separations than direct imaging at wide separations.

6.4 Comparison of the APP and Direct Imaging

There have been several other surveys focused on searching for planets around A stars (SEEDS: Janson et al. 2013; Brandt et al. 2014, NICI: Biller et al. 2013; Nielsen et al. 2013; Wahhaj et al. 2013, IDPS: Vigan et al. 2012, NACO Large Survey: Desidera et al. 2015; Chauvin et al. 2015, L'-band NACO: Rameau et al. 2013a). Our results are most comparable to Rameau et al. (2013a) since data were taken in L'-band. These surveys have detected low-mass stellar companions (Rameau et al. 2013a; Vigan et al. 2012), and brown dwarfs (Nielsen et al. 2013; Brandt et al. 2014). Our survey of only 13 targets yielded three low-mass companions. The dark 180° hole due to the APP is expected to increase sensitivity over direct imaging from 0.″2 to 0.″7. Without non-coronagraphic data of all of these targets, it is challenging to determine which benefited from the APP. However, four of our targets were also directly imaged in L'-band by Rameau et al. (2013a), allowing direct comparison of the sensitivity (Figure 6.5). We accessed the archival raw direct imaging data, processed it with PCA and follow the strategy detailed in Section 6.2.2 to ensure the data are reduced identically to the APP data.

These data are not ideal for comparison as they have different integration times, field rotation, and airmass. However, we compare the contrast curves for the two datasets for each target (Figure 6.5). HD 12894 and HD 102647 show increased sensitivity due to the APP. These targets show the expected decrease in sensitivity around 0.″8, where the PSF matches direct imaging (the "outside" of the dark hole). Beyond this angular separation, direct imaging performs slightly better than the APP, as expected (Kenworthy et al. 2010). The HD 984 contrast curves are nearly identical for direct imaging and the APP. Direct imaging performs better for HD 25457. This target does not achieve an increase in sensitivity from the APP at smaller radii, as was expected.
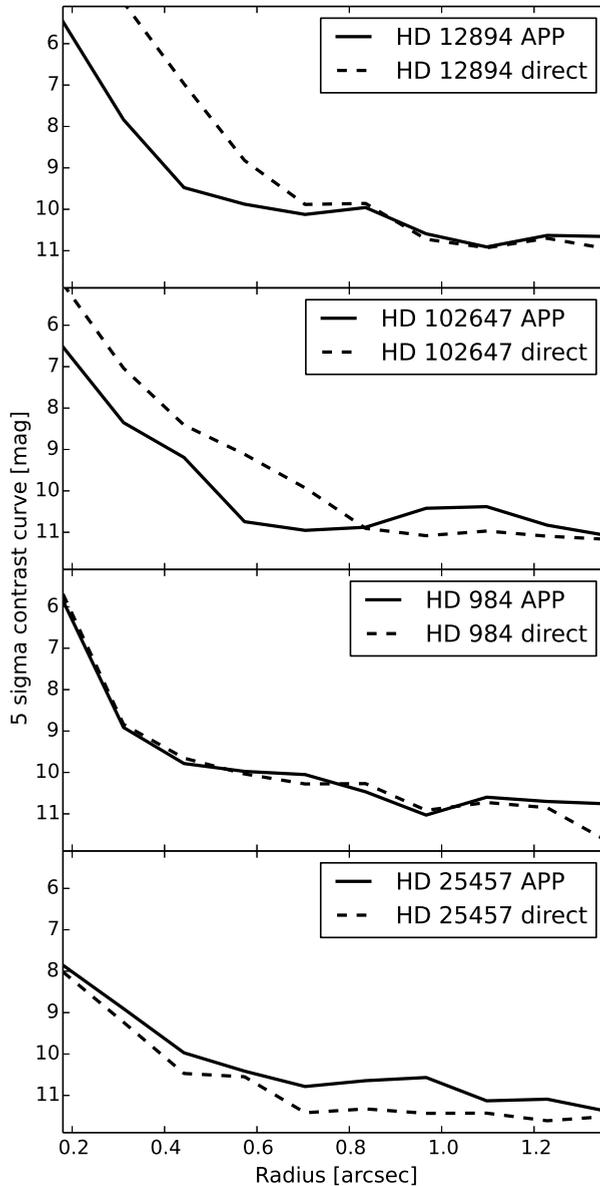
Figure 6.5 5σ contrast curves for the four targets which overlap with the direct imaging targets in Rameau et al. (2013a). HD 12894 and HD 102647 benefited from the use of the APP over direct imaging, seen by the "bump" in the contrast curve at $\sim 0\rlap{.}''7$. The bump shows that the APP suppressed diffraction more effectively than direct imaging would have under similar conditions. The curves are scaled so each target is the same integration time.

It is challenging to draw conclusions from these four datasets alone, as the rotation angle, seeing conditions, and integration times are not identical. However, in two of the four cases, the APP is more sensitive than direct imaging at small angular separations. At best, the APP provides 1-2 mag increased sensitivity from $0\rlap{.}''2$ to $0\rlap{.}''8$. Achieving better detection limits at smaller inner working angles is necessary to reach closer-in planets (Chauvin et al. 2010; Lafrenière et al. 2007; Nielsen & Close 2010). The APP, like all coronagraphs, is condition sensitive. These results suggest that a larger sample size with controlled data conditions should be performed to assess when the APP coronagraph outperforms direct imaging.

6.5   Conclusion

We present the results from a survey of carefully selected A- and F-type main sequence stars, searching for exoplanet companions. We aim to put direct imaging constraints on the occurrence of sub-stellar companions as a function of stellar mass. We obtained data on thirteen nearby (d<65 pc), young (<125 Myr) targets with the APP coronagraph on NACO/VLT. We are sensitive to planet masses (2 to 10 $M_{\rm Jup}$) on Solar System scales ($\leq$30 AU) for all but one of our targets. We detected a new M6.0 ± 0.5 dwarf companion to HD 984 and confirm stellar companions to HD 12894 and HD 20385, discovered shortly after our survey data were acquired. Our photometry and astrometry for these companions are consistent with the values reported at the time of their discovery (Biller et al. 2013; Hartkopf et al. 2012). We found zero false positives in our L'-band data, as all of our detected point sources were bona-fide companions. We perform Monte Carlo simulations to determine the expected probability of detecting low-mass companions in our survey, based on our sensitivity and assumed semi-major axis distributions. Our non-detection of substellar companions ($< 80\,M_{\rm Jup}$) allows us to rule out the A-star frequency model distribution for >100 AU, with 95% confidence. We compare our APP coronagraphic data sensitivity with archival non-coronagraphic data for four targets and comment on when the performance is improved. We suggest a dedicated comparison survey is necessary to determine the appropriate targets and observing conditions when the APP coronagraph will consistently outperform direct imaging.

Acknowledgments

References

Alibert Y., Mordasini C., Benz W., 2011, A&A, 526, A63

Amara A., Quanz S. P., 2012, MNRAS, 427, 948

Bailey V., Hinz P. M., Currie T., Su K. Y. L., Esposito S., Hill J. M., Hoffmann W. F., Jones T., Kim J., Leisenring J., Meyer M., Murray-Clay R., Nelson M. J., Pinna E., Puglisi A., Rieke G., Rodigas T., Skemer A., Skrutskie M. F., Vaitheeswaran V., Wilson J. C., 2013, ApJ, 767, 31

Bailey V., Meshkat T., Reiter M., Morzinski K., Males J., Su K. Y. L., Hinz P. M., Kenworthy M., Stark D., Mamajek E., Briguglio R., Close L. M., Follette K. B., Puglisi A., Rodigas T., Weinberger A. J., Xompero M., 2014, ApJL, 780, L4

Baraffe I., Chabrier G., Barman T. S., Allard F., Hauschildt P. H., 2003, A&A, 402, 701

Barenfeld S. A., Bubar E. J., Mamajek E. E., Young P. A., 2013, ApJ, 766, 6

Biller B. A., Liu M. C., Wahhaj Z., Nielsen E. L., Hayward T. L., Males J. R., Skemer A., Close L. M., Chun M., Ftaclas C., Clarke F., Thatte N., Shkolnik E. L., Reid I. N., Hartung M., Boss A., Lin D., Alencar S. H. P., de Gouveia Dal Pino E., Gregorio-Hetem J., Toomey D., 2013, ApJ, 777, 160

Bowler B. P., Johnson J. A., Marcy G. W., Henry G. W., Peek K. M. G., Fischer D. A., Clubb K. I., Liu M. C., Reffert S., Schwab C., Lowe T. B., 2010, ApJ, 709, 396

Brandt T. D., McElwain M. W., Turner E. L., Mede K., Spiegel D. S., Kuzuhara M., Schlieder J. E., Wisniewski J. P., Abe L., Biller B., Brandner W., Carson J., Currie T., Egner S., Feldt M., Golota T., Goto M., Grady C. A., Guyon O., Hashimoto J., Hayano Y., Hayashi M., Hayashi S., Henning T., Hodapp K. W., Inutsuka S., Ishii M., Iye M., Janson M., Kandori R., Knapp G. R., Kudo T., Kusakabe N., Kwon J., Matsuo T., Miyama S., Morino J.-I., Moro-Martín A., Nishimura T., Pyo T.-S., Serabyn E., Suto H., Suzuki R., Takami M., Takato N., Terada H., Thalmann C., Tomono D., Watanabe M., Yamada T., Takami H., Usuda T., Tamura M., 2014, ApJ, 794, 159

Casagrande L., Schönrich R., Asplund M., Cassisi S., Ramírez I., Meléndez J., Bensby T., Feltzing S., 2011, A&A, 530, A138

Chauvin G., Lagrange A.-M., Bonavita M., Zuckerman B., Dumas C., Bessell M. S., Beuzit J.-L., Bonnefoy M., Desidera S., Farihi J., Lowrance P., Mouillet D., Song I., 2010, A&A, 509, A52

Chauvin G., Vigan A., Bonnefoy M., Desidera S., Bonavita M., Mesa D., Boccaletti A., Buenzli E., Carson J., Delorme P., Hagelberg J., Montagnier G., Mordasini C., Quanz S. P., Segransan D., Thalmann C., Beuzit J.-L., Biller B., Covino E., Feldt M., Girard J., Gratton R., Henning T., Kasper M., Lagrange A.-M., Messina S., Meyer M., Mouillet D., Moutou C., Reggiani M., Schlieder J. E., Zurlo A., 2015, A&A, 573, A127

Chen C. H., Mittal T., Kuchner M., Forrest W. J., Lisse C. M., Manoj P., Sargent B. A., Watson D. M., 2014, ApJS, 211, 25

Clanton C., Gaudi B. S., 2014, ApJ, 791, 90

Cox A. N., 2000, Allen's astrophysical quantities

Crepp J. R., Johnson J. A., 2011, ApJ, 733, 126

Cumming A., Butler R. P., Marcy G. W., Vogt S. S., Wright J. T., Fischer D. A., 2008, PASP, 120, 531

Cutri R. M., Skrutskie M. F., van Dyk S., Beichman C. A., Carpenter J. M., Chester T., Cambresy L., Evans T., Fowler J., Gizis J., Howard E., Huchra J., Jarrett T., Kopan E. L., Kirkpatrick J. D., Light R. M., Marsh K. A., McCallon H., Schneider S., Stiening R., Sykes M., Weinberg M., Wheaton W. A., Wheelock S., Zacarias N., 2003, VizieR Online Data Catalog, 2246, 0

De Rosa R. J., Patience J., Wilson P. A., Schneider A., Wiktorowicz S. J., Vigan A., Marois C., Song I., Macintosh B., Graham J. R., Doyon R., Bessell M. S., Thomas S., Lai O., 2014, MNRAS, 437, 1216

Desidera S., Covino E., Messina S., Carson J., Hagelberg J., Schlieder J. E., Biazzo K., Alcalá J. M., Chauvin G., Vigan A., Beuzit J. L., Bonavita M., Bonnefoy M., Delorme P., D'Orazi V., Esposito M., Feldt M., Girardi L., Gratton R., Henning T., Lagrange A. M., Lanzafame A. C., Launhardt R., Marmier M., Melo C., Meyer M., Mouillet D., Moutou C., Segransan D., Udry S., Zaidi C. M., 2015, A&A, 573, A126

Fischer D. A., Valenti J., 2005, ApJ, 622, 1102

Hartkopf W. I., Tokovinin A., Mason B. D., 2012, AJ, 143, 42

Heinze A. N., Hinz P. M., Sivanandam S., Kenworthy M., Meyer M., Miller D., 2010, ApJ, 714, 1551

Hinkley S., Oppenheimer B. R., Soummer R., Brenner D., Graham J. R., Perrin M. D., Sivaramakrishnan A., Lloyd J. P., Roberts Jr. L. C., Kuhn J., 2009, ApJ, 701, 804

Janson M., Brandt T. D., Moro-Martín A., Usuda T., Thalmann C., Carson J. C., Goto M., Currie T., McElwain M. W., Itoh Y., Fukagawa M., Crepp J., Kuzuhara M., Hashimoto J., Kudo T., Kusakabe N., Abe L., Brandner W., Egner S., Feldt M., Grady C. A., Guyon O., Hayano Y., Hayashi M., Hayashi S., Henning T., Hodapp K. W., Ishii M., Iye M., Kandori R., Knapp G. R., Kwon J., Matsuo T., Miyama S., Morino J.-I., Nishimura T., Pyo T.-S., Serabyn E., Suenaga T., Suto H., Suzuki R., Takahashi Y., Takami M., Takato N., Terada H., Tomono D., Turner E. L., Watanabe M., Wisniewski J., Yamada T., Takami H., Tamura M., 2013, ApJ, 773, 73

Johnson J. A., Aller K. M., Howard A. W., Crepp J. R., 2010, PASP, 122, 905

Johnson J. A., Butler R. P., Marcy G. W., Fischer D. A., Vogt S. S., Wright J. T., Peek K. M. G., 2007, ApJ, 670, 833

Jurić M., Tremaine S., 2008, ApJ, 686, 603

Kasper M., Apai D., Janson M., Brandner W., 2007, A&A, 472, 321

Kenworthy M., Quanz S., Meyer M., Kasper M., Girard J., Lenzen R., Codona J., Hinz P., 2010, The Messenger, 141, 2

Kenworthy M. A., Meshkat T., Quanz S. P., Girard J. H., Meyer M. R., Kasper M., 2013, ApJ, 764, 7

Kraus A. L., Shkolnik E. L., Allers K. N., Liu M. C., 2014, AJ, 147, 146

Lafrenière D., Doyon R., Marois C., Nadeau D., Oppenheimer B. R., Roche P. F., Rigaut F., Graham J. R., Jayawardhana R., Johnstone D., Kalas P. G., Macintosh B., Racine R., 2007, ApJ, 670, 1367

Lagrange A.-M., Bonnefoy M., Chauvin G., Apai D., Ehrenreich D., Boccaletti A., Gratadour D., Rouan D., Mouillet D., Lacour S., Kasper M., 2010, Science, 329, 57

Lagrange A.-M., Gratadour D., Chauvin G., Fusco T., Ehrenreich D., Mouillet D., Rousset G., Rouan D., Allard F., Gendron É., Charton J., Mugnier L., Rabou P., Montri J., Lacombe F., 2009, A&A, 493, L21

Lenzen R., Hartung M., Brandner W., Finger G., Hubin N. N., Lacombe F., Lagrange A.-M., Lehnert M. D., Moorwood A. F. M., Mouillet D., 2003, in Society of Photo-Optical Instrumentation Engineers (SPIE) Conference Series, Vol. 4841, Society of Photo-Optical Instrumentation Engineers (SPIE) Conference Series, Iye M., Moorwood A. F. M., eds., pp. 944–952

Luhman K. L., Stauffer J. R., Mamajek E. E., 2005, ApJL, 628, L69

Mamajek E. E., Bell C. P. M., 2014, MNRAS, 445, 2169

Marois C., Lafrenière D., Doyon R., Macintosh B., Nadeau D., 2006, ApJ, 641, 556

Marois C., Macintosh B., Barman T., Zuckerman B., Song I., Patience J., Lafrenière D., Doyon R., 2008, Science, 322, 1348

Marois C., Macintosh B., Véran J.-P., 2010, in Society of Photo-Optical Instrumentation Engineers (SPIE) Conference Series, Vol. 7736, Society of Photo-Optical Instrumentation Engineers (SPIE) Conference Series

Mason B. D., Wycoff G. L., Hartkopf W. I., Douglass G. G., Worley C. E., 2011, VizieR Online Data Catalog, 1, 2026

Meshkat T., Bailey V. P., Su K. Y. L., Kenworthy M. A., Mamajek E. E., Hinz P. M., Smith P. S., 2015, ApJ, 800, 5

Meshkat T., Kenworthy M. A., Quanz S. P., Amara A., 2014, ApJ, 780, 17

Nielsen E. L., Close L. M., 2010, ApJ, 717, 878

Nielsen E. L., Liu M. C., Wahhaj Z., Biller B. A., Hayward T. L., Close L. M., Males J. R., Skemer A. J., Chun M., Ftaclas C., Alencar S. H. P., Artymowicz P., Boss A., Clarke F., de Gouveia Dal Pino E., Gregorio-Hetem J., Hartung M., Ida S., Kuchner M., Lin D. N. C., Reid I. N., Shkolnik E. L., Tecza M., Thatte N., Toomey D. W., 2013, ApJ, 776, 4

Pourbaix D., Tokovinin A. A., Batten A. H., Fekel F. C., Hartkopf W. I., Levato H., Morell N. I., Torres G., Udry S., 2009, VizieR Online Data Catalog, 1, 2020

Quanz S. P., Amara A., Meyer M. R., Kenworthy M. A., Kasper M., Girard J. H., 2013, ApJL, 766, L1

Quanz S. P., Lafrenière D., Meyer M. R., Reggiani M. M., Buenzli E., 2012, A&A, 541, A133

Quanz S. P., Meyer M. R., Kenworthy M. A., Girard J. H. V., Kasper M., Lagrange A.-M., Apai D., Boccaletti A., Bonnefoy M., Chauvin G., Hinz P. M., Lenzen R., 2010, ApJL, 722, L49

Quanz S. P., Schmid H. M., Geissler K., Meyer M. R., Henning T., Brandner W., Wolf S., 2011, ApJ, 738, 23

Rameau J., Chauvin G., Lagrange A.-M., Boccaletti A., Quanz S. P., Bonnefoy M., Girard J. H., Delorme P., Desidera S., Klahr H., Mordasini C., Dumas C., Bonavita M., 2013a, ApJL, 772, L15

Rameau J., Chauvin G., Lagrange A.-M., Klahr H., Bonnefoy M., Mordasini C.,

Bonavita M., Desidera S., Dumas C., Girard J. H., 2013b, A&A, 553, A60

Rameau J., Chauvin G., Lagrange A.-M., Meshkat T., Boccaletti A., Quanz S. P., Currie T., Mawet D., Girard J. H., Bonnefoy M., Kenworthy M., 2013c, ApJL, 779, L26

Reggiani M., Meyer M. R., 2013, A&A, 553, A124

Rousset G., Lacombe F., Puget P., Hubin N. N., Gendron E., Fusco T., Arsenault R., Charton J., Feautrier P., Gigan P., Kern P. Y., Lagrange A.-M., Madec P.-Y., Mouillet D., Rabaud D., Rabou P., Stadler E., Zins G., 2003, in Society of Photo-Optical Instrumentation Engineers (SPIE) Conference Series, Vol. 4839, Society of Photo-Optical Instrumentation Engineers (SPIE) Conference Series, Wizinowich P. L., Bonaccini D., eds., pp. 140–149

Santos N. C., Israelian G., Mayor M., 2004, A&A, 415, 1153

Spiegel D. S., Burrows A., 2012, ApJ, 745, 174

van Leeuwen F., 2007, A&A, 474, 653

Vigan A., Patience J., Marois C., Bonavita M., De Rosa R. J., Macintosh B., Song I., Doyon R., Zuckerman B., Lafrenière D., Barman T., 2012, A&A, 544, A9

Wahhaj Z., Liu M. C., Nielsen E. L., Biller B. A., Hayward T. L., Close L. M., Males J. R., Skemer A., Ftaclas C., Chun M., Thatte N., Tecza M., Shkolnik E. L., Kuchner M., Reid I. N., de Gouveia Dal Pino E. M., Alencar S. H. P., Gregorio-Hetem J., Boss A., Lin D. N. C., Toomey D. W., 2013, ApJ, 773, 179

OUTLOOK

This thesis has focused on optimizing the detection of faint planets primarily with the apodizing phase plate coronagraph (APP: Kenworthy et al. 2010) on the NaCo instrument (Lenzen et al. 2003; Rousset et al. 2003) at the Very Large Telescope (VLT). I begin this Chapter by discussing the current limitations of direct imaging and how new instruments, coronagraphs, and surveys which will yield significant results in the next five years. Then, I make predictions on the next 5-10 years with the potential for the direct detection of another Earth with future Extremely Large Telescopes (ELTs). Finally, I speculate on the long term outlook of the field of exoplanet research.

7.1 Current limitations and The Next Five Years

Significant advances in telescope optics and instruments have led to the discovery of the first few directly imaged exoplanets (HR8799 bcde (Marois et al. 2008, 2010), Fomalhaut b (Kalas et al. 2008), β Pic b (Lagrange et al. 2009, 2010), 2MASS1207 b (Chauvin et al. 2004), 1RXS J1609–2105 b (Lafrenière et al. 2008), HD 95086 b (Rameau et al. 2013a), HD 106906 b (Bailey et al. 2014), GJ 504 b (Kuzuhara et al. 2013), and GU Psc b (Naud et al. 2014).) However, unlike the other exoplanet detection techniques, direct imaging has not yielded many planet detections. There are a number of reasons why there are so few detections, outlined below:

- **Predicted methane:** Many of the first direct imaging surveys (discussed in the section 1.5) were performed in H (1.6μm) and Ks-band (2.18μm), explicitly to take advantage of the predictions from theoretical evolutionary models (e.g. COND: Baraffe et al. 2003) that cool planets would have strong methane absorption features and little cloud opacity. However, most of the direct imaging planets that have been observed so far are not similar to field brown dwarfs of similar effective temperature. These planets do not show the predicted methane absorption (e.g. HR 8799 bcd and 2M1207 b: Skemer et al. 2014) and in some cases are much redder than predicted (HD 95086 b: Galicher et al. 2014). This suggests that future direct imaging instruments and surveys should be focused on the thermal infrared (L'-band, 3.8 μm) and longer wavelengths, where the current detected planets appear the brightest.

- **Quasi-static speckles:** Nearly all of the current instruments used to detect planets have been designed for a wide range of science cases (NaCo at VLT, NIRC2 at Keck, STIS on HST). The ideal instrument designed for the direct imaging of exoplanets would have as few optical paths as possible, to limit the amount of aberrations in the final images, also known as quasi-static speckles. These speckles are similar in size and can be even brighter than a real companion signal. Many image processing algorithms have been designed to counter this limitation. However, in order to reach the faintest planets it is important to design the instrument from a systems level given the science goal of directly imaging exoplanets, and all choices of the design should reflect that.

- **Small number of planets:** Thus far, direct imaging planet searches are very resource intensive, requiring hundreds of stars to be observed to only discover one planet. As a result, there are few directly detected planets, and the stars which are best suited for finding these planets is not known. The properties of these planets and the frequency of planets is also difficult to assess statistically.

Fortunately, there are many exciting new instruments, coronagraphs, image processing algorithms, and direct imaging surveys being developed and implemented now. Based on the experience of many other direct imaging surveys, I am cautious about the exact number of planets that will be discovered with these new
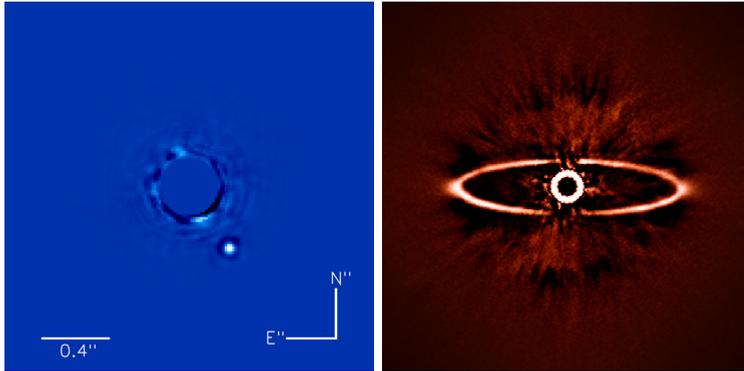
Figure 7.1 Left: GPI detection of the planet beta Pictoris b from the GPI first light press release. Right: SPHERE detection of a dust ring around the star HR 4796A from the SPHERE first light ESO press release.

instruments and surveys. I predict, at a minimum, a dozen new directly imaged planets will be discovered in the next five years, detailed below:

- **Instruments:** Two dedicated exoplanet imagers have recently gone online, making the next few years particularly exciting. The Gemini Planet Imager (GPI: Macintosh et al. 2006) at the Gemini telescope and Spectro-Polarimetric High-contrast Exoplanet REsearch (SPHERE: Beuzit et al. 2008) at the VLT. Figure 7.1 shows the first light data from GPI and SPHERE, which re-detect a planet and disk with much higher signal-to-noise than before and in less time. In addition, the Subaru Coronagraphic Extreme-AO (SCExAO) system (Guyon et al. 2011) at the Subaru telescope is an instrument currently being used for exoplanet direct imaging. The Large Binocular Telescope Interferometer (LBTI: Hinz et al. 2014; Skemer et al. 2014 is very recently in operation. This combines the two 8.4 meter mirrors at the LBT in order obtain the equivalent baseline of 22.8 meter telescope. All of these instruments are remarkably sensitive to lower mass planets (down to 1 Jupiter mass), closer to the star ($> 0''.1$). This increased sensitivity allows us to image – for the first time – planets similar in mass and orbital distance to our own outer Solar System planets. Rather than obtaining broadband images, some of these instruments obtain integral field spectroscopy (IFS) data. Instead of a single image, a data cube is obtained, each frame of which corresponds to a different wavelength. IFS data are extremely powerful, they allow us to detect and characterize planets through spectral analysis (see Konopacky et al. (2013)).

- **Coronagraphs:** There are several new coronagraphic optics which will allow us to probe for fainter planets and closer to the star. Many of the latest coronagraph designs achieve high throughput at small inner working angles. For example, the Vector Vortex coronagraph (Mawet et al. 2005) has

been demonstrated in on sky performance to reach deep sensitivity limits at extremely small angular separations (>0″09). However, these optics are susceptible to tip-tilt vibrations and pointing errors (discussed in 1.4). Pupil plane coronagraphs modify the amplitude (Pueyo et al. 2011) and the phase (Kenworthy et al. 2010) of the wavefronts from the star and planet. One such optic is the vector Apodizing Phase Plate (vAPP: Otten et al. 2014), which has been developed at the Leiden Observatory. The vAPP takes advantage of the design of the standard APP coronagraph (Kenworthy et al. 2010), which modifies the pupil-plane phase in order to create a dark hole on one side of a point source PSF. Most of the work in this thesis takes advantage of the APP coronagraph at NaCo/VLT. The vAPP deals with the most important problem with the APP: one can only search for planets on one side of a star at a time. In order to solve this problem, the vAPP uses a circular polarization to beam-split and create two PSFs with the dark hole on different sides of the star. Thus, the vAPP has all the advantages of the APP (no tip-tilt error, works in the pupil-plane, single optic, see Section 1.4.3) without the dark hole being only on one side. These new coronagraphs will be installed and in operation on several telescopes within the year.

- **Image Processing Algorithms:** Current image processing algorithms typically use the data itself as the reference to create a model stellar PSF to subtract away from each image (ADI: Marois et al. 2006, LOCI: Lafrenière et al. 2007 , PCA: Amara & Quanz 2012, Soummer et al. 2012). However, at small angles, basic ADI results in significant self-subtraction that can hide planets. By observing different stars on the same night with the same observing strategy, we can use the other datasets to create reference PSFs to subtract the stellar PSF in our data (Mawet et al. 2012). This prevents self subtraction in small inner working angles, as an exoplanet is very unlikely to be in the same location in two datasets. By compiling a library of reference PSFs, we can also reanalyze large databases of archival data from telescopes, much of which was never published since no planets were detected.

- **Optimizing chances of finding planets:** The primary targets for directly imaging exoplanets are young, as they are still self-luminous, making them brighter in the infrared. However, determining the age of a star is challenging. Stellar associations are often the targets of direct imaging surveys because the age of the stars are typically well constrained. Thus, one possible way to discover many new planets is to focus on discovering new stellar members of known, young associations. Large direct imaging surveys are resource intensive, requiring many nights of telescope time to observe hundreds of stars, often resulting in only one new planet detection. One other possibility to discover new planets is to focus on the types of stars which have already been found to harbor planets. In our Holey Debris Disks survey (Meshkat et al. 2015), two new planets (HD 106906 b: Bailey et al. 2014, HD 95086 b: Rameau et al. 2013b) were discovered out of our list of only fifteen stars. Given the typically low rate of detection in imaging surveys (<2%), this survey shows that Holey Debris Disks are effective sign-

posts for planet formation. Focusing future direct imaging surveys on Holey Debris Disks targets and discovering new stars with Holey Debris Disks will likely yield a higher planet detection rate.

- **Surveys:** There are several ongoing direct imaging surveys which are expected to be completed in the next few years. The Strategic Explorations of Exoplanets and Disks with Subaru (SEEDS) survey has already published a subset of results (Janson et al. 2013; Brandt et al. 2014), including one planet detection GJ 504 b (Kuzuhara et al. 2013). The complete survey of nearly 400 stars is expected to published soon, which will be the largest number of stars observed in one survey to date. The new second generation imagers GPI and SPHERE both have ongoing very large surveys of stars. Over the next few years, dozens of planets are predicted to be discovered and confirmed with proper motion. The LEECH survey is unique from the previous three surveys in that images will be obtained in L'-band (3.8μm) rather than H-band (1.6μm). This 100 night survey using the LBTI is expected to be completed in the next few years.

One of the most important events that will happen in the next 5 years is the launch of the *James Webb Space Telescope* (JWST). While it almost certainly will not be used for direct imaging surveys (simply due to the vast amount of hours such a survey will require), it will provide the much needed sensitivity necessary to characterize the already discovered direct imaging planets and to perhaps even to see the rocky surfaces of tidally heated exomoons (Peters & Turner 2013). It is important that many planet candidates are detected in the next few years in order to provide the target list for JWST.

7.2   The Long Term

There is a limit to the sensitivity that can be achieved with current ground based telescopes, and as a result, the number of planets that can be detected through direct imaging is limited. At some point in the next 5 years, all the planets which can be directly imaged may well be discovered (from the ground) and subsequently characterized with the JWST. In order to reach fainter planets at smaller inner working angles, we need ELTs sized telescopes. The planned ELTs (the European Extremely Large Telescope, the Giant Magellan Telescope, and the Thirty Meter Telescope) will have the resolving power of a 24 to 40 meter primary mirror at visible and NIR wavelengths. This will give us unprecedented sensitivity at very small angular separations. A study of the planned European Extremely Large Telescope instrument METIS suggests that it will be possible to detect the first nearby super Earth with its increased sensitivity and inner working angle (Quanz et al. 2015). Additionally, by combining high dispersion spectroscopy with high contrast imaging at the European Extremely Large Telescope, it may be possible to detect and characterize nearby rocky planets (Snellen et al. 2015).

It is hard to predict the longer term beyond the ELT generation of telescopes, but it is very likely that Earth-sized planets will be directly imaged in reflected light

within 20 years. It is my sincere hope that as we begin to characterize Earth-twins and perhaps even measure bio-markers, we as a species will collectively reflect on the importance of habitable worlds like our own.

References

Amara, A., & Quanz, S. P. 2012, MNRAS, 427, 948

Bailey, V., Meshkat, T., Reiter, M., et al. 2014, ApJL, 780, L4

Baraffe, I., Chabrier, G., Barman, T. S., Allard, F., & Hauschildt, P. H. 2003, A&A, 402, 701

Beuzit, J.-L., Feldt, M., Dohlen, K., et al. 2008, in Society of Photo-Optical Instrumentation Engineers (SPIE) Conference Series, Vol. 7014, Society of Photo-Optical Instrumentation Engineers (SPIE) Conference Series, 18

Brandt, T. D., McElwain, M. W., Turner, E. L., et al. 2014, ApJ, 794, 159

Chauvin, G., Lagrange, A.-M., Dumas, C., et al. 2004, A&A, 425, L29

Galicher, R., Rameau, J., Bonnefoy, M., et al. 2014, A&A, 565, L4

Guyon, O., Martinache, F., Clergeon, C., et al. 2011, in Society of Photo-Optical Instrumentation Engineers (SPIE) Conference Series, Vol. 8149, Society of Photo-Optical Instrumentation Engineers (SPIE) Conference Series, 8

Hinz, P., Bailey, V. P., Defrère, D., et al. 2014, in Society of Photo-Optical Instrumentation Engineers (SPIE) Conference Series, Vol. 9146, Society of Photo-Optical Instrumentation Engineers (SPIE) Conference Series, 0

Janson, M., Brandt, T. D., Moro-Martín, A., et al. 2013, ApJ, 773, 73

Kalas, P., Graham, J. R., Chiang, E., et al. 2008, Science, 322, 1345

Kenworthy, M. A., Quanz, S. P., Meyer, M. R., et al. 2010, in Society of Photo-Optical Instrumentation Engineers (SPIE) Conference Series, Vol. 7735, Society of Photo-Optical Instrumentation Engineers (SPIE) Conference Series

Konopacky, Q. M., Barman, T. S., Macintosh, B. A., & Marois, C. 2013, Science, 339, 1398

Kuzuhara, M., Tamura, M., Kudo, T., et al. 2013, ApJ, 774, 11

Lafrenière, D., Jayawardhana, R., & van Kerkwijk, M. H. 2008, ApJL, 689, L153

Lafrenière, D., Marois, C., Doyon, R., Nadeau, D., & Artigau, É. 2007, ApJ, 660, 770

Lagrange, A.-M., Gratadour, D., Chauvin, G., et al. 2009, A&A, 493, L21

Lagrange, A.-M., Bonnefoy, M., Chauvin, G., et al. 2010, Science, 329, 57

Macintosh, B., Graham, J., Palmer, D., et al. 2006, in Society of Photo-Optical Instrumentation Engineers (SPIE) Conference Series, Vol. 6272, Society of Photo-Optical Instrumentation Engineers (SPIE) Conference Series, 0

Marois, C., Lafrenière, D., Doyon, R., Macintosh, B., & Nadeau, D. 2006, ApJ, 641, 556

Marois, C., Macintosh, B., Barman, T., et al. 2008, Science, 322, 1348

Marois, C., Macintosh, B., & Véran, J.-P. 2010, in Society of Photo-Optical Instrumentation Engineers (SPIE) Conference Series, Vol. 7736, Society of Photo-Optical Instrumentation Engineers (SPIE) Conference Series

Mawet, D., Riaud, P., Absil, O., & Surdej, J. 2005, ApJ, 633, 1191

Mawet, D., Pueyo, L., Lawson, P., et al. 2012, in Society of Photo-Optical Instrumentation Engineers (SPIE) Conference Series, Vol. 8442, Society of Photo-Optical Instrumentation Engineers (SPIE) Conference Series, 4

Naud, M.-E., Artigau, É., Malo, L., et al. 2014, ApJ, 787, 5

Otten, G. P. P. L., Snik, F., Kenworthy, M. A., Miskiewicz, M. N., & Escuti, M. J. 2014, Optics Express, 22, 30287

Peters, M. A., & Turner, E. L. 2013, ApJ, 769, 98

Pueyo, L., Kasdin, N. J., Carlotti, A., & Vanderbei, R. 2011, ApJS, 195, 25

Quanz, S. P., Crossfield, I., Meyer, M. R., Schmalzl, E., & Held, J. 2015, International Journal of Astrobiology, 14, 279

Rameau, J., Chauvin, G., Lagrange, A.-M., et al. 2013a, A&A, 553, A60

—. 2013b, ApJL, 772, L15

Skemer, A. J., Hinz, P., Esposito, S., et al. 2014, in Society of Photo-Optical Instrumentation Engineers (SPIE) Conference Series, Vol. 9148, Society of Photo-Optical Instrumentation Engineers (SPIE) Conference Series, 0

Snellen, I., de Kok, R., Birkby, J. L., et al. 2015, A&A, 576, A59

Soummer, R., Pueyo, L., & Larkin, J. 2012, ApJL, 755, L28

Nederlandse samenvatting

De interesse in andere planeten maakt al duizenden jaren deel uit van het menselijk onderzoek. De Griekse Filosoof Epicuris stelde, in de vierde eeuw voor Christus, dat er andere werelden – gelijk en anders dan de onze – moeten bestaan. Onze nieuwsgierigheid stamt waarschijnlijk af uit het doel om onszelf, onze planeet en onze plaats in het universum te begrijpen. Tot recentelijk waren de enige planeten die wij kenden afkomstig uit ons eigen zonnestelsel. Ondanks dat het direct verkrijgen van een afbeelding van een planeet de meest logische manier lijkt om planeten in andere zonnestelsels te vinden ("extrasolaire planeet": exoplaneet) hebben technische beperkingen het jarenlang niet toegelaten dat deze methode succesvol was. Het gevolg was dat het bestaan van exoplaneten pas werd bevestigd toen indirecte detectietechnieken gevoelig genoeg werden om planeten te vinden.

De eerste exoplaneetdetectietechniek, genaamd radiële snelheid, meet de kleine wiebel van een ster als gevolg van de zwaartekracht van een nabijgelegen, nog onbekende, planeet. Tot grote verbazing van veel planetaire wetenschappers heeft deze zwaartekrachtwiebeltechniek ervoor gezorgd dat honderden exoplaneten, geheel anders dan die in ons zonnestelsel, aan het licht zijn gekomen. Veel van de eerst ontdekte planeten waren in massa vergelijkbaar met Jupiter, alleen waren ze erg dicht bij hun moederster, binnen de omloopbaan van Mercurius. Vervolgens is er een andere indirecte techniek ontwikkeld om de subtiele daling in helderheid van een ster te detecteren als er een planeet voorlangs passeert (dit wordt een overgang genoemd). Deze overgangstechniek was ook een erg succesvolle indirecte techniek om planeten te detecteren, met als gevolg de ontdekking van honderden exoplaneten. Sindsdien hebben technologische ontwikkelingen vanaf de aarde en telescopen in de ruimte geleid tot de ontdekking van meer dan 1500 bevestigde exoplaneten, verschillend in massa en planetaire architectuur. De grootte en distributie van exoplaneten rond nabijgelegen sterren in ons sterrenstelsel biedt inzicht in de wijze van planeetvorming. Dit kan ons uiteindelijk helpen om erachter te komen of ons zonnestelsel typisch is of een uitzondering.

Het direct verkrijgen van een afbeelding van een exoplaneet is een recentelijk succesvolle techniek die ons toestaat om exoplaneten te detecteren en karakteriseren. Deze techniek is buitengewoon krachtig omdat we licht van de planeet zelf kunnen registreren, dit staat ons toe om de afstand van de planeet tot de ster
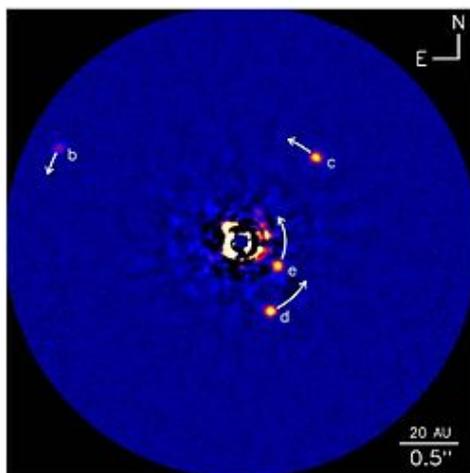
Figuur 7.2 Directe afbeelding van de ster HR 8799 met vier planeten eromheen. De ster is in het centrum van de afbeelding en de vier planeten zijn gelabeld als b, c, d, en e.

en karakteristieken van de planeet zoals atmosfeer te bestuderen. Echter is deze methode van planeetdetectie om meerdere redenen een uitdaging, sommige zijn meteen duidelijk -planeten zijn klein, niet helder en in de buurt van hun heldere moederplaneet- andere zijn niet zo duidelijke -optische limieten. De beperkingen van de huidige technologie staan alleen het direct verkrijgen van een afbeelding toe bij jonge planeten die nog warm zijn van hun vorming. Deze jonge, nog warme, planeten zijn makkelijker te detecteren bij infrarode golflengtes. Aangezien planeetvorming niet goed wordt begrepen zijn direct waargenomen planeten ideale kandidaten om latere fases van planeetvorming te bestuderen.

Ondanks de technische uitdagingen die samengaan met deze vorm van detectie zijn er ongeveer vijftien planeten direct waargenomen, waaronder het meervoudige planetenstelsel HR 8799 (zie Figure 7.2). De detectie van deze jonge planeten begint het gat te dichten tussen planeten op grote afstanden van hun moederster (zoals reuzen and ijsreuzen in ons zonnestelsel) en hun koudere en in een later stadium levende zusterplaneten, die goed in kaart gebracht zijn door de radiële snelheids- en planeetovergangtechniek.

Dit proefschrift

De bevindingen in dit proefschrift zijn gebaseerd op waarnemingen gemaakt met de Very Large Telescope (VLT) in Chili. Ik begin met een onderzoek om het beeldverwerkingsalgoritme -dat gebruikt wordt om niet heldere planeten te detecteren- te optimaliseren. Dit geoptimaliseerde algoritme wordt vervolgens toegepast op verschillende datasets, inclusief twee grootschalige onderzoeken van sterren. Twee van de nieuwe ontdekkingen die uit dit onderzoek komen worden ook in detail

besproken.

In hoofdstuk 2 bespreken we de uitdagingen die samengaan met het detecteren van een zwakke planeet in de buurt van een heel heldere moederster. Door observaties in infrarood wordt het verschil in helderheid tussen de planeet en de ster geminimaliseerd. Ontwikkelingen in telescoopinstrumenten en beeldverwerkingstechnieken hebben het mogelijk gemaakt om deze zwakke bronnen te detecteren. Een van deze ontwikkelingen is principale-componentenanalyse (PCA). Dit algoritme zorgt ervoor dat er zoveel mogelijk licht van de ster uit de afbeelding wordt gehaald zonder het licht van de planeet eruit te halen. We hebben onze eigen PCA code ontwikkeld en toegepast op de directe waarnemingen van het systeem Fomalhaut gemaakt met de VLT. We hebben meerdere tests gedaan en een methode gekozen die het signaal van de zwakke planeet in de buurt van de ster optimaliseert. We tonen aan dat onze PCA code gevoeliger is dan de eerdere analysemethodes.

In hoofdstuk 3 onderzoeken we waarom er zo weinig direct waargenomen planeten ontdekt zijn en wat voor type sterren we moeten observeren om deze planeten te vinden. Dit project, genaamd "Holey Debris Disks" was gevormd om te onderzoeken of de sleuven in de stoffige puinschijf rond de ster indicatoren zijn voor planeetvorming. Het stof ontstaat door botsingen tussen asteroïdes en kometen. De sleuven in de schijf zijn waarschijnlijk gevormd doordat de zwaartekracht van planeten, terwijl deze aan het vormen waren, een sleuf in de schijf hebben uitgesleten. We bespreken de analyse van zes sterren, waarvan de afbeeldingen gemaakt zijn met de VLT en met onze PCA code zijn bewerkt (zoals uitgelegd in hoofdstuk 2). We hebben een model gemaakt van het stof rond de sterren en we hebben de locaties van de gaten in de schijf en de planeten die nodig zijn om die gaten te maken geschat. Ons onderzoek bevat vijftien sterren die we met andere telescopen hebben geobserveerd. Twee planeten, genaamd HD 95086b en HD106906b (zie Figure 7.3), zijn ontdekt tijdens dit onderzoek. Aangezien er relatief weinig direct waargenomen planeten zijn doet de detectie van twee planeten in een kleine hoeveelheid sterren suggereren dat dit type sterren goede kandidaten zijn om andere planeten te vinden.

In hoofdstuk 4 bestuderen we afbeeldingen van de planeet rond HD 95086 gemaakt met de Gemini telescoop in een andere golflengte. In onze aanvullende waarnemingen detecteren we de planeet niet, ondanks dat onze data erg gevoelig is. Deze non-detectie in onze afbeeldingen leidt tot sterke restricties wat betreft de mogelijke massa van de planeet door de helderheid van de planeet te combineren op verschillende golflengtes. Gebaseerd op theoretische modellen kunnen we concluderen dat deze planeet waarschijnlijk rood, stoffig en bewolkt is.

In hoofdstuk 5 bespreken we de ontdekking van een nieuwe compagnon rond een ster, HD 984, met behulp van data van de VLT. We detecteren de compagnon weer in aanvullende afbeeldingen die een paar dagen later zijn genomen; dit versterkt de zaak dat dit een echte bron is. De massa's van direct afgebeelde compagnons worden normaal gesproken afgeleid uit theoretische modellen (zoals in hoofdstuk 4), deze zijn extreem gevoelig voor de leeftijd van de ster. De leeftijd van HD 984 is erg lastig te bepalen; het kan een hele jonge ster van 30 miljoen jaar zijn of een 2 miljard jaar oude ster. Gebaseerd op de extreme verschillen van de leeftijd and de theoretische modellen kan deze compagnon een bruine dwerg met een lage
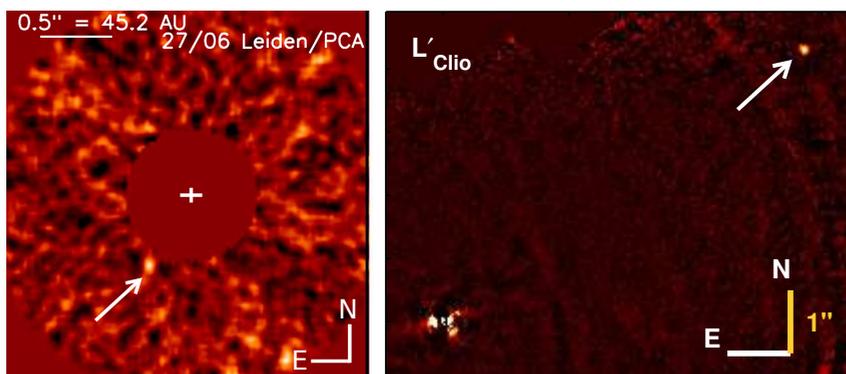
Figuur 7.3 Links: Direct genomen afbeelding van planeet HD 95086b met 5 keer de massa van Jupiter en aangegeven met een witte pijl. Rechts: Direct genomen afbeelding van planeet HD 106906b (witte pijl), die 12 keer de massa van Jupiter heeft en 650 keer verder van zijn ster verwijderd is dan de Aarde van de Zon.

massa zijn -een bruine dwerg is een object met de massa tussen een planeet en een ster- of een ster met een lage massa. Om meer duidelijkheid te krijgen gebruiken we aanvullende data van een ander instrument van de VLT dat ons een spectrum geeft in plaats van een afbeelding. Met dit spectrum kunnen we de atmosfeer van de compagnon vergelijken met de atmosfeer van andere bruine dwergen en sterren met een lage massa. We concluderen dat de compagnon het beste past bij een ster met een lage massa, wat het belang versterkt van het gebruik van een spectrum om de massa van een compagnon te bepalen.

In hoofdstuk 6 bespreken we de resultaten van een onderzoek naar sterren met een hoge massa en gebruiken we de VLT om te zoeken naar planeten. In aanvulling op het zoeken naar nieuwe compagnons proberen we beperkingen te plaatsen op het aantal planeten rond dit type sterren. De frequentie van grote planeten wordt vaak geëxtrapoleerd van radiele snelheidsonderzoeken naar directe waarnemingen hoewel deze twee detectiemethodes misschien verschillende populaties planeten bestrijken. In dit onderzoek hebben we drie stellaire massa compagnons gevonden en één ster met een lage massa (zoals besproken in hoofdstuk 5). We hebben statistische simulaties toegepast om restricties te plaatsen op het bestaan van planeten rond deze sterren. Gebaseerd op de non-detectie van planeten kunnen we bepaalde frequentiemodellen met hoge zekerheid verwerpen.

PUBLICATIONS

1. *Optimized Principal Component Analysis on Coronagraphic Images of the Fomalhaut System*
   T. Meshkat, M. A. Kenworthy, S. P. Quanz, and A. Amara
   2014, ApJ, 780, 17.

2. *Searching for Planets in Holey Debris Disks with the Apodizing Phase Plate*
   T. Meshkat, V. P. Bailey, K. Y. L. Su, M. A. Kenworthy, E. E. Mamajek, P. M. Hinz, and P. S. Smith
   2015, ApJ, 800, 5.

3. *Further Evidence of the Planetary Nature of HD 95086 b from Gemini/NICI H-band Data*
   T. Meshkat, V. Bailey, J. Rameau, M. Bonnefoy, A. Boccaletti, E. E. Mamajek, M. Kenworthy, G. Chauvin, A.-M. Lagrange, K. Y. L. Su, and T. Currie
   2013, ApJL, 775, 40.

4. *Discovery of a Low-Mass Companion to the F7V star HD 984*
   T. Meshkat, M. Bonnefoy, E. E. Mamajek, S. P. Quanz, G. Chauvin, M. A. Kenworthy, J. Rameau, M. R. Meyer, A.-M. Lagrange, J. Lannier, and P. Delorme
   2015, MNRAS, submitted.

5. *Searching for gas giant planets on Solar System scales - A NACO/APP L'-band survey of A- and F-type Main Sequence stars*
   T. Meshkat, M. A. Kenworthy, M. Reggiani, S. P. Quanz, E. E. Mamajek, and M. R. Meyer
   2015, MNRAS, submitted.

6. *HD 106906 b: A Planetary-mass Companion Outside a Massive Debris Disk*

V. Bailey, **T. Meshkat** et al.
2014, ApJL, 780, 4.

7. *Confirmation of the Planet around HD 95086 by Direct Imaging.*
   J. Rameau, G. Chauvin, A.-M. Lagrange, **T. Meshkat** et al.
   2013, ApJL, 779, 26.

8. *Discovery of a Probable 4–5 Jupiter-mass Exoplanet to HD 95086 by Direct-imaging.*
   J. Rameau, G. Chauvin, A.-M. Lagrange, A. Boccaletti, S. P. Quanz, M. Bonnefoy, J. H. Girard, P. Delorme, S. Desidera, H. Klahr, C. Mordasini, C. Dumas, M. Bonavita, **T. Meshkat**, V. Bailey, M. Kenworthy.
   2013, ApJL, 772, 15.

9. *Coronagraphic Observations of Fomalhaut at Solar System Scales.*
   M. A. Kenworthy, **T. Meshkat**, S. P. Quanz, J. H. Girard, M. R. Meyer, M. Kasper.
   2013, ApJ, 764, 7.

Proceedings

1. *Testing Optimized Principal Component on Coronagraphic Images of the Fomalhaut System.*
   T. Meshkat, M. A. Kenworthy, S. P. Quanz, A. Amara.
   2014, IAU Symposium Proceedings, Volume 299, 56-57.

2. *Successes and challenges of the APP Coronagraph.*
   M. A. Kenworthy, S. P. Quanz, G. Otten, **T. Meshkat**, J. Codona, F. Snik, M. E. Meyer, M. Kasper.
   2014, IAU Symposium Proceedings, Volume 299, 40-41.

Curriculum Vitae

I was born on October 7th, 1987 in Mountain View, California, USA. I grew up in San Jose, California, the heart of Silicon Valley, where I attended elementary, middle, and high school. I was particularly inspired to pursue a career in science after watching Carl Sagan's Cosmos tv series, and thus focused on taking many science classes in school. I attended the COSMOS summer school for mathematics and science at the University of California, Santa Cruz. I graduated from Leland High School in 2005.

I attended the University of California, Los Angeles (UCLA), first as a Math major but eventually switched to Astrophysics. I completed two summer programs (Research Experience for Undergraduates: REU) in Math at UCLA and Astrophysics at the National Optical Astronomical Observatory (NOAO) in Tucson, Arizona. During my undergraduate degree, my main research project was with Professor Stanimir Metchev, searching for brown dwarf companions in images from the Lick Observatory. I also worked on a project with Professor Bradley Hansen on modeling a recently discovered exoplanetary system. I graduated with a Bachelors in Science in Astrophysics in 2009, with Highest Departmental Honors, Cum Laude, UCLA College Honors, the Deans Honor List, and the Geoffrey Hilton Award for Excellence in Astronomy.

I then moved to the Netherlands, where I completed my Masters of Science degree in Astronomy at Leiden University in 2011. My Masters minor project was with Dr. Bernhard Brandl studying the far-infrared/radio correlation in the Antennae galaxies. My masters major project was with Professor Ignas Snellen, re-analyzing the methane detection in the atmosphere of the extrasolar planet HD 189733b. I began my PhD work under the supervision of Dr. Matthew Kenworthy in the Fall of 2011. My thesis work has focused on optimizing the algorithms and observations for the direct detection of extrasolar planets. During my PhD, I presented my work at international conferences in the Netherlands, France, Germany, the United Kingdom, Canada, and the United States.

In the Fall of 2015, I will begin my postdoctoral fellowship at the Jet Propulsion Laboratory (JPL) and California Institute of Technology (Caltech) in Pasadena, California. I will continue my research searching for planets in other solar systems by developing new techniques and working with new telescopes and instruments.

Acknowledgements

great friend and you always make sure everyone is laughing. Olga, thank you for always being a source of happiness and fun!

I have made so many great friends at the Leiden Observatory it is almost impossible to name everyone. Alex South, you are a wonderfully kind and close friend, I'm so grateful to have met you. Monica, it's been amazing to go through this PhD process with you, through all the crazy stressful moments, you've been there to support and make me laugh. I've really enjoyed dinner and movie nights with you and Bernard, I wish you all the best on the East coast, you will be missed! Allison, I feel like I've known you for years! Thank you for always being there to get a coffee and laugh about everything with me. And Alex West, you're so much fun and I'm so glad I've gotten to know you! I will miss you both so much! Mason, even when I met you back when we were both Masters students, I knew we would be close friends. I'm glad you chose to stay in Leiden for your PhD so we were able to become better friends. Mattia, you've been a great friend for all these years even before I started my PhD. Thank you for all the support and the great conversations over lunch and coffee. I'm so excited for you and Anna's new adventure in NYC! Matteo, you were one of the first PhDs I met at the Sterrewacht and we've been close ever since. Thank you for mentoring me during my Masters research project. Jayne, thank you for hosting me in Boston and for all your help during my postdoc application process! I couldn't have gotten a position without all your helpful suggestions. Maria, you are an amazing colleague and even better friend. I'm honored to have been your paranymph.

Thank you to my office mates over the years: Maryam, Cristobal, Nico, Stefania, Rafa, Matteo, Javi, David, Ainil, Joana, Tiger, Mehdi. I wish you all the best! Maryam, thank you for sharing your thesis design with me and for celebrating norooz with us. Thank you to all the friends I've made at the Sterrewacht who I've become close with over these years through work and borrels: Alex N, Ali, Andra, Ben, Benne, Berenice, Bram, Carl, Caroline, Christian, David, Gilles, Heather, Henriette, Irene, Jeroen, Jesse, Leah, Lorrie, Marco, Marijke, Mihkel, Nicola, Nienke, Renske, Sascha, Sebastiaan, Shannon, Steven, Thanja. Sebastiaan, thank you for reading over my introduction section. Thanja, thank you for all your help with my thesis printing, you've been my hero! Gilles, it's been great to be your colleague over these years. Many thanks to the borrel organizers over the years, Mher, Nicola, Matteo, Marissa, Marco, Alex S, Heather, Emanuele, Allison, Mason, and David, you have kept us all sane.

Thank you Stan, for hiring me for my first research project in astronomy back at UCLA. It is because of your support and motivation that I felt confident to continue doing research! Thank you to my collaborators in Arizona, Grenoble, Zurich, Berkeley, and Rochester. Working with you has made me a better scientist. Many thanks to those at the Sterrewacht who have helped me throughout the years including the computer group and the secretaries.

Bruce, Lis, Arun and Carine, I am grateful for your kindness and am so happy that I will be joining your family. Thank you Josh for your help with my cover, you're an amazing artist. It's been great getting to know you over these years and I've enjoyed our trips together. I hope you will visit us in California! Hanno, thank you for thought provoking discussions and for being a good friend to me

and Tom over these years. I wish you all the best with your twin babies!

Marissa, you could fall under every category in these acknowledgements from UCLA to Leiden to family. Through all the tough times, both academic and personal, you've been there to support me. It's been great learning astronomy with you from the very beginning. Thank you for everything! Your pursuit of becoming an astronaut is an inspiration. Keep following you dream and don't forget us when you're in space!

My paranymphs are two extremely accomplished PhDs and I am very grateful that they will both travel from long distances to sit by my side on June 11th. Professor Nikki Meshkat and Dr. Marissa Rosenberg, I know you will defend me well.

Finally, my future husband, Tom. You have been my rock for more than 5 amazing years. You are the most positive force in my life, you are my happiness. You keep me sane and calm, even when I'm stressing out. You have gone above and beyond to support me through this process and I am forever grateful. Thank you for being thoughtful, kind and for always making me laugh. Soon our journey will take us to California and I'm so glad you will be by my side.